UNIVERSITY OF CALIFORNIA

IRVINE

Two Photon Decays of Charmonium States Produced in Proton-Antiproton Annihilations

DISSERTATION

submitted in partial satisfaction of the requirements for the degree of

DOCTOR OF PHILOSOPHY

in Physics

by

James Elliot Fast

Dissertation Committee:

Professor Mark A. Mandelkern, Chair

Professor Jonas Schultz

Professor Dennis J. Silverman

1992

The dissertation of James Elliot Fast is approved,
and is acceptable in quality and form
for publication on microfilm:

_____

_____

_____

Committee Chair

University of California, Irvine

1992

Contents

List of Figures

List of Tables

Acknowledgements

The completion of this dissertation is the culmination of a significant collaborative effort of many people. I wish to express my gratitude for the support given by the technical staff of Fermi National Accelerator Laboratory, without whom this experiment would not have been possible.

I would also like to acknowledge the effort of the other graduate students and the postdocs of experiment E760, for they are truly the individuals whose efforts made this a successful experiment. I would like, in particular, to acknowledge the efforts of Augusto Ceccucci and George Zioulas. I would also like to thank Augusto and George, as well as Jose Marques, for their efforts, insights, and valuable feedback.

A special thanks to Rosanna Cester for her extraordinary efforts as spokesperson for E760, as well as for her personal involvement in my work. Thanks to Stephen Pordes, Alan Hahn, and Petros Rapidis for their guidance and direction during my stay at Fermilab.

I would like to thank my advisors, Mark Mandelkern and Jonas Schultz, for their assistance and support, and for the time and effort they have invested in this dissertation.

Finally, I would like to thank my friends and family for their support. A special thanks goes to a smiling squirrel in Minnesota, without whom I would not have been able to accomplish this, or much else, with my sanity intact.

Curriculum Vitae

1987	B.A. in Physics and Mathematics, Colby College, Waterville, ME.
1986–1987	Research Assistant, Department of Physics, Colby College, Waterville, ME.
1987–1988	Teaching Assistant, Department of Physics, University of California, Irvine
1988–1992	Research Assistant, Department of Physics, University of California, Irvine
1990	M.S. in Physics, University of California, Irvine
1992	Ph.D. Physics, University of California, Irvine Dissertation: *Two Photon decays of Charmonium States Produced in Proton-Antiproton Annihilations.* Professor Mark A. Mandelkern, Chair

Publications

L. Bartoszek et al., The E760 Lead-glass Central Calorimeter: Design and Initial Test Results, Nucl. Instr. and Meth. **A301** (1991) 47-60.

T.A. Armstrong et al., Study of the χ_1 and χ_2 Charmonium states Formed in $\bar{p}p$ Annihilations, Nucl. Phys. **B373** (1992) 35.

T.A. Armstrong et al., Precision Measurements of Charmonium States Formed in $\bar{p}p$ Annihilation, Phys. Rev. Lett. **68** (1992) 1468-1471.

E760 Collaboration, Observation of the $^1P_1$ State of Charmonium, FERMILAB-Pub-92/186-E, submitted to Phys. Rev. Lett.

E760 Collaboration, Observation of a 1515 MeV $2\pi^0$ Meson in Proton-Antiproton Annihilation at $\sqrt{s}$ = 2980 and 3097 MeV, submitted to Phys. Rev. Lett.

E760 Collaboration, Measurement of the $\gamma\gamma$ Partial Width of the χ_2 Charmonium Resonance, FERMILAB-Pub-92/266-E, submitted to Phys. Rev. Lett.

E760 Collaboration, Measurement of the J/ψ and ψ' Resonance Parameters in $\bar{p}p$ Annihilation, submitted to Phys. Rev. D.

E760 Collaboration, Measurement of Proton Electromagnetic Form Factors for Time-like High Momentum Transfer, submitted to Phys. Rev. Lett.

E760 Collaboration, Two Photon Decays of the $^1S_0$ Charmonium Resonances Formed in $\bar{p}p$ Annihilations, Phys. Rev. D, to be submitted.

E760 Collaboration, Measurement of the Angular Distributions from the Radiative Decay of the χ_2 State of Charmonium Formed in $\bar{p}p$ Annihilations, Phys. Rev. D, to be submitted.

Abstract

Two Photon Decays of Charmonium States Produced in Proton-Antiproton Annihilations

by

James Elliot Fast

Doctor of Philosophy in Physics

University of California, Irvine, 1992

Professor Mark A. Mandelkern, Chair

The two photon decays of the η_c and χ_2 charmonium states have been measured in $\bar{p}p$ annihilation using the E760 apparatus at Fermilab during the 1990-1991 fixed target run. A search for the η_c' resonance decaying into two photons has also been conducted. The processes $\bar{p}p \rightarrow R \rightarrow \gamma\gamma$ have been measured using a cooled beam of antiprotons circulating in the Fermilab accumulator ring intersecting an internal hydrogen gas-jet target. The final state photons were measured with a high granularity, high resolution lead glass calorimeter.

From a scan of the η_c resonance region, the mass, the total width, and the branching ratio to two photons have been measured. The results are $M_{\eta_c} = 2989.9 \pm 2.2 \pm 0.4\ MeV/c^2$, $\Gamma_{\eta_c} = 15.6 \pm 6.9 \pm 6.4\ MeV$, and $BR(\eta_c \rightarrow \gamma\gamma) = (2.77 \pm 1.19 \pm 0.43) \times 10^{-4}$. Data were taken at the peak of the χ_2 resonance, and the two photon branching ratio was determined to be $BR(\chi_2 \rightarrow \gamma\gamma) = (1.54 \pm 0.40 \pm 0.24) \times 10^{-4}$. Data were collected at several energies around the expected mass of the η_c'. Upper limits have been placed on the product of branching ratios, $BR(\eta_c' \rightarrow \bar{p}p)BR(\eta_c' \rightarrow \gamma\gamma)$, as function of the η_c' mass and total width.

Introduction

This thesis describes measurements of the two photon decays of charmonium in the process $\bar{p}p \rightarrow \bar{c}c \rightarrow \gamma\gamma$ by experiment E760 at the Fermi National Accelerator Laboratory (Fermilab) Antiproton Accumulator. Cross sections, branching ratios, and partial widths are presented for the χ_2 and η_c resonances, as well as upper limits for the process $\bar{p}p \rightarrow \eta_c' \rightarrow \gamma\gamma$ in the vicinity of six points taken during a search for the η_c' resonance. Measurements of the mass and total width of the η_c are also presented. A study of background sources, particularly important for the η_c analysis, is discussed. Finally, a comparison of results with other measurements and with theory is given.

The charm quark was first proposed in 1970 by Glashow, Iliopoulus, and Maiani to explain the absence of strangeness changing weak neutral current processes. In November of 1974 a narrow resonance, the J/ψ, was observed at a mass of 3100 MeV/c^2 in the invariant mass distribution of e^+e^- pairs in the reaction $p + Be \rightarrow e^+e^- + X$ at Brookhaven National Laboratory and simultaneously at the Stanford Linear Accelerator Center in the reaction $e^+e^- \rightarrow hadrons$ at $\sqrt{s} \approx 3100\ MeV$. Shortly thereafter a second resonance, the ψ', was observed at a mass of 3686 MeV/c^2. Studies of the decays of the ψ' revealed intermediate resonances now know as the χ_c states.

Previous experience with the positronium system, a bound electron-positron pair, helped to foster the idea that these states were excitations of a bound quark-antiquark pair ($Q\overline{Q}$) dubbed quarkonium, with the J/ψ family ($c\bar{c}$ bound states) dubbed charmonium. Subsequent experiments have revealed another family of states, the Υ and its excitations, formed from a bottom quark and its antiquark ($b\bar{b}$). The $Q\overline{Q}$ system provides a simple testing ground for the strong force which binds quarks together, playing the role of the "hydrogen atom" of the strong interaction. A non-relativistic treatment of this system using the Schrödinger equation with a static potential, along with relativistic corrections to order $(v/c)^2$, describes the charmonium spectrum and most decay modes adequately. More recently, fully relativistic treatments of the $c\bar{c}$ and $b\bar{b}$ systems have been explored.

In the 18 years since the discovery of the J/ψ, a large body of information about the charmonium spectrum has been compiled. The spectrum in figure 0.1 shows the known and predicted resonances below the $D\overline{D}$ threshold. The majority of the experimental results come from e^+e^- colliders which can only produce charmonium states with the quantum numbers of the photon, $J^{PC} = 1^{--}$. Other states of the $c\bar{c}$ system can only be observed in transitions from the radial excitations of the J/ψ (n^3S_1) in these experiments. Measurements of states with $J^{PC} \neq 1^{--}$ have relied on the resolution of the detectors. For example, the Crystal Ball detector (see figure 0.2), which concentrated on precise photon spectroscopy, had a resolution of about 5 MeV (rms), while many of the charmonium states have small intrinsic line widths, $\Gamma \leq 2\ MeV$. Due to the inherent limitations of these techniques, precision

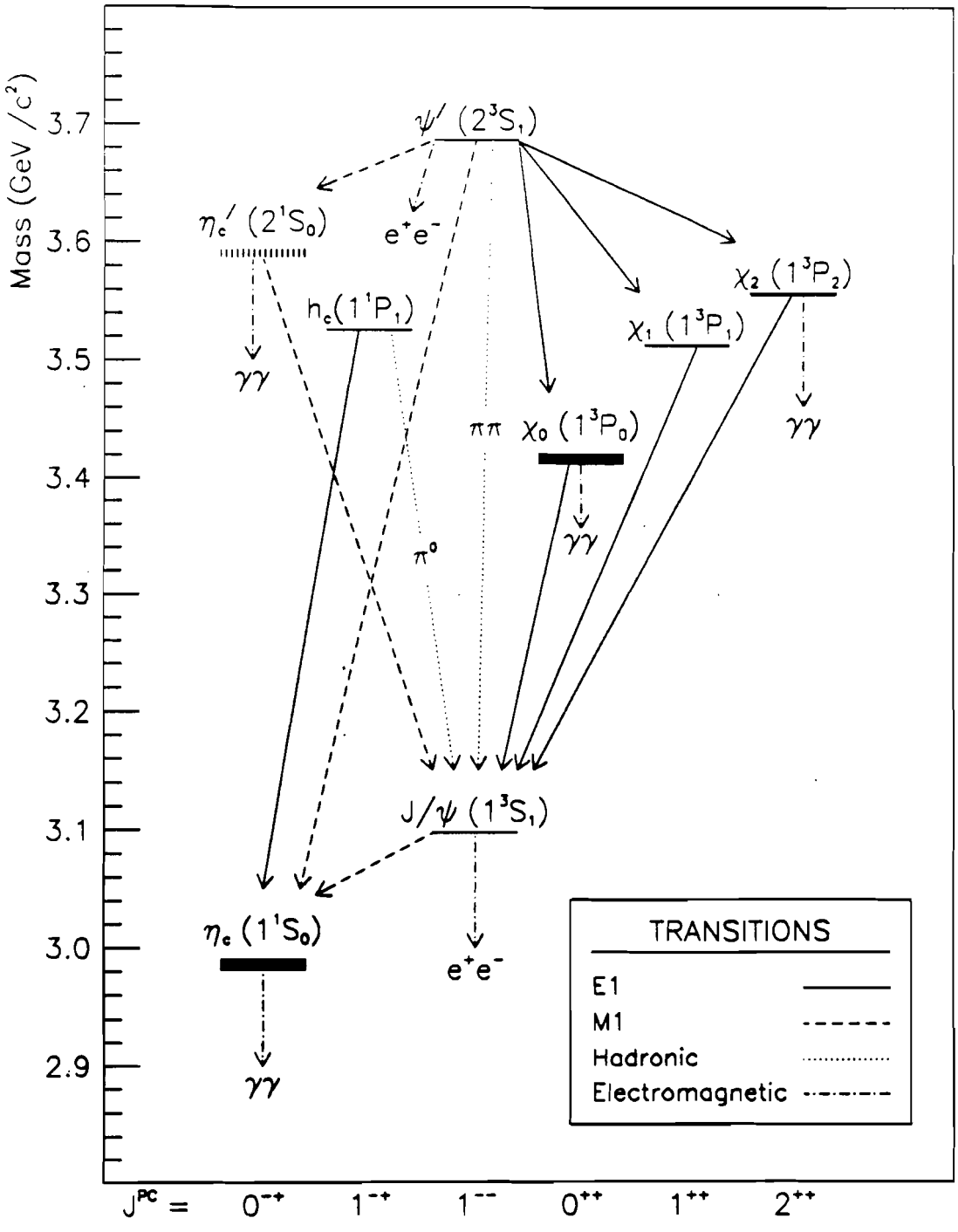

Figure 0.1: Charmonium spectrum

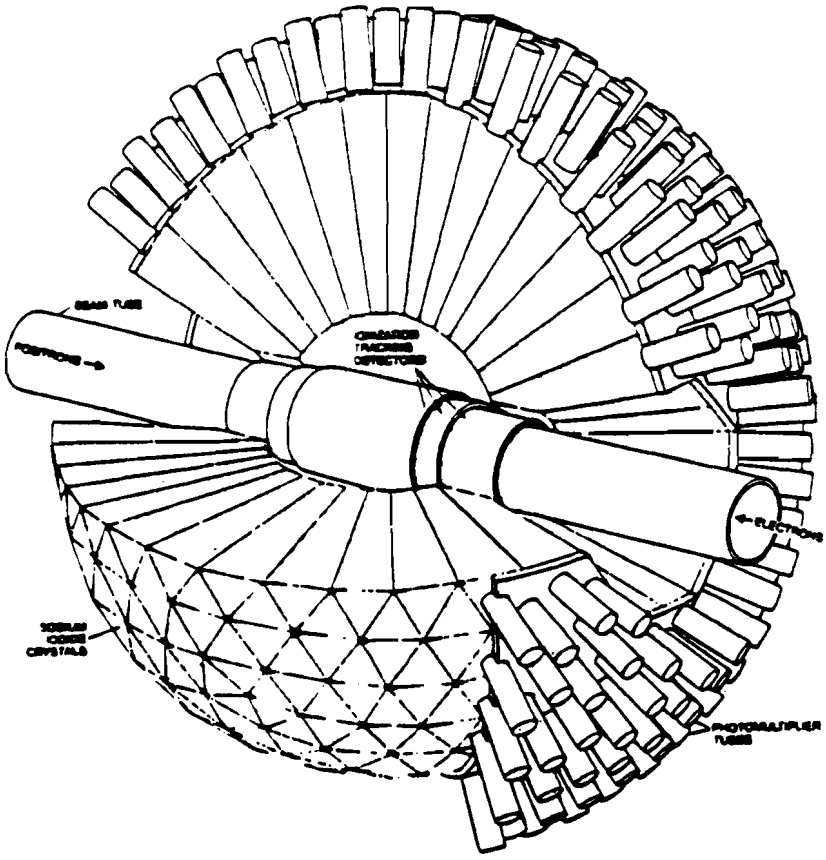

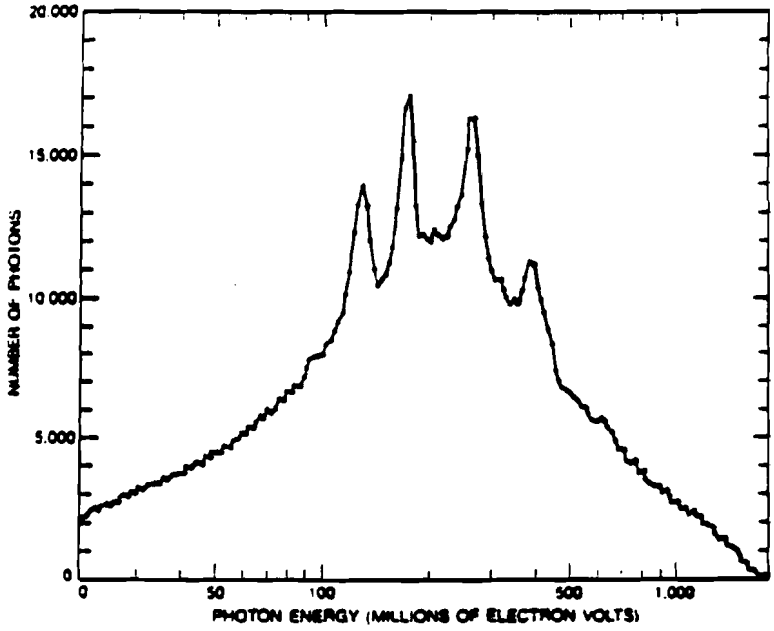

Figure 0.2: Crystal Ball detector and inclusive photon spectrum

measurements of states with $J^{PC} \neq 1^{--}$ have been impossible. A group at CERN, experiment R704, pioneered a method for resonant production of charmonium in $\bar{p}p$ annihilation. This technique allows states of all allowed quantum numbers to be produced directly, but at the expense of large hadronic backgrounds. In this environment one must look for charmonium in electromagnetic final states.

The two photon decays of the η_c ($J^{PC} = 0^{-+}$) and χ_2 ($J^{PC} = 2^{++}$) resonances have been studied by several groups. These measurements have used three different production mechanisms:

1. J/ψ, ψ' radiative decays (DM2, Crystal Ball, DASP)

2. Photon-photon collisions (CLEO, TPC/2γ, ARGUS, PLUTO,VENUS)

3. $\bar{p}p$ annihilation (R704, E760)

The η_c measurements are compatible, but cover a large range of values, $\Gamma(\eta_c \rightarrow \gamma\gamma) = 6 - 28\ KeV$. In addition, the η_c mass and total width are not yet well established [1]. The data for the χ_2 are less consistent, with a measurement of $\Gamma(\chi_2 \rightarrow \gamma\gamma) = 2.9 \pm^{1.3}_{1.0} \pm 1.7\ KeV$ [2] and a result placing a 95% confidence level upper limit of 1 KeV on the partial width [3]. The Crystal Ball collaboration has reported a candidate for the η_c' resonance at a mass of 3594 ± 5 MeV [4], but it has not been confirmed.

Confirmation of the η_c' and precision measurements of the η_c and χ_2 will resolve these discrepancies, and provide valuable constraints on models of the $c\bar{c}$ system. A comparison of the present results with those of previous experiments appears in chapter 8.

Chapter 1

Motivation and Theory

1.1 Motivation

The two photon partial widths of charmonium states provide a direct measure of the running coupling constant, α_s, at the mass of the charmed quark within the framework of Quantum Chromodynamics (QCD), the theory that describes the strong nuclear force in terms of interactions between quarks via gluon exchange. The mass splittings between the singlet and triplet states (η_c - J/ψ or η_c' - ψ') provide information on the spin dependent forces derived from a simple hydrogen-like (single gluon exchange) potential model for the $c\bar{c}$ system.

1.2 Potential Model Approach to Charmonium

Since the discovery of the J/ψ in 1974, much effort has been put forth to understand the $c\bar{c}$ system within the framework of simple potential models [5,6,7]. The greatest difficulty is the determination of the bound state wavefunctions. From these the values of various observables, such as particle masses or mass splittings,

total widths, and partial widths to the simplest final states (2 or 3 gluons, 2 photons, radiative transitions to J/ψ or η_c), can be calculated. Several difficulties arise in doing such calculation in QCD. The form of the potential is unknown, with several models fitting the data equally well. The running coupling constant, or its equivalent in other models, has been parameterized based on experimental results, but is not fundamentally known. Thus, explicit calculations of the wavefunctions and the observables are model-dependent. The perturbative approach employed in Quantum Electrodynamics (QED) calculations runs into problems since the QCD coupling constant is of order unity, so that many higher order terms contribute to these processes. For many processes the lowest order QCD corrections are large, 40% or more. Other methods, such as QCD sum rules, are also used to find relations between observables, for instance to determine mass splittings [8].

The simplest potential model for charmonium consists of a short range single gluon exchange (1/r) term and a long range confinement term. The single gluon exchange term is a purely vector interaction, while the confinement term is typically taken to be a purely scalar interaction, although it can have vector, tensor, or other contributions as well. This form is known as the "Cornell potential":

$$V(r) = -\frac{4}{3}\frac{\alpha_s(Q^2)}{r} + Kr \qquad (1.1$$

where $\alpha_s(Q^2)$ is the QCD coupling constant which varies with the momentum transfer, Q, of the interaction, analogous to α in electromagnetism, and K is a constant determining the strength of the confinement term. The QCD coupling

constant "runs" with Q according to:

$$\alpha_s(Q^2) = \frac{12\pi}{[33-2n_f]\ln(Q^2/\Lambda^2)}\left[1 - \frac{6(153-19n_f)}{(33-2n_f)^2}\frac{\ln[\ln(Q^2/\Lambda^2)]}{\ln(Q^2/\Lambda^2)}\right] + \ldots \quad (1.2)$$

where n_f is the number of quark flavors with mass below Q ($n_f = 3$ for charmonium) and Λ is a parameter of the theory experimentally determined to be $\Lambda \simeq 200\ MeV$ [9]. The fine structure and hyperfine structure are accounted for by the typical spin-orbit, spin-spin and tensor terms:

$$V_{LS}(r) = (\vec{L}\cdot\vec{S})\frac{1}{2m^2 r}\left[3\frac{dV_v}{dr} - \frac{dV_s}{dr}\right] \quad (1.3)$$

$$V_{SS}(r) = \frac{\vec{\sigma_1}\cdot\vec{\sigma_2}}{6m^2}\nabla^2 V_v(r) \quad (1.4)$$

$$V_{tensor}(r) = \frac{3(\vec{\sigma_1}\cdot\hat{r})(\vec{\sigma_2}\cdot\hat{r}) - (\vec{\sigma_1}\cdot\vec{\sigma_2})}{12m^2}\left[\frac{1}{r}\frac{dV_v}{dr} - \frac{d^2V_v}{dr^2}\right] \quad (1.5)$$

where $V_v(r)$ and $V_s(r)$ are the vector and scalar parts of the potential, respectively, $\vec{L}$ is the total angular momentum of the $c\bar{c}$ system, $\vec{s_1} = \vec{\sigma_1}/2$ and $\vec{s_2} = \vec{\sigma_2}/2$ are the quark spins, $\vec{S} = \vec{s_1} + \vec{s_2}$, and m is the charmed quark mass.

In addition, there are significant spin-independent relativistic corrections that must be made to the energy levels ($\simeq 100\ MeV$) [6], as well as possible coupled-channel effects as the mass of the $c\bar{c}$ system approaches the $D\overline{D}$ threshold [6,8]. Measurements of the $J/\psi - \eta_c$, $\psi' - \eta_c'$, and $\chi_{cog} - {}^1P_1$ mass splittings provide valuable information about the strength, range, and Lorentz nature of the hyperfine interactions. The recent measurement of the ${}^1P_1$ mass [10] and improved measurements of the χ_1 and χ_2 masses [11] by E760 result in a very small hyperfine splitting in the P-wave states, with the singlet lying above the spin-weighted center of gravity of the triplet states. Since the expectation values of the spin-orbit and

tensor interactions vanish for both the singlet states and spin-weighted average of the triplet states, the only contribution to the hyperfine splittings is due to the spin-spin term. In addition, the spin-spin term due to the Coulomb part of the potential vanishes in the P-wave states in the non-relativistic limit. Relativistically, the P-wave wavefunction does not vanish at the origin so the Coulomb part of the potential will contribute to the hyperfine splitting. However, this term will shift the singlet state down relative to the center of gravity of the triplet states. Coupled channel effects are thought to be small [12], but these effects are not fully understood for states below the $D\overline{D}$ threshold. The simplest interpretation of the observed splitting is the presence of a Lorentz vector contribution to the confinement term in the potential. Recent work by Gupta, Repko, and Suchyta [13] also support the existence of a vector contribution to the confinement term. Comments on the implications of the present measurement of the η_c mass and the search for the η_c' resonance appear in chapter 8.

Predictions for the rates of various processes have been calculated with first order QCD (single loop) corrections [5,6,7]. These calculations must be used with care as the renormalization scale (the energy at which α_s is evaluated in the expansion) is taken to be the mass of the constituent quark in some cases, and the mass of the resonance in others. The most recent paper by Kwong, Mackenzie, Rosenfeld and Rosner [7] uses the convention of renormalization at the mass of the quark (1.5 GeV). The following formulae are from Table III of Kwong et al.:

$$\Gamma(\eta_c \to gg) = \frac{8\pi\alpha_s^2|\Psi(0)|^2}{3m_c^2}\left[1 + 4.8\frac{\alpha_s}{\pi}\right] \tag{1.6}$$

$$\Gamma(\eta_c \to \gamma\gamma) = \frac{64\pi\alpha^2|\Psi(0)|^2}{27m_c^2}\left[1 - 3.4\frac{\alpha_s}{\pi}\right] \tag{1.7}$$

$$\Gamma(\chi_2 \to gg) = \frac{8\alpha_s^2|R'_{nP}(0)|^2}{5m_c^4}\left[1 - 2.2\frac{\alpha_s}{\pi}\right] \tag{1.8}$$

$$\Gamma(\chi_2 \to \gamma\gamma) = \frac{64\pi\alpha^2|R'_{nP}(0)|^2}{45m_c^4}\left[1 - 16\frac{\alpha_s}{3\pi}\right] \tag{1.9}$$

$$\frac{\Gamma(\eta_c \to \gamma\gamma)}{\Gamma(J/\psi \to \mu^+\mu^-)} = \frac{4}{3}[1 + 1.96\frac{\alpha_s}{\pi}] \tag{1.10}$$

Knowledge of the two photon rates for the η_c and χ_2 can be used to test the validity of these equations, assuming a value of α_s from other sources ($\alpha_s \approx 0.26$), or conversely, these equations can be used to evaluate α_s at the mass of the charmed quark.

More recently, Barnes and Ackleh have calculated the two photon decay rates with relativistic corrections (to all orders) as well as the lowest order QCD corrections described above [14]. Bodwin, Braaten, and Lepage have employed a new technique to avoid infrared divergencies which arise in the P-wave decay amplitudes using factorization theorems valid to all orders in α_s and to order v^2/c^2 [15], however they have only made numerical estimates to lowest order in α_s, not included the leading order QCD radiative corrections to those rates, which are very

significant for charmonium decays. A comparison of the experimental results with these predictions appears in chapter 8.

1.3 Experimental Method

Experiment E760 employs the technique pioneered at the CERN ISR by experiment R704. A beam of antiprotons circulating in the Antiproton Accumulator is decelerated to the resonance energy and cooled. The beam energy distribution is measured very accurately using techniques described in section 2.2.4. The beam energy is stepped through the resonance region in small steps (100 KeV in the center of mass). At each point the detector is used to count the number of charmonium decays. A silicon detector is used to determine the luminosity by counting the number of elastically scattered protons at 86.5°. The resulting excitation curve represents the convolution of the beam energy distribution and the Breit-Wigner line shape of the resonance. With this procedure, it is the beam energy measurement which determines the mass and width of the resonance extracted from the excitation curve. The detector is merely a counting device. However, a good understanding of the detector performance is required for the extraction of branching ratios.

Chapter 2

Experimental Apparatus

2.1 Fermilab Accelerator Facilities

Experiment E760 resides in the Antiproton Accumulator ring at the Fermi National Accelerator Laboratory. The Fermilab complex, shown in figure 2.1, has two distinct modes of operation - fixed target and colliding beams. The facility consists of: a Cockroft-Walton generator that provides 800 KeV protons; a 200 MeV linear accelerator; the 8 GeV Booster synchrotron; the Main Ring, capable of 400 MeV energies; and the superconducting Tevatron ring, capable of accelerating protons to 1 TeV. The facility contains two additional rings, the Debuncher and the Accumulator, used for the production and storage of antiprotons. During collider operations the antiprotons are injected into the Main Ring and subsequently into the Tevatron where they are collided with counter-circulating protons at a center of mass energy of 1.8 TeV. During fixed target operations 800 GeV protons are extracted from the Tevatron to the switchyard area where the beam is split and used either directly or for production of secondary beams for use in several experimental halls.

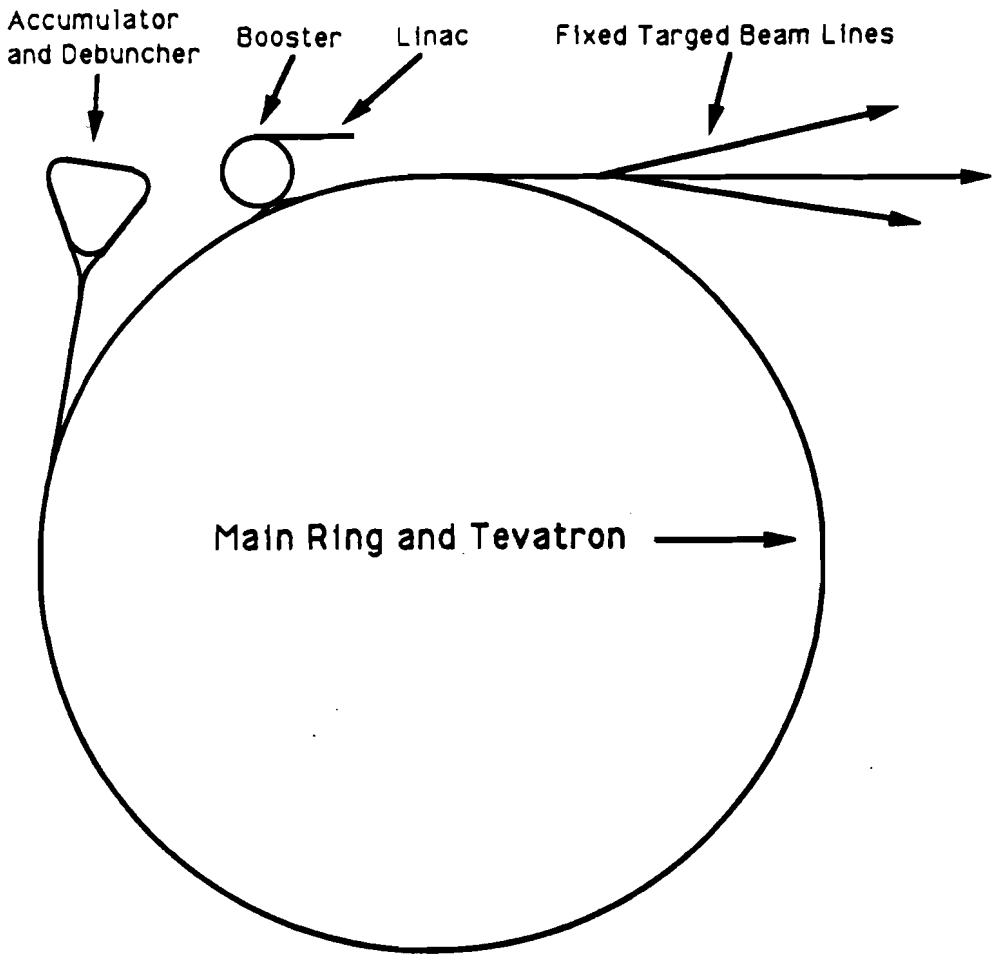

Figure 2.1: Fermi National Accelerator Lab complex

2.2 The $\overline{p}$ Source

2.2.1 General Information and Outline of Operations

Experiment E760 resides in the A-50 sector of the Fermilab antiproton Accumulator, or $\overline{p}$ source, a 475 meter ring designed for storage of antiprotons for the main collider facility. It was designed to operate at a fixed energy of 8.9 GeV with a long beam lifetime (300^{+} hours) in order to store a large number of antiprotons (10^{12}) for injection into the Tevatron.

Several features of the Accumulator make it an ideal location for a $\overline{p}p$ resonant formation experiment. The ring is triangular, containing three low dispersion straight sections ideal for placement of a detector. The Accumulator is idle during fixed target operations at Fermilab, thus an experiment can operate there parasitically during fixed target running. The ring also contains a very efficient stochastic cooling system, so that a beam of small transverse size (≤ 0.5 cm) and small momentum spread ($\delta P/P \leq 2 \times 10^{-4}$) can be obtained. In addition, the cooling is able to compensate for scattering of the beam in the target region.

The antiproton source operation for E760 consists of a period of stacking antiprotons, deceleration to the desired energy, cooling the beam to $\sigma_{E_{CM}} \approx$ 250 KeV, and taking data for 1 to 2 beam lifetimes. The typical stacking rate for the 1991 data taking period was 1 to 2 ma/hr and a typical stack was 30 to 40 ma ($1\ ma = 10^{10}\ \overline{p}$). The beam lifetime was 60 to 100 hrs during data taking. A typical gas-jet density of 10^{14} $atoms/cm^2$ provided the experiment with an ini-

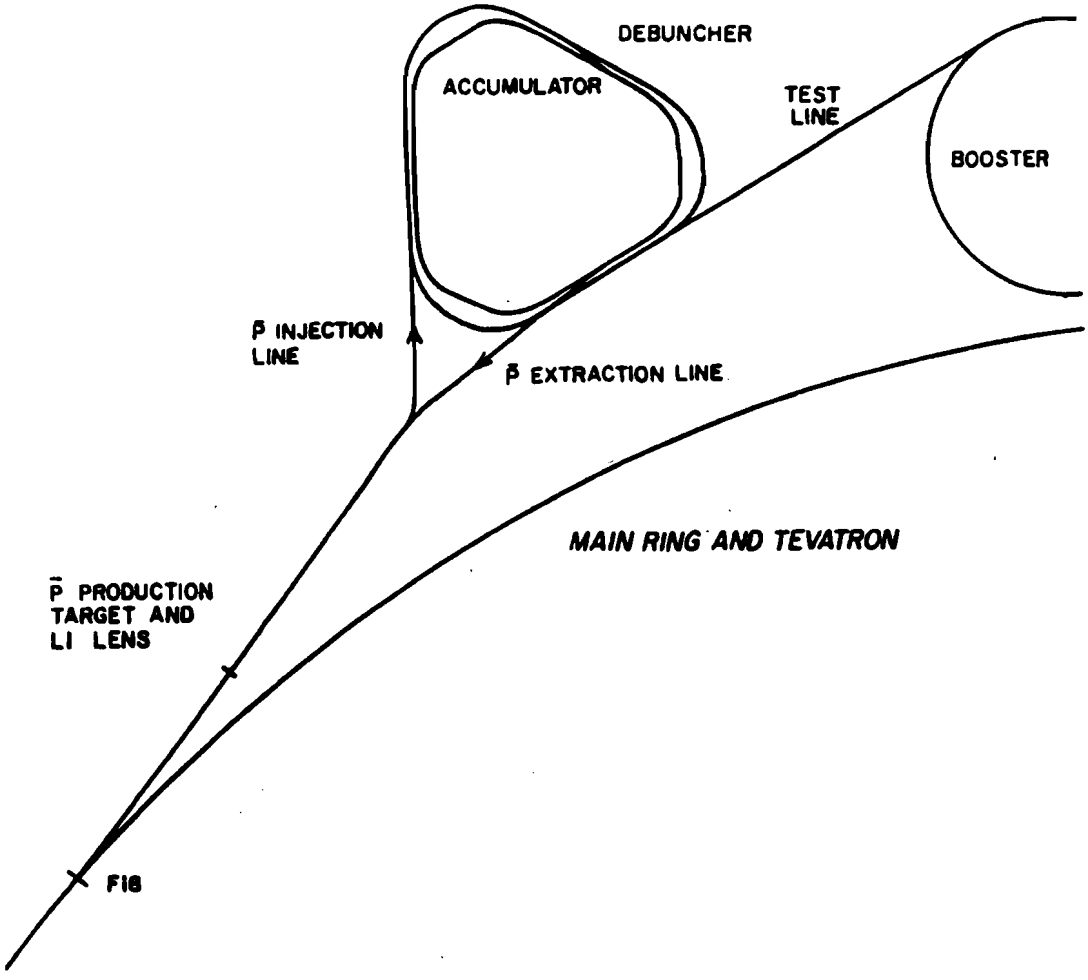

Figure 2.2: Layout of the Fermilab Antiproton Accumulator complex

tial luminosity of $10^{31}\ cm^{-2}s^{-1}$, which corresponds to a total interaction rate of about 700 KHz. One entire data taking cycle, referred to as a "stack", provided an integrated luminosity of $\sim 1pb^{-1}$ in 5 to 7 days.

2.2.2 Stacking ($\overline{p}$ Production)

The antiproton source at Fermilab consists of two separate rings, the Debuncher and the Accumulator. Antiprotons are produced at the AP-0 target hall, transported along the A-2 beam line, injected into the Debuncher ring, and then transferred to the Accumulator where they are stored. During fixed target operations the accelerator complex operates on a 62 second cycle (the Tevatron supercycle). During this cycle the Main Ring provides protons to the Tevatron during the first few seconds. After the Tevatron is filled, the remainder of the supercycle is spent ramping the Tevatron to 900 GeV and doing slow extraction to the fixed target experiments. During the Tevatron ramping and extraction period the Main Ring is available to provide protons for $\overline{p}$ production. Thus stacking of antiprotons can be done symbiotically with normal Fermilab fixed target operations[1].

The target, a 6 cm long piece of tungsten, receives short bunches of 120 GeV protons from the Main Ring. The target is followed by a lithium lens that provides cylindrically symmetric strong focusing to recollimate the divergent beam of secondaries. The lithium lens is 15 cm long with a radius of 1 cm and is pulsed

[1] A detailed description of the Fermilab facilities, including the Antiproton Accumulator, appears in *Design Report Tevatron 1 Project*, Fermilab (1984)

with $\sim$ 500 KA (.6 $msec$ pulse every 2 sec), providing a uniform field gradient of $\sim$ 1000 T/m. The beam is then transported by the A-2 beam line which selects negatively charged particles with a momentum of 8.9 GeV/c. At this point the beam has a large momentum spread but a small time spread, reflecting the bunch structure of the beam incident on the target. The beam circulates in the Debuncher for several seconds, during which it undergoes a longitudinal phase rotation, reducing the momentum spread of the beam while increasing the time spread of the bunches (debunching the beam). The beam is also cooled during this time to further reduce its momentum spread and transverse emittance. The duration of time spent in the Debuncher is sufficient that the majority of the pions and muons in the beam decay. The electrons are lost in the Debuncher where synchrotron radiation causes them to fall out of the machine in a few revolutions. The pure $\bar{p}$ beam is then transferred into the Accumulator ring where it is stored and further cooled.

2.2.3 Stochastic Cooling Systems

The principle behind stochastic cooling systems is quite simple. A pickup measures the deviation of the beam centroid from the central orbit, this signal is transmitted across the ring, amplified, and fed into a kicker which adjusts the

beam accordingly as it passes. The transverse motion of a particle is given by[2]

$$x = A\beta^{1/2}cos(\psi + \delta) \qquad x' = \frac{A}{\beta^{1/2}}\left[\frac{\beta'}{2}cos(\psi + \delta) - sin(\psi + \delta)\right] \tag{2.1}$$

where x and x' are the particle's position and slope (relative to the central orbit), $\beta(s)$ is the betatron function at a point s in the lattice, and ψ is the betatron phase. If it was possible to measure the deviation of each beam particle from the central orbit, Δx, and place the kicker $(n + \frac{1}{2})\pi$, where n is an integer, in betatron phase from the pickup, adjusting the gain to give a kick $\Delta x' = \Delta x/\sqrt{\beta_1\beta_2}$ (where β_1 and β_2 are the values of the betatron function at the pickup and kicker), then all of the beam fluctuations could be removed in one passing of the beam. In practice the pickup must sample many beam particles at once due to bandwidth limitations. The sample size, N_s, determines the number of revolutions (or time) required to cool the beam. The sample size is related to the bandwidth of the cooling system by the expression

$$N_s = \frac{N}{2TW} \tag{2.2}$$

where N is the total number of particles in the ring, T is the revolution period, and W is the bandwidth of the cooling system. The Fermilab Accumulator uses a 4-8 GHz transverse cooling system and has a revolution frequency of about 600 KHz. For a typical stack of 4×10^{11} $\bar{p}$, the sample size is $N_s \approx 3 \times 10^7$. For such a sample there will be a characteristic cooling time

$$\frac{1}{\tau} = \frac{1}{N_s T}\left[2g - g^2 M\right] = \frac{2W}{N}\left[2g - g^2 M\right]. \tag{2.3}$$

[2]A thorough discussion of basic accelerator physics, including stochastic cooling systems, appears in *AIP Conference Proceedings*, **249** (1991).

The parameter g is the gain of the system while

$$M = \frac{1}{2WT|\eta|(\delta p/p)} \tag{2.4}$$

represents the mixing of the beam, i.e. the number of revolutions required for a particle of momentum $p+\delta p$ to move from one sample to another. The parameter $\eta = \frac{1}{\gamma^2} - \frac{1}{\gamma_t^2}$ is known as the momentum slip factor. At the transition "energy" of the accelerator, γ_t, η vanishes. From equation 2.3 we see that when this energy is approached the cooling time becomes small and negative, so the beam is heated by the stochastic cooling system very quickly[3]. Under typical operating conditions at the Fermilab $\overline{p}$ source $M \approx 100$. In order to minimize the cooling time, the gain should be $g = \frac{1}{M} \approx \frac{1}{100}$, and the corresponding cooling time is then

$$\tau = \frac{NM}{2W} = \frac{N}{4W^2T|\eta|(\delta p/p)} \approx 1hour. \tag{2.5}$$

Longitudinal cooling is performed in a similar manner. The deviation of the beam from the central frequency is measured and the beam is given an appropriate longitudinal kick, either by a set of electrodes or using an RF cavity. The longitudinal cooling time is also of order 1 *hour* for the Accumulator.

2.2.4 Beam Energy Measurement

The measurement of the $\overline{p}$ energy is critical to the mass and width measurements performed by E760. During a scan of a resonance the detector is used

[3]This is clearly an unstable operating point for the accelerator. When the transition energy must be crossed, the technique used is to keep the beam at a fixed energy and "jump" γ_t past the beam energy by altering the machine lattice.

to count candidate events and integrated luminosity, while the beam energy is measured to determine the center of mass energy of the interactions. By plotting events/luminosity versus center of mass energy, one obtains a line shape given by the convolution of the beam energy distribution and the resonance Breit-Wigner line shape. Thus, the mass and width are determined from precise knowledge of the beam energy distribution.

The beam energy distribution, in turn, is determined from the beam velocity distribution. The center of mass energy is related to the $\bar{p}$ velocity, β, by

$$E_{CM} = \sqrt{2(1+\gamma)}\, m_p \tag{2.6}$$

where $\gamma = 1/\sqrt{1-\beta^2}$ and m_p is the proton mass. The velocity distribution is obtained by measuring the beam frequency distribution and the orbit length. For a coasting (unbunched) beam, such as that used by E760, the beam frequency spectrum can be obtained by observing the incoherent beam noise, known as Schottky noise, using a beam current monitor and a spectrum analyzer. The Schottky noise bands appear at integer multiples of the beam revolution frequency. The power spectrum for each Schottky band is given by [16]

$$\frac{dI^2}{df_{rev}} = 2e^2 f_{rev}^2 \frac{dN}{df_{rev}} \tag{2.7}$$

so the frequency spectrum, dN/df_{rev}, can be obtained directly from the observed power spectrum. In practice, the pickup is a cavity with a resonant frequency near 79.5 MHz, so that the Schottky band observed is the harmonic nearest to the cavity's resonance frequency, where the gain of the system is highest. A typical Schottky spectrum taken at $\sqrt{s} = 3685\ MeV$ is shown in figure 2.3.

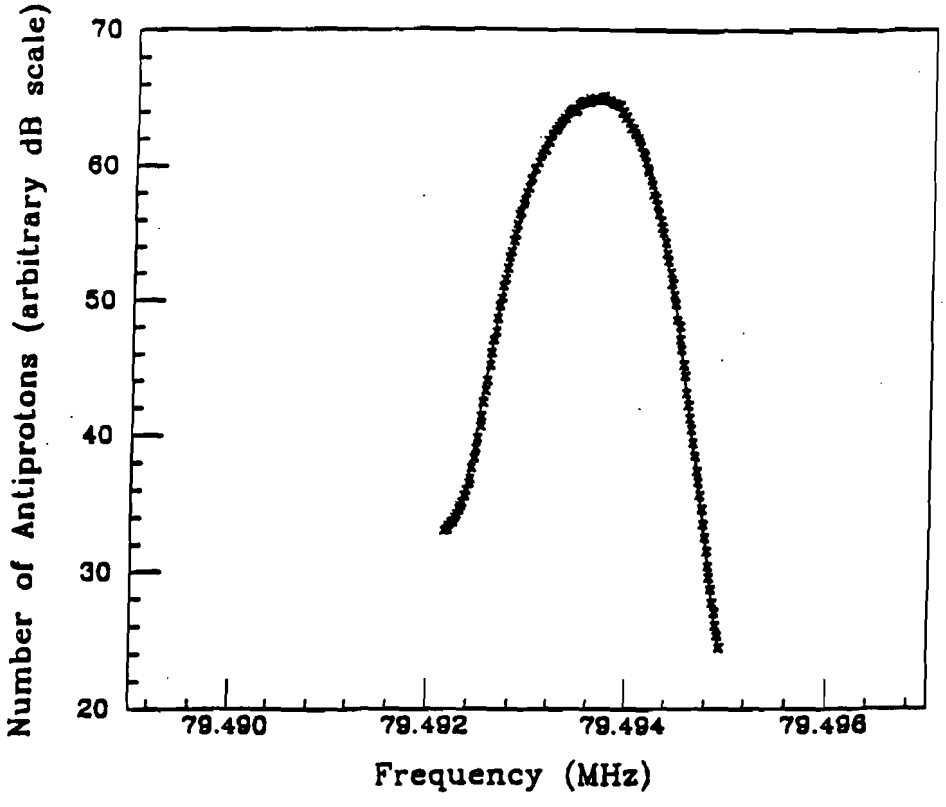

Figure 2.3: Schottky noise spectrum

From equation 2.6, the spread in the center of mass energy is related to the spread in $\overline{p}$ velocities by

$$\frac{\delta E_{CM}}{E_{CM}} = \frac{m_p^2}{E_{CM}} \beta^2 \gamma^3 \frac{\delta \beta}{\beta} \tag{2.8}$$

where the velocity spread is given by

$$\frac{\delta \beta}{\beta} = \sqrt{\left(\frac{\delta L}{L}\right)^2 + \left(\frac{\delta f_{rev}}{f_{rev}}\right)^2}. \tag{2.9}$$

Equations 2.8 and 2.9 can also be used to calculate the error in the beam energy measurement. The frequency measurement is made with an accuracy of 1 part in 10^{-7}, so the error in the center of mass energy from this source, assuming no orbit length error, is only 0.9 KeV to 4.5 KeV over the center of mass energy range 2900 MeV to 3700 MeV. The orbit length is calculated by measuring the difference between a reference orbit and the present orbit using 48 beam position monitors (BPMs). The orbit length difference can be measured to an accuracy of 1 mm, corresponding to the least significant bit of the BPMs. In addition, the reference orbit, taken at the peak of the ψ' resonance, has an error of 0.7 mm in it's length, $\approx$ 475 m, due to the uncertainty in the mass of the ψ'. Therefore the measured orbit lengths are accurate to 1.7 mm, corresponding to center of mass energy errors of 30 KeV to 160 KeV for center of mass energies in the range 2900 MeV to 3700 MeV.

2.3 The Gas-Jet Target

E760 utilizes an internal molecular hydrogen gas-jet target [17]. Gaseous H_2 at high pressure and low temperature is released through a narrow trumpet shaped nozzle. As the gas expands it becomes supersonic. The density of gaseous hydrogen in the nozzle is high enough to cause saturation, followed by nucleation, and formation of clusters of $10^5 - 10^6$ hydrogen molecules (see figure 2.4). The nozzle geometry and subsequent scrapers collimate the jet into a narrow cone which traverses the Accumulator vacuum pipe and then enters a collector where the excess hydrogen is pumped out. The jet size is $\leq 1cm$ in the interaction region and has a density of $\approx 10^{14}\ atoms/cm^2$. A series of vacuum pumps removes residual hydrogen from the delivery and collection stages of the gas-jet in order to minimize diffusion into the Accumulator vacuum system which would degrade the beam lifetime and potentially cause undesirable interactions down stream.

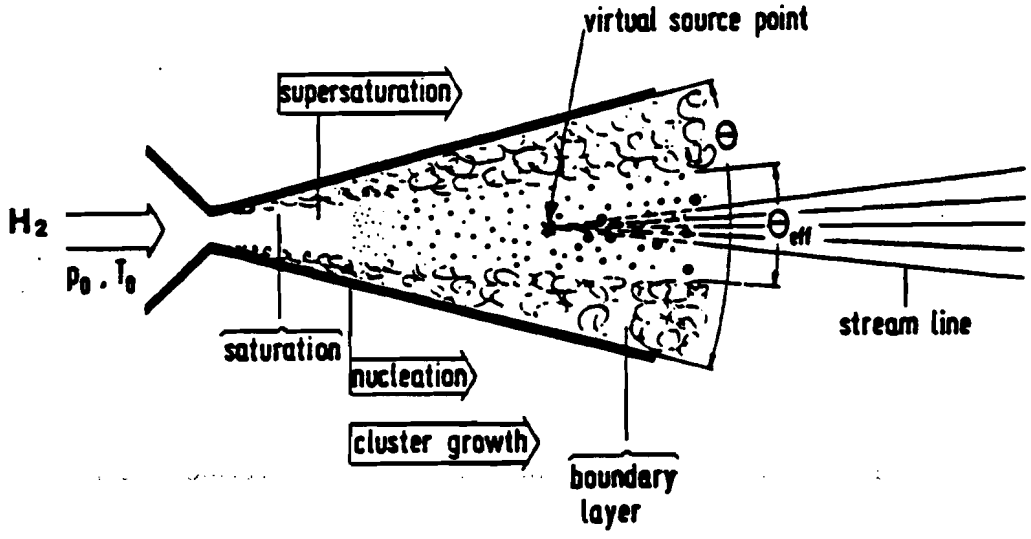

Figure 2.4: Gas-jet schematic

2.4 The Luminosity Monitor

The luminosity is measured by counting recoil protons in a silicon detector at $\theta = 86.435°$. The luminosity monitor is shown in figure 2.5. In addition to the fixed detector used to measure the experiment's luminosity, 6 additional detectors mounted on a moveable carriage were used to study the $\bar{p}p$ forward elastic cross section.

The luminosity is derived using the measured detector acceptance and the known $\bar{p}p$ elastic cross section [18]. The 500 μm thick, 12 $mm \times 48$ mm fixed detector sits 1.47 m below the interaction region in a vacuum chamber connected to the Accumulator beam pipe. The detector is sufficiently thick to stop protons up to 8 MeV/c, while the maximum recoil momentum expected in the detector is 7.1 MeV/c. A typical pulse height spectrum from the detector is shown in figure 2.6. The spectra are fit for an exponential background plus the expected pulse height shape, which is based on the detector acceptance. The statistical error in the number of counts and the error involved in the background subtraction result in a 3% point to point uncertainty in the luminosity. There are three possible sources of systematic errors: the detector area, the value of the $\bar{p}p$ cross section from the literature, and the detector efficiency. The detector dimensions provided by the manufacturer indicate an uncertainty in the area of 2.8%, which has been confirmed with a Monte Carlo simulation. The uncertainty in the $\bar{p}p$ cross section from the literature is 2.5% at these energies. The detector efficiency is assumed to be 100%. These uncertainties result in a systematic error of 5.3% in the luminosity.

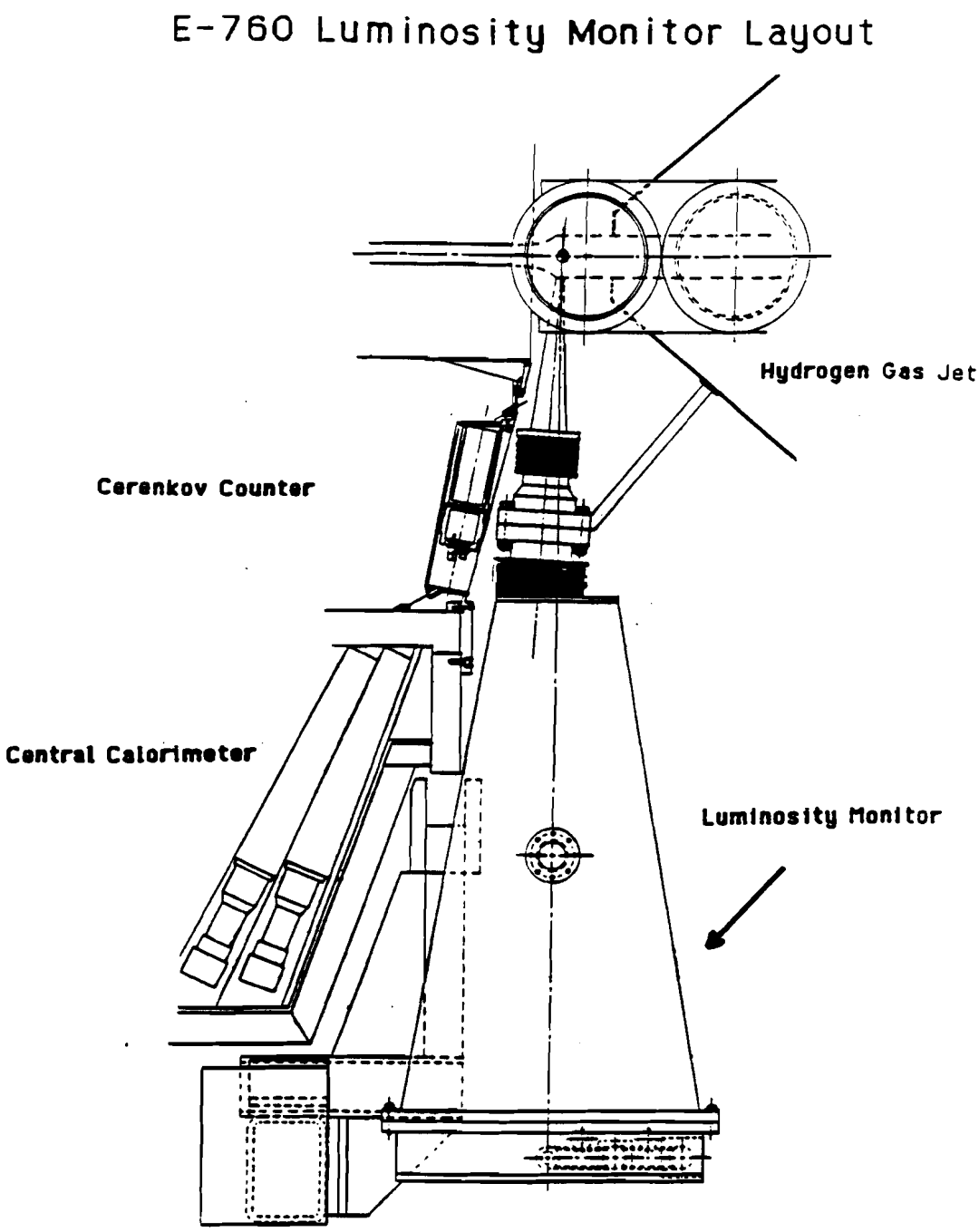

Figure 2.5: Luminosity monitor

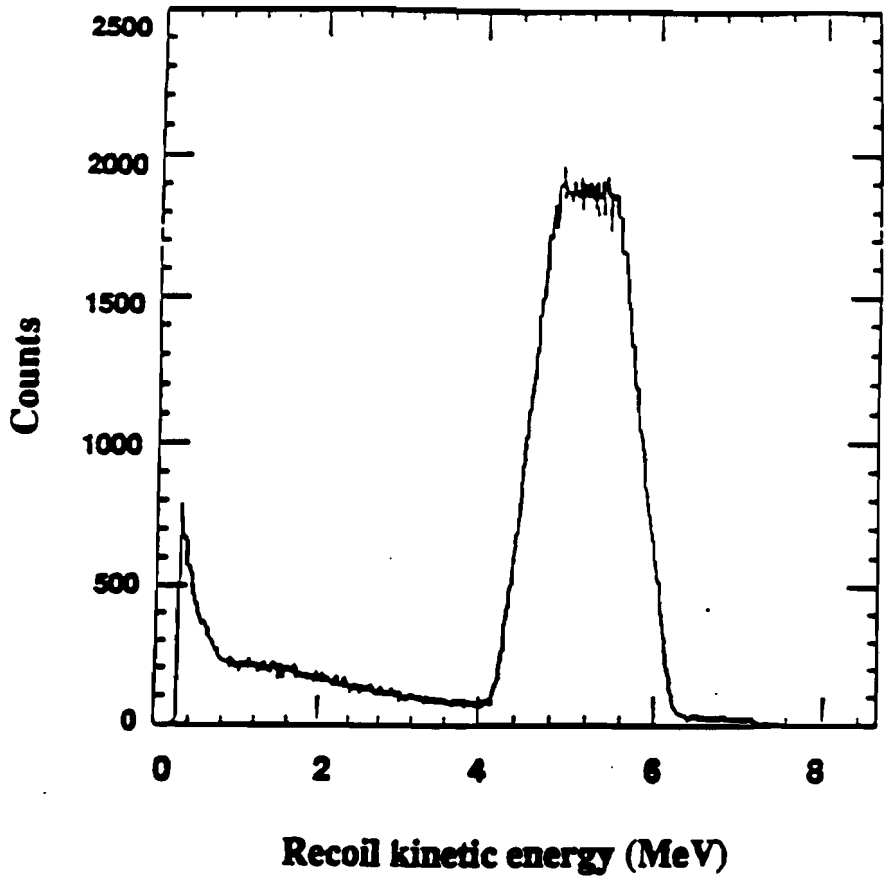

Figure 2.6: Luminosity monitor pulse height spectrum

In addition to the fixed detector used to monitor the experiment luminosity the apparatus is equipped with 6 other detectors mounted on a moveable carriage which serve two functions. They provide a continuous monitor of the fixed detector efficiency, which has remained very stable throughout the data taking period, and they will provide a direct measure of the $\overline{p}p$ cross section parameters, which will make a slight improvement in the systematic error coming from the present values in the literature.

2.5 The E760 Detector

The E760 detector, shown in figure 2.7, is a large acceptance nonmagnetic spectrometer optimized for the identification of the final states $e^+e^- + X$ and $n\gamma$. It has cylindrical symmetry about the beam axis, covering the entire azimuth ϕ and the polar angles $2° \leq \theta \leq 70°$. The central detector covers the region $11° \leq \theta \leq 70°$

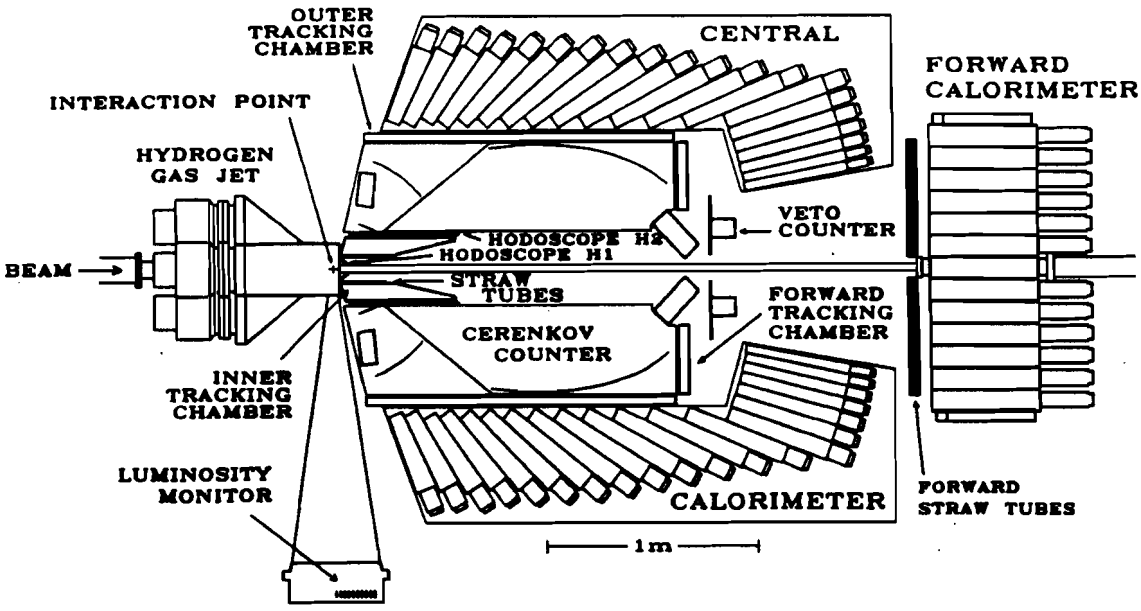

Figure 2.7: The E760 detector

and consist of: an inner trigger hodoscope (H1), two layers of straw tubes [19], a radial projection chamber [20], a multiwire proportional counter [21], a second set of trigger hodoscopes (H2), a multicell threshold Čerenkov counter [22], two layers of limited streamer tubes [23], and the lead glass central calorimeter (CCAL) [24]. In the forward region there are: a set of scintillator counters to veto charged particles in that region (FCV), three planes of straw tubes, and the lead-scintillator forward calorimeter (FCAL) [25]. For all neutral final states, the critical pieces

of the apparatus are the two electromagnetic calorimeters and the scintillator counters used to veto charged particles (H1, FCV).

2.6 The Central Calorimeter

The central calorimeter is cylindrically symmetric around the beam axis with a pointing geometry. The pointing geometry allows for very simple event reconstruction, providing E760 with flexibility in triggering at the hardware level, and allowing for intricate event selection and on-line tagging at the software level. The disadvantage of this choice of geometry is that the manufacturing of the calorimeter components is more costly, particularly the machining of the lead-glass blocks.

2.6.1 Design

The primary consideration in the design of the central calorimeter was the ability to isolate the two photon decays of charmonium from hadronic channels with multi-photon final states. Since these channels have very large cross sections, it was necessary to choose the calorimeter geometry in such a way that the two photon decays could be distinguished from the majority of this background at the trigger level (hardware and software). The pointing geometry used allows for this and greatly simplifies the offline analysis efforts as well.

Of primary concern was the background from $\bar{p}p \rightarrow \pi^0\pi^0$ events. There are two scenarios in which a π^0 can appear as a single photon with the correct kinematics for a 2-body decay. One possibility is that the π^0 decays symmetrically.

In this case the detector may not be able to resolve the photons since they will enter the detector very near each other. The solution to this problem is to place the detector sufficiently far away from the interaction region, and segment it sufficiently, so that the two photons are clearly distinguishable. The obvious problem with this approach is that the detector cost increases dramatically with increasing size, as does the cost of the electronics required for greater segmentation. The other possibility is that the decay is very asymmetric, with the low energy photon lost either below the detector threshold or outside the detector acceptance. This problem also has a straight forward solution, namely the use of extremely sensitive detectors and electronics covering the entire solid angle. But again, the cost becomes prohibitive. An alternative solution is to attain sufficient angular resolution to distinguish between a photon from an asymmetric π^0 decay and one from a $\gamma\gamma$ decay of charmonium. In order to attain this level of angular resolution a pre-shower detector would be needed. This would degrade the energy resolution and would degrade the low energy photon detection efficiency.

In order to assess the relative importance of energy resolution, angular resolution, and detection threshold and in order to find the optimum detector parameters within a finite budget, Monte Carlo simulations were performed using GEANT and EGS. It was found that good energy resolution was crucial, and that achieving a very low detection threshold outweighed the benefits of superior angular resolution.

With the physics goals of good energy resolution and very low photon detection threshold decided upon, several issues remained. Foremost was the choice of material to be used. There were several factors to be considered in this selection: the performance with regard to the physics objectives, the availability of materials, the cost of the raw material and machining, and radiation hardness as the detector was expected to receive about 500 rads during its operational lifetime. While several materials satisfied the performance criteria, lead glass was chosen for its relatively low cost.

Tests were performed on several types of glass from various manufacturers, primarily to assess the response for low energy photons. The blocks needed to be sufficiently long to contain electromagnetic showers from photons and electrons up to 5 GeV, yet be transparent enough to transmit the small amount of Čerenkov light from a low energy photon, most of which is produced very near the front face of the block, to the phototube mounted on the back face. Spectrophotometer measurements and test beam measurements performed at the University of Illinois at Urbana-Champaign (see figure 2.8) resulted in the selection of Schott F2 lead glass. The properties of the glass used in the central calorimeter are summarized in table 2.1. The final segmentation for the detector achieved a balance between the physics requirement of resolving symmetric π^0 decays and cost. The detector contains 1280 lead-glass blocks in a 20 (θ) by 64 (ϕ) array.

The selection of photomultiplier tubes (PMTs) was also driven by the desire to push the low energy detection threshold as low as possible. In addition, the tubes

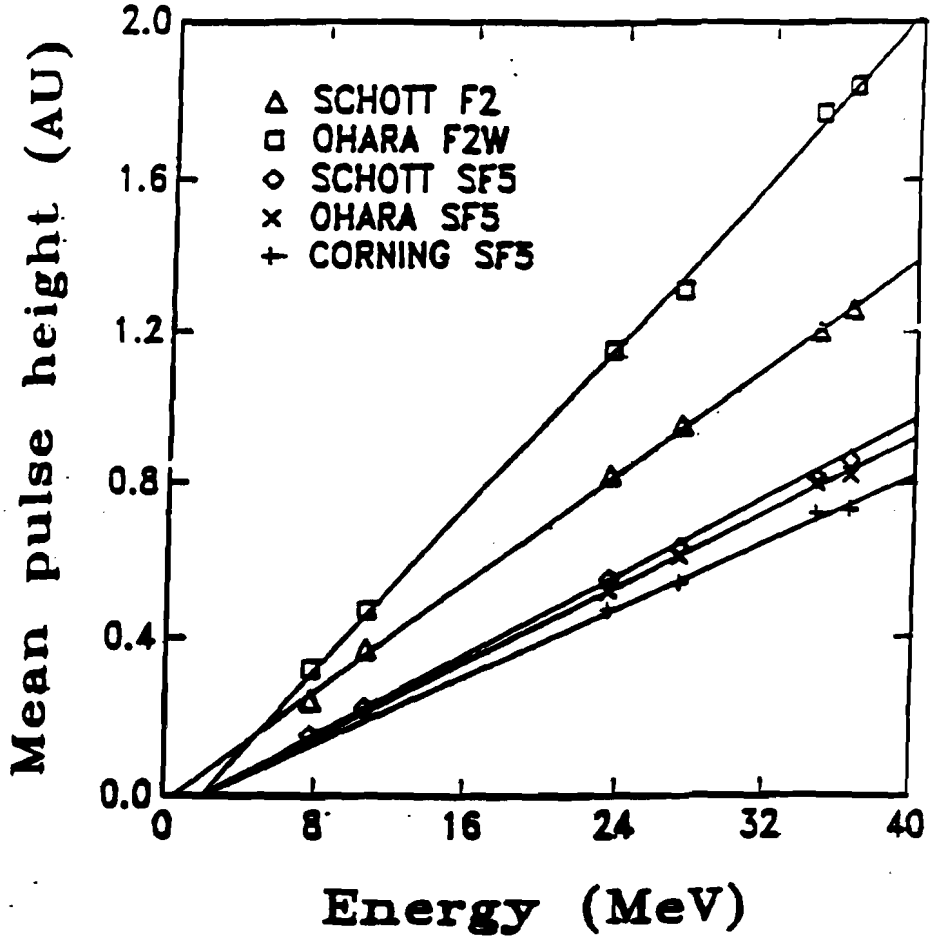

Figure 2.8: Comparison of response of several types of lead glass

Radiation Length	3.141 cm
Density	3.61 g/cm^3
Refractive Index at 404.7 nm	1.651
Composition By Weight:	
Lead	42.2%
Oxygen	29.5%
Silicon	21.4%
Potassium	4.2%
Sodium	2.3%
Arsenic	0.15%
Transmittance Through 10 cm of Glass:	
Wavelength (nm)	Transmittance
335-344	56.9%
385-394	95.5%
435-444	97.9%
485-494	98.4%
535-544	98.9%
585-594	99.4%

Table 2.1: Schott F2 lead-glass specifications

needed to have a linear response over a wide dynamic range, be insensitive to the ambient magnetic fields in the Accumulator tunnel, and be relatively inexpensive. Reasonably fast PMTs were desired to minimize event pile-up in the electronics. The size of the blocks varies substantially due to the geometry of the detector. Four sizes of PMTs from Hamumatsu were selected. The characteristics of the PMTs are summarized in table 2.2.

Photocathode Material		Bialkali	
Window Material		Borosilicate Glass	
Dynode Structure		Linear Focused	
Sensativity Range		300-650 nm	
Peak Sensitivity		420 nm	
Quantum Efficiency (at 450 nm)		0.015	
Model Number	Number of Dynodes	Diameter (in.)	Length (in.)
R3036-02	12	3.0	5.0
R3345-02	12	2.5	5.0
R2154-04	10	2.0	6.0
R580-13	10	1.5	6.0

Table 2.2: Hamamatsu photomultiplier tube characteristics

2.6.2 Construction

In order to facilitate repairs, the detector is assembled in 64 modules known as "wedges". Each self-contained wedge has 20 lead glass modules mounted inside a light-tight stainless steel shell (see figure 2.9). The assembled wedges are mounted on two rings which are free to rotate on the detector stand (raft). Figure 2.10 depicts the calorimeter support structure. The situation shown in the figure would be very unstable as each wedge weighs approximately 500 *lbs.*, but it illustrates the

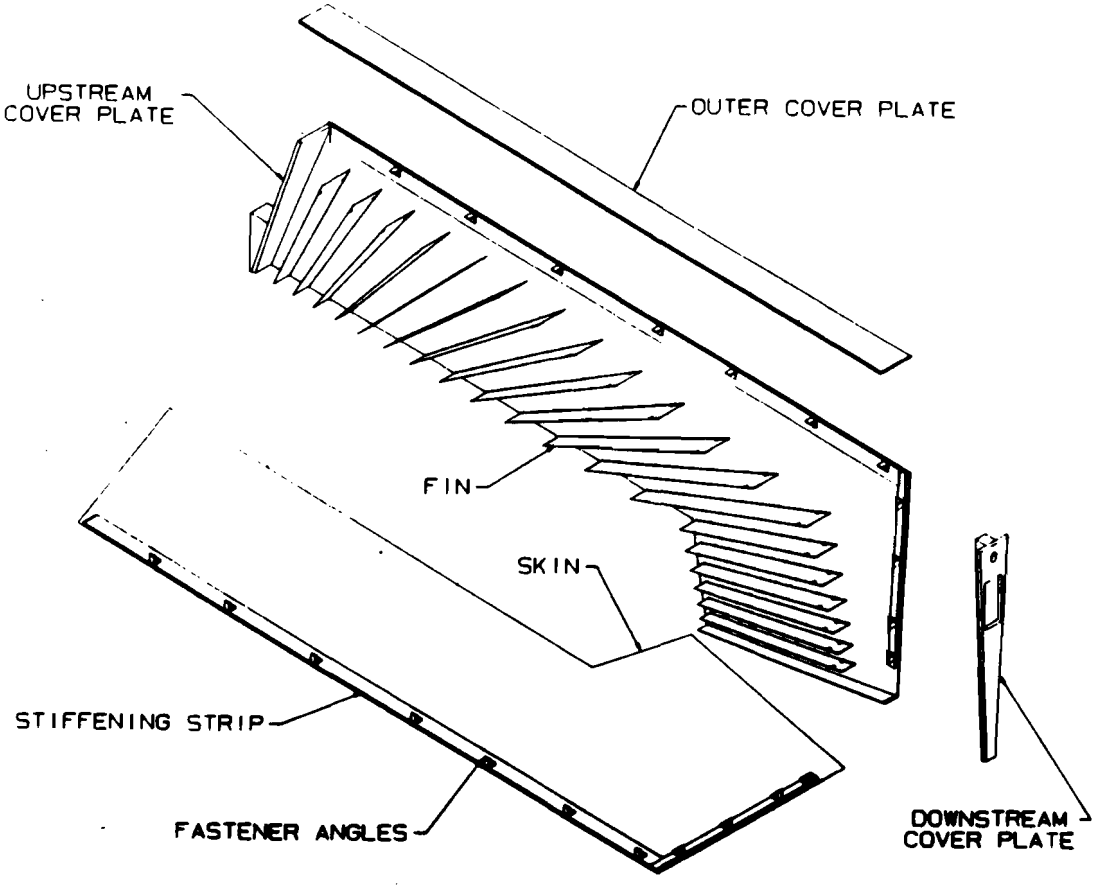

Figure 2.9: Calorimeter wedge assembly

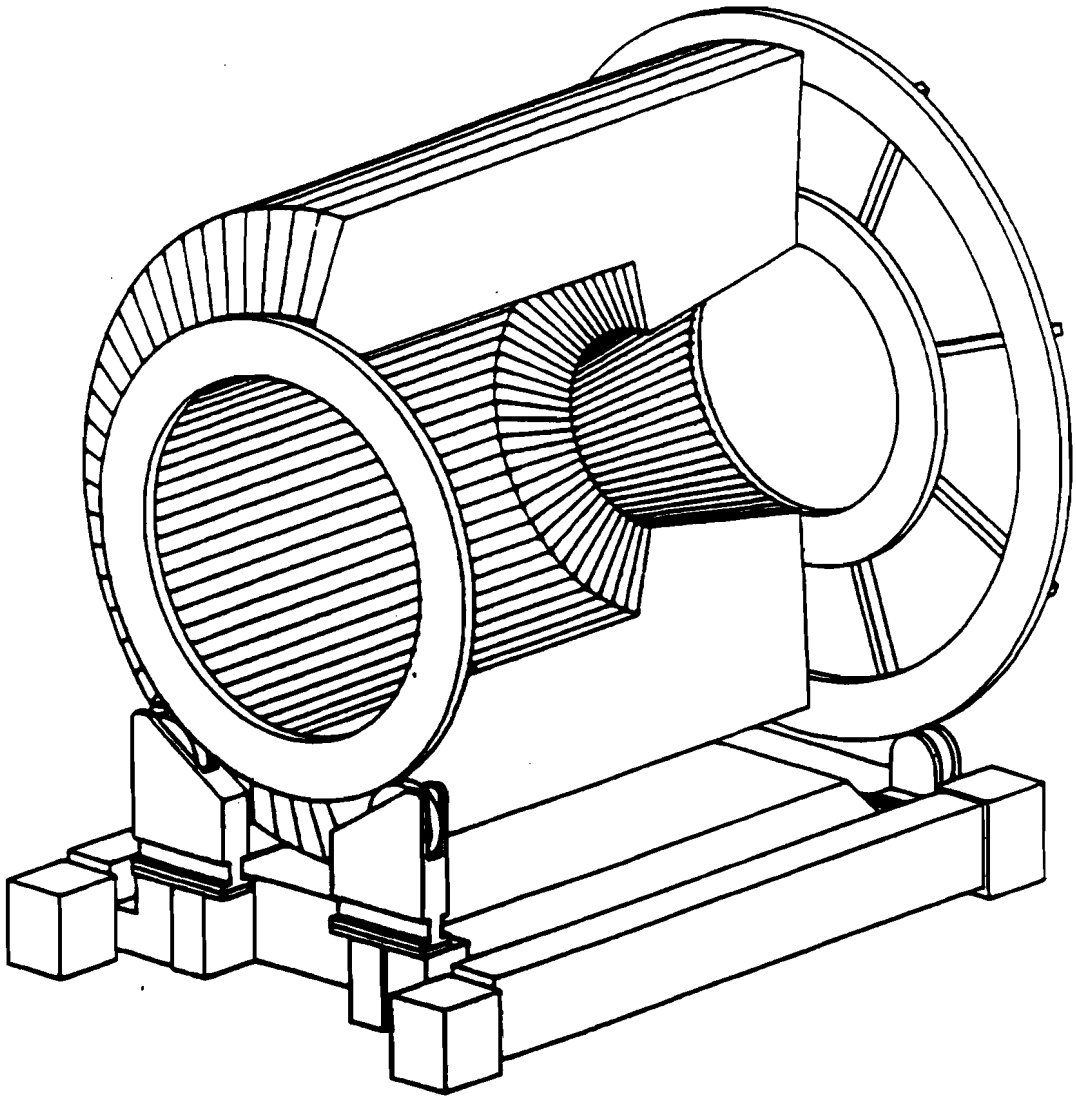

Figure 2.10: Schematic of partially assembled calorimeter

design of the structure. The true assembly procedure begins at the bottom center, with subsequent wedges placed alternately on the left and right sides. During assembly the rings are supported with an exterior frame. Once the majority of the wedges are in place, they provide the support for the rings. The wedges needed to be sufficiently rigid to hold their shape during installation and, for the lower wedges, under the pressure of the wedges above. On the other hand, the hermeticity of the detector is crucial for obtaining the physics objectives of the experiment, so the amount of inactive material between the blocks needed to be minimized. A balance between these objectives was achieved, erring on the side of too much material since the calorimeter would be of little use if the glass was not intact after assembly.

The inner detectors are mounted on a bearing attached to one of the rings so that they may remain stationary while the calorimeter is rotated around them. This design allows a wedge to be rotated to the top and removed for repairs relatively easily. Two spare wedges were assembled as replacements in the event of major problems.

The total weight of the lead glass modules is about 16 tons. The entire assembly including the rings, raft, inner detectors, and gas-jet weighs 25 tons. The area available to maneuver this assembly onto the beam line is minimal, so it was decided to use air casters to "float" the detector, rather than wheels. A set of 5 air casters are mounted to the bottom of the raft and provided with air from an external compressor. When the detector is floating it is easily manipulated by

hand, although prudence is necessary since it is not trivial to stop a 25 ton object once it is moving! Once in place, the detector is supported by a set of 4 vertical jacks which are used to level it at the desired height. Final alignment is aided by use of a set of hydraulic cylinders that extend from the raft to push against the adjacent walls of the Accumulator tunnel. After the detector is surveyed into place the Accumulator beam pipe is connected to the gas-jet and to the beam pipe that runs down the center of the detector. Final cabling completes the installation procedure.

Chapter 3

Trigger and Data Acquisition

The total $\bar{p}p$ cross section in the energy region of interest is about 70 mb, corresponding to an interaction rate of about 700 KHz at the experiment's peak luminosity of $10^{31} cm^{-2} s^{-1}$. The goal of the level 1 and level 2 (hardware) triggers is to reduce this rate to about 1 KHz in order to avoid excessive deadtime in the CAMAC readout and level 3 (software) trigger. The level 3 trigger reduces the rate by another factor of 5 before writing the events to tape.

The charged event rate is easily reduced to a reasonable level using Čerenkov requirements to select electromagnetic final states from charmonium decays, reducing the rate of charged events into the level 3 trigger to about 20 Hz. No such criterion is available for the selection of all neutral final states, which have a cross section of 4.5 mb at $\sqrt{s} = 3\ GeV$, corresponding to a rate of 4.5 KHz. For neutral events, the required factor of 5 reduction from the level 1 and level 2 triggers was achieved using a topological trigger based on the energy deposits in the calorimeters.

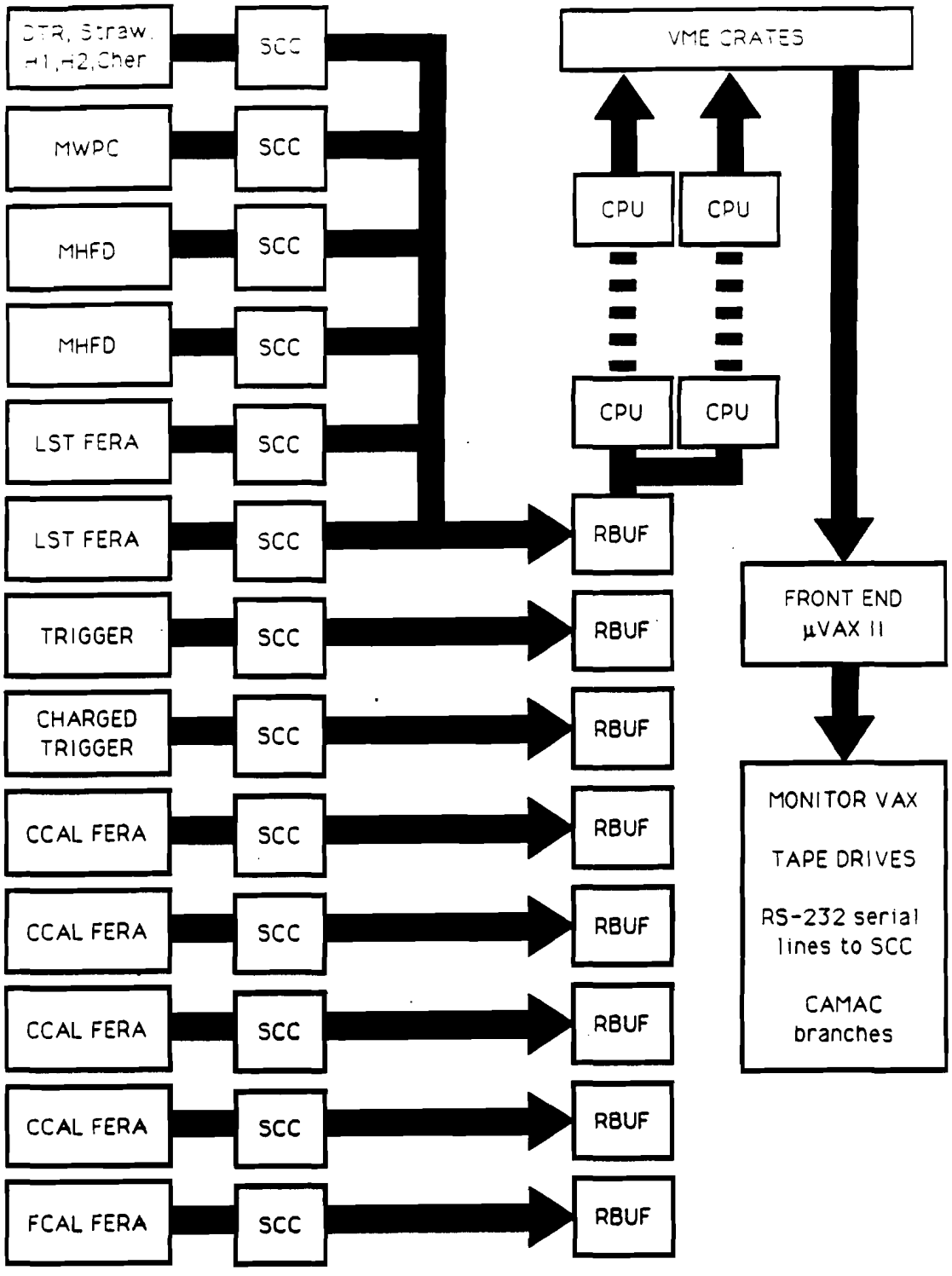

Figure 3.1: E760 data acquisition system

3.1 Level 1 Triggers

The level 1 triggers are a set of simple topological elements formed from pattern unit information from the hodoscopes, Čerenkov counter, and calorimeters.

The central calorimeter plays a crucial role in the trigger. It is equipped with fast analog summers which produce 40 signals, each covering a 5×9 grid ($\theta \times \phi$), referred to as "super-modules". The formation of the super-modules is done in two stages. At the first stage, for each ring (θ), the 64 wedges (ϕ) are linearly summed into 8 groups of 9 blocks each. There is one block of overlap between each of the 8 groups. The 160 output signals from the first stage of summers are used as input to the second stage summers, which now sum over rings (θ) within each octant in ϕ to produce the 40 super-module signals. At the second stage, the 20 rings are summed into 5 groups with 5 rings each, again with a one block overlap between each group. The second stage sums are non-linear since the electrons (or photons) from the decay of a J/ψ (or an η_c) vary in energy as a function of θ due to the Lorentz boost of the beam [26]. This allows discrimination at a uniform center of mass energy regardless of the laboratory angle (θ) of the electron (or photon). These 40 signals are integrated and then discriminated, with the thresholds for each of the super-modules set at 60% to 70% of the energy of an electron (photon) from the decay of a J/ψ (η_c) produced in the reaction $\bar{p}p \rightarrow J/\psi\ (\eta_c) + X$. Finally the discriminator outputs from the 5 super-modules in each octant are logically *ORed* to form the 8 logic signals used to form the level 1 triggers, in particular *PBG*1 which is described below. In addition to these 8 signals, a single total

energy signal is formed using linear summation, without overlap, at the second stage sums. This signal was typically discriminated at 80% to 90% of the total available energy.

The following items constitute the elements of the level 1 trigger:

*PBG*1 This is a topological trigger which requires large energy deposits back-to-back in the central calorimeter. It requires signals from two opposing octants (the source of these is described above, and in detail in [26]). The coplanarity requirement is a 1-to-3 correspondence of opposing octants, i.e. [(octant 1) *AND* (octant 4 *OR* octant 5 *OR* octant 6)] *OR* [(octant 2) *AND* (octant 5 *OR* octant 6 *OR* octant 7)], etc., except at the J/ψ where the correspondence was 1-to-1, i.e. [octant 1 *AND* octant 5] *OR* [octant 2 *AND* octant 6], etc. The octants are numbered in the obvious way, the edge of octant 1 at $\phi = 0$, with the octants numbered sequentially with increasing ϕ.

ETOT This is a total energy trigger which uses the single analog sum from the central calorimeter (described above), discriminated at $\approx 90\%$ of the total available energy.

1*h* A single hadron is defined by signals in an H1 (inner hodoscope) counter and one of the corresponding H2 (outer hodoscope) counters. There are 8 H1 counters and 32 H2 counters. Six H2 counters are mapped to each H1 counter to account for misalignment and the finite size of the interaction region.

$2h$	Two hadrons are defined in the same manner as a single hadron. They may not share the same H1 counter.
$1e$	A single electron is defined by an H1, a corresponding H2 and a corresponding Čerenkov element. The Čerenkov counter is segmented into octants in ϕ, with two cells in each octant. Each octant of the Čerenkov counter (2 cells) is mapped onto one H1 counter.
$2e$	Two electrons are defined in the same way as two hadrons, but with the associated Čerenkov elements for each octant present.
copl	The coplanarity of two charged particles is defined using the H2 hodoscopes. This requirement is a 1-to-1 mapping at the J/ψ and 1-to-3 mapping during all other data taking.
$H1$	These are H1 hodoscope multiplicity requirements. $\overline{H1}$ is a veto on hits in the $H1$ counter array.
$H2$	These are H2 hodoscope multiplicity requirements.
$\overline{FCV}$	This is a veto on the forward scintillator array.
$\overline{FCAL}$	This is a veto on the forward calorimeter. The threshold is set at $\approx 100\ MeV$.

3.2 Level 2 Triggers

The level 2 triggers are formed using the basic elements from the level 1 trigger. They fall into four categories:

MLU1	Charged trigger
MLU2	Two-body trigger
MLU3	Developmental or special trigger
MLU4	Neutral trigger.

The charged trigger (MLU1) is intended to collect, with a high efficiency, final states containing an electron pair, primarily from the decay of a J/ψ in the event. The neutral trigger (MLU4) collects final states containing 2 or more photons with large energy deposits in the calorimeters. Its primary objective is to efficiently collect charmonium events with 2 or 3 photon final states.

3.2.1 The MLU1 Trigger

The MLU1 trigger consists of the logical OR of four different sub-triggers:

1. $(PBG1) \otimes (H2 \leq 4) \otimes (H1 \leq 4) \otimes (2e)$
2. $(PBG1) \otimes (H2 = 2) \otimes (H1 \leq 2) \otimes (2h) \otimes (1e) \otimes (COPL)$
3. $(PBG1) \otimes (H2 = 2) \otimes (H1 \leq 2) \otimes (2h) \otimes (COPL) \otimes (\overline{FCV})$
4. $(H2 = 2) \otimes (H1 \leq 2) \otimes (2e) \otimes (COPL)$.

It is the last sub-trigger which ensures that there is no bias coming from the central calorimeter in the collection of $J/\psi \rightarrow e^+e^-$ and $\psi' \rightarrow e^+e^-$ events used for calculation of the $\gamma\gamma$ analysis efficiency.

3.2.2 The MLU4 Trigger

The MLU4 trigger consists of the logical OR of two different sub-triggers:

1. $(PBG1) \otimes (\overline{H1}) \otimes (\overline{FCV})$

2. $(ETOT) \otimes (\overline{H1}) \otimes (\overline{FCV}) \otimes (\overline{FCAL})$.

The first sub-trigger is intended for the reactions $\bar{p}p \rightarrow \gamma\gamma$ and $\bar{p}p \rightarrow \eta_c + X \rightarrow \gamma\gamma + X$, while the second is intended for multibody processes containing $\pi^0 s$ and ηs.

3.3 Level 3 Triggers

The level 3 trigger system consists of a set of 26 Fermilab ACP modules [27,28]. The primary analysis performed in these modules is the clustering of calorimeter hits, calculation of the invariant masses from all possible pairings of these clusters, and particle identification. The clustering algorithm used in the ACPs is identical to that used in the offline (see chapter 5) except that cluster splitting and sharing are not done. After all invariant mass combinations are calculated, the algorithm searches for masses near known particles beginning with the highest mass objects, the charmonium states. Once a pair of photons have been associated with a particle they are no longer used in searches for lower mass particles. If ambiguities

arise, for instance if several clusters can be associated in different configurations to produce different collections of "particles", then the configuration which produces the largest number of particles is used. A level 3 trigger summary block containing the cluster, invariant mass, and particle information is appended to the data stream.

Software trigger masks are created which utilize the cluster information, identified particles, and total calorimeter energy to select desired topologies. In the case of charged events the level 3 trigger does not cut any events, but the level 3 trigger summary is used to tag specific event topologies for online monitoring, and in order to expedite the making of data summary tapes (DSTs). For neutral data the level 3 trigger is used to reduce the event rate by a factor of 5, to $\approx 200\ Hz$. Although more complex topologies are tagged for DST production, the primary selection masks are very simple:

1. Two cluster invariant mass $\geq 2.0\ GeV/c^2$

2. Total calorimeter energy (CCAL+FCAL) $\geq 80\%$ of the available energy and ≤ 5 clusters.

Additional masks, for example a 3η trigger, are *ORed* with the two primary trigger masks in order to pass interesting events that would not pass the primary trigger masks.

3.4 Trigger Efficiency For $\gamma\gamma$ Events

The trigger for $\gamma\gamma$ events consists of three parts:

1. PBG1

2. Charged particle veto (using H1 and FCV counters)

3. Level 3 (software filter).

The PBG1 efficiency is easily checked using $J/\psi \rightarrow e^+e^-$ data since the two electron trigger discussed above (see MLU1 trigger 4) does not contain this requirement. Using a sample of $\approx$ 3500 clean J/ψ events selected using the Čerenkov counter, the PBG1 requirement is found to be 100% efficient. The level 3 trigger efficiency can also be checked with these events since no charged (MLU1) events are cut by the level 3 trigger. It is also found to be 100% efficient for this type of event.

The charged particle veto requires no hits in either the H1 or FCV scintillator counters. A sample of data was collected with a trigger which required only PBG1 to check the inefficiency due to the charged particle veto. From this data set, a clean sample of $\pi^0\pi^0$ events can be selected with a kinematical fit and mass cuts on the reconstructed pions. It is found that 13.1% of these events have either the H1 or FCV trigger bit set. The probability of Dalitz decay is 1.2% for each π^0 and the probability of conversion in the beam pipe is $\approx$ 1.1% per photon. This results in an intrinsic inefficiency due to the charged particle veto requirement of 6.3%, plus an additional inefficiency of 1.1% per photon in the final state. Thus the

inefficiency for $\gamma\gamma$ final states is 8.5%. The intrinsic inefficiency is consistent with the rate expected from $\delta-$rays coming from the target region (see appendix A).

Each data point used in the $\gamma\gamma$ analysis consists of an entire stack during which the luminosity varies from $\approx 6 \times 10^{30}\ cm^{-2}s^{-1}$ at the beginning of the stack down to $\approx 2 \times 10^{30}\ cm^{-2}s^{-1}$ at the end of the stack. In the determination of the trigger inefficiency, the relevant quantity is the luminosity weighted average inefficiency during the stack. Under the assumption that the inefficiency varies linearly with luminosity, this corresponds to the inefficiency at a luminosity of:

$$L_{equivalent} = \frac{L_0}{2}\left[\frac{1 - e^{-2t/\tau}}{1 - e^{-t/\tau}}\right] \tag{3.1}$$

where L_0 is the initial luminosity at the beginning of the stack, typically $6 \times 10^{30}\ cm^{-2}s^{-1}$, and t is the amount of time during which data is taken, typically 2τ. The data used to calculate the veto inefficiency above were taken at a luminosity of $3.5 \times 10^{30}\ cm^{-2}s^{-1}$, very near the value of $L_{equivalent}$ for a typical stack. A conservative 3% systematic error is included in the final trigger efficiency to account for luminosity dependence.

The overall trigger efficiency for $\gamma\gamma$ events is $91 \pm 3 \pm 3\%$.

Chapter 4

Calibration and Initial Testing of the Calorimeter

4.1 Initial Calibration Using Cosmic Ray Muons

The initial calibration of the central calorimeter modules was done using cosmic ray muons since test beam time was not available for calibration of every module. The goal was to adjust the voltages on the phototubes so that all 1280 modules of the detector would provide the same gain, to within a few percent, upon installation.

4.1.1 Photomultiplier Tube Gain Curve Measurements

The first step in the process was to measure the quantum efficiencies and gains as a function of voltage of the photomultiplier tubes (PMTs). A dark room facility at UCI was equipped with a flashlamp system as a light source and a rack for mounting 30 PMTs at a time. Since the absolute gains of the tubes were important, the relative amount of light falling on each of the rack locations had

to be determined and monitored over the course of the measurements. Three monitor tubes were used for this purpose. One was stationary and held at a fixed voltage to monitor the absolute light output of the flashlamp on a pulse by pulse basis. The other two "roving" monitors were continuously cycled through all of the positions in the rack to monitor the relative amount of light at each position. The phototubes were tested at 2000 V, near the upper limit of their designed operating range, to check for electrical breakdowns. After this "burn-in" cycle, the voltages were lowered to a nominal operating voltage of $\approx$ 1500 V and allowed to stabilize for an hour. The voltages were then adjusted until each PMT produced the desired output for its location in the rack. The voltages were then stepped through a 200 V range centered around the values obtained in the previous step, and measurements of the PMT outputs were made at each voltage. The gain curve for each PMT was then fit with the functional form:

$$Charge = c(Voltage)^m \tag{4.1}$$

4.1.2 Determination of Gains for Cosmic Ray Testing

The physics objectives of the experiment led to the choice of a full scale corresponding to a signal produced by a 5 GeV electron shower. The central calorimeter readout is done using LeCroy FERA ADCs. The full scale for the FERAs is 1900 channels (1920 channels with the pedestal typically at channel 20). The goal of the muon calibration was to set the PMT voltages so that a 3 GeV/c electron traversing the center of each counter would produce the same amount of charge at

the ADCs. Since the calibration was to be done with cosmic ray muons traversing the entire length of the modules, rather than with electrons, the ratio of the signals from these sources was needed. This ratio was determined experimentally. A subset of the detector (3 wedges=60 modules) was taken to Brookhaven National Laboratory (BNL) and placed in a test beam containing both e^- and π^-. A threshold Čerenkov counter was used to tag electrons in the beam. Data were collected at 1, 2, 3 and 4 GeV/c. The 3 GeV/c data were used to calculate the ratio of the responses to pions and electrons, $\frac{\pi}{e^-}$. There are 20 different "shapes" of lead glass blocks used in the detector. The quantity $\frac{\pi}{e^-}$ depends on the block shape since the block length determines the amount of light produced by a minimum ionizing particle, and both the length and the transverse dimensions determine the containment of the electromagnetic showers.

The remaining factor which was needed was the ratio of response to cosmic ray muons and to collimated 3 GeV/c test beam pions. The link which allowed for the transfer of the calibration from BNL to the Fermilab muon lab was a set of ^{207}Bi light pulsers mounted on the front faces of the modules. A typical spectrum from a ^{207}Bi pulser is shown in figure 4.1. The ratio $\frac{\mu}{\pi}$ is independent of the block shape, and its value was found to be $\frac{\mu}{\pi} = 0.85$.

The desired μ mean for a given block shape is given by

$$ADC_\mu = ADC_{e^-} \left(\frac{\mu}{\pi}\right)\left(\frac{\pi}{e^-}\right) = 1140\ (0.85)\left(\frac{\pi}{e^-}\right) \qquad (4.2$$

where 1140 is the desired ADC channel for a 3 GeV/c electron shower. The desired muon means for the 20 block shapes appear in table 4.1.

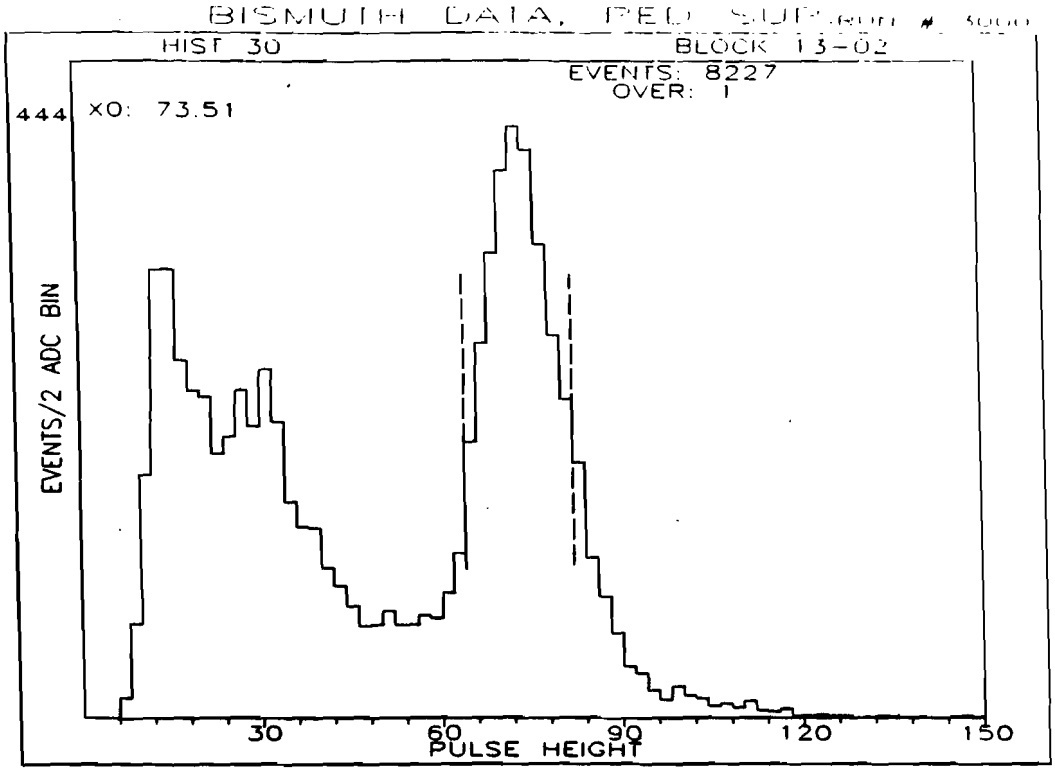

Figure 4.1: Spectrum from ^{207}Bi light pulser

Shape	Desired μ Mean (ADC channels)
1	115.42
2	116.35
3	120.85
4	120.62
5	135.53
6	135.75
7	150.29
8	153.62
9	153.57
10	157.56
11	157.62
12	156.96
13	155.21
14	155.72
15	161.67
16	159.48
17	162.62
18	160.30
19	177.45
20	165.07

Table 4.1: Desired μ means for cosmic ray muon calibration

4.1.3 Determination of Operating Voltages

The experimental setup for the cosmic ray muon measurements consisted of four dark-boxes, each capable of holding 6 lead glass modules in a vertical position, with a set of plastic scintillator hodoscopes positioned above and below each module. Coincidence between any pair of hodoscopes and the associated lead glass module constituted a trigger for all 24 stations. The modules were read-out with FERA ADCs through cables of comparable length to those used in the experimental hall. A schematic of the setup is shown in figure 4.2.

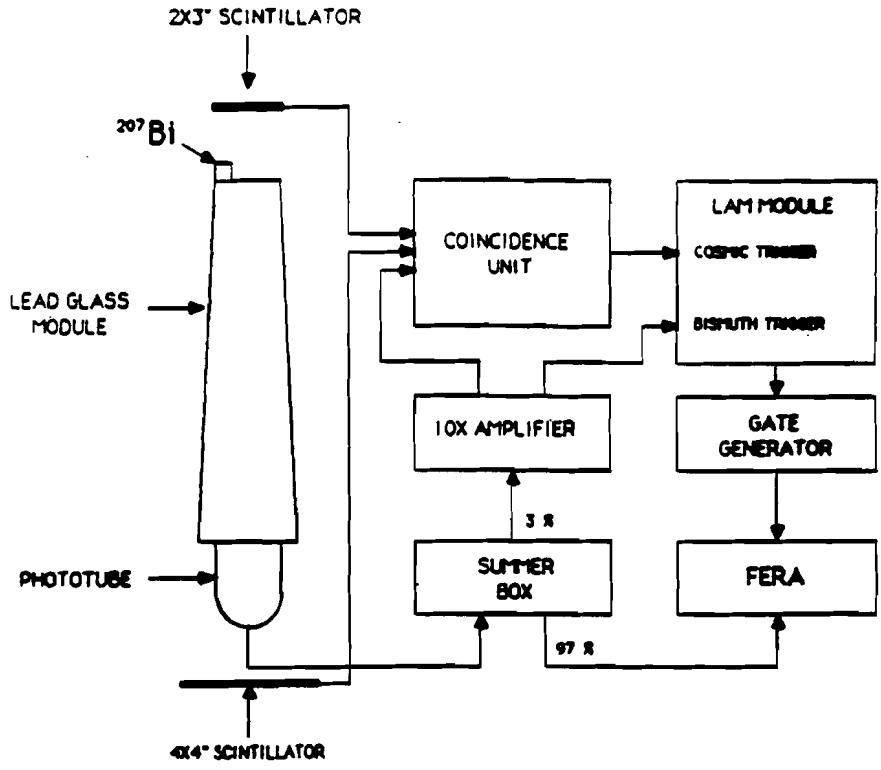

Figure 4.2: Schematic of apparatus used for μ calibration of lead glass

Initial voltages were determined from the gain curves and quantum efficiencies measured at UCI, in conjunction with a Monte Carlo which predicted the average

number of photons that would reach the PMT from a 1 GeV/c electron shower. The counters were tested at these initial voltages, and the means of the cosmic ray muon peaks were determined. Figure 4.3 shows a typical cosmic ray spectrum collected in 18 to 20 hours of data taking. The voltages were then iterated using the relation:

$$Voltage_{final} = Voltage_{initial} \left[\frac{ADC_{desired}}{ADC_{measured}} \right]^{\frac{1}{m}} \tag{4.3}$$

where m is defined in equation 4.1. Only a small subsample of modules were

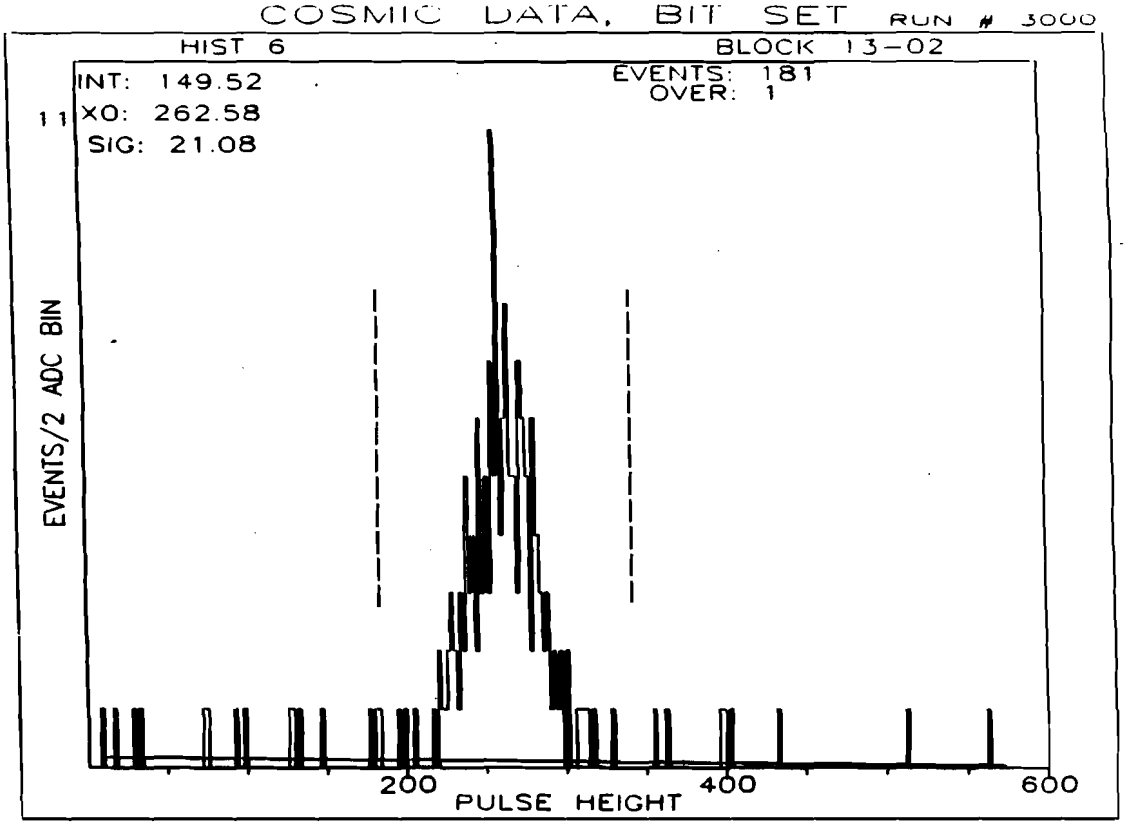

Figure 4.3: Spectrum form cosmic ray muons

retested at the new voltages, in particular those for which the initial measured ADC means were more than 20% off from the desired value ($\leq$ 10% of the modules). There were also 2 monitor modules used, one at a fixed location and one

that was cycled through the remaining 23 locations in the dark-boxes, to monitor the stability of the apparatus and the long term stability of the PMT gains, both of which were found to be quite stable.

The initial *in situ* calibration of the calorimeter with $J/\psi \rightarrow e^+e^-$ events confirmed that the muon calibration was satisfactory, with an rms spread of 6.6% in the gains of the modules and associated electronics.

4.2 *In Situ* Calibration Using $\pi^0\pi^0$ Events

The original plan was to use electrons from J/ψ decay to calibrate the central calorimeter at the outset of the running period, and to track the gains of the modules using a flashlamp system which could supply either blue or green light to each of the modules. This system was installed and operated during the run, but an alternate method was developed which allowed the detector to be recalibrated on a weekly basis using physics events rather than an artificial light source. The method invoked was to use the copious quantity of $\bar{p}p \rightarrow \pi^0\pi^0$ events which were already being written to tape.

The π^0 energies are known from their angles using 2-body kinematics, in the same way that an electron from a J/ψ decay has a well defined energy as a function of its laboratory angle. The $\pi^0\pi^0$ case is slightly more complicated since the angle of each π^0 must be reconstructed from the 4-momenta of the two photons from its decay. One concern is that a poor initial calibration might cause large angular errors, thus causing large errors in the predicted π^0 energies. The predicted

energies are insensitive to moderate calibration errors, varying by $\leq 2\%$ for an angular error of 15 *mrad*.

Up to 18 lead glass modules can contribute to the calculated energy for each π^0 used in the calibration procedure . An iterative χ^2 minimization procedure is used to determine the gain of each block. The function which is minimized at each iteration is

$$\chi^2 = \sum_{j=1}^{N} \frac{(\sum_{i=1}^{n} g_i A_{ij} - E_j)^2}{\sigma_j^2} \tag{4.4}$$

where the sum is over all of the $\pi^0 s$, g_i is the gain for the i^{th} module, A_{ij} is the measured number of ADC counts in the i^{th} module due to the j^{th} π^0, E_j is the predicted energy for the j^{th} π^0 and σ_j is the estimated error in the predicted energy of the j^{th} π^0. Setting the partial derivative of equation 4.4 with respect to g_k equal to zero and solving for g_k gives:

$$g_k = \frac{\sum_{j=1}^{N} \left[A_{kj}/\sigma_j^2\right] \left[E_j - \sum_{i \neq k} A_{ij} g_i\right]}{\sum_{j=1}^{N} \left[A_{kj}^2/\sigma_j^2\right]}. \tag{4.5}$$

The gain constants $g_k^{(n+1)}$ for the $(n+1)^{st}$ iteration are calculated using the gains $g_k^{(n)}$ from the n^{th} iteration in the right hand side of equation 4.5. For the first iteration, the nominal gains from a previous calibration are used. The procedure is iterated until the gains converge.

Chapter 5

Data Analysis

5.1 Introduction

The analysis of $\gamma\gamma$ candidates relies primarily on the performance of the central calorimeter. The design and calibration of the calorimeter have been discussed already. In this chapter the algorithm for determining the positions and energies of showers in the central calorimeter will be discussed in detail, including a discussion on the treatment of overlapping showers. The determination and parameterization of the angular and energy errors is also presented. The chapter concludes with a section discussing the hardware and software used to distinguish between in-time and out-of-time showers in the calorimeter.

5.2 Clustering

5.2.1 Overview of Clustering Algorithm

The central calorimeter clustering algorithm begins by identifying all of the local maxima in the calorimeter, i.e. blocks with more energy deposited in them

than any of their 8 neighbors. A threshold of 5 MeV is used for these central blocks. The total energy deposited in the central block plus its 8 neighbors must be greater than 20 MeV. Once all of these "cluster centers" have been found, an array is formed containing the distances (in block units) between each pair of central blocks. Since the resolution of photons from symmetric π^0 decay is of paramount importance, the algorithm begins by finding the closest pair of clusters. If they are sufficiently close that their electromagnetic showers may have overlapped, then an algorithm designed to share the energies of the blocks in the overlap region is called. The main program removes these two clusters from its list and looks for the next closest pair. Once all such pairs of clusters have been removed, the main routine calls an "isolated" shower routine for any remaining clusters. If any of the showers formed by the isolated shower routine appear to be due to highly symmetric π^0 decays (a cluster *mass* variable is used to identify these cases), then these clusters are passed to a cluster splitting routine similar to the cluster sharing routine.

5.2.2 Isolated Shower Routine

The basic technique used is to calculate the cluster centroid using an energy weighted average of the 9 blocks in a 3 by 3 clusters. The true position of the cluster centroid is then found using a parameterization of the transverse shower profile. The sum of two exponentials is used, with one exponential representing the narrow central core of the shower and the other representing the broad tails

of the shower. The shower profile parameterization is also used to correct for energy lost in the inactive material between the blocks. Due to the different amounts of inactive material between the blocks in θ and ϕ, each direction is parameterized separately. For convenience, the positions are first calculated in "block coordinates", 1-20 in "ring number" (θ) and 0.5-64.5 in "wedge number" (ϕ), then translated into laboratory angles.

Since we are working in "block" units, it is easiest to remove the integer part of the coordinates and calculate the true shower position relative to the middle of the central block of the cluster. Let x represent the fractional part of the ring number, and y represent the fractional part of the wedge number, calculated from the energy weighted average of the 9 blocks in the cluster,

$$x = \frac{\sum_{i=1}^{9} E_i x_i}{\sum_{i=1}^{9} E_i} \qquad y = \frac{\sum_{i=1}^{9} E_i y_i}{\sum_{i=1}^{9} E_i} \tag{5.1}$$

where E_i is the energy deposited in the i^{th} block, $x_i = -1, 0, 1$ is the row number for the i^{th} block, and $y_i = -1, 0, 1$ is the column number of the i^{th} block, relative to the central block. Note that ($x = 0,\ y = 0$) corresponds to the center of the block and that x and y are bounded at ± 0.5. The actual position, (x', y'), is determined from the weighted average position, (x, y), using the relations

$$|x'| = A_x(1 - e^{-\frac{|x|}{x_A}}) + B_x(1 - e^{-\frac{|x|}{x_B}}) \tag{5.2}$$

$$|y'| = A_y(1 - e^{-\frac{|y|}{y_A}}) + B_y(1 - e^{-\frac{|y|}{y_B}}) \tag{5.3}$$

where the actual positions retain the signs of the weighted average positions. The values of the parameters in these expressions, determined empirically from data

taken during the initial calorimeter tests at BNL [24] and from $J/\psi \rightarrow e^+e^-$ data taken *in situ*, appear in table 5.1. Note that the parameters are independent of ring number since the block sizes are nearly equal over the majority of the detector.

Corrections for energy lost in the inactive material between the blocks have been parameterized with a similar functional form

$$E_{corrected} = \frac{E_{measured}}{(1 - C_x e^{-|x''|/x_C})(1 - C_y e^{-|y''|/y_C} - D_y e^{-|y''|/y_D})} \tag{5.4}$$

where $(x'',\ y'')$ is the position of the incident track measured from the edge of the block, as opposed to $(x',\ y')$ which is measured from the center of the block. Due to the staggering of the blocks in θ (see figure 5.1) the ring corrections are

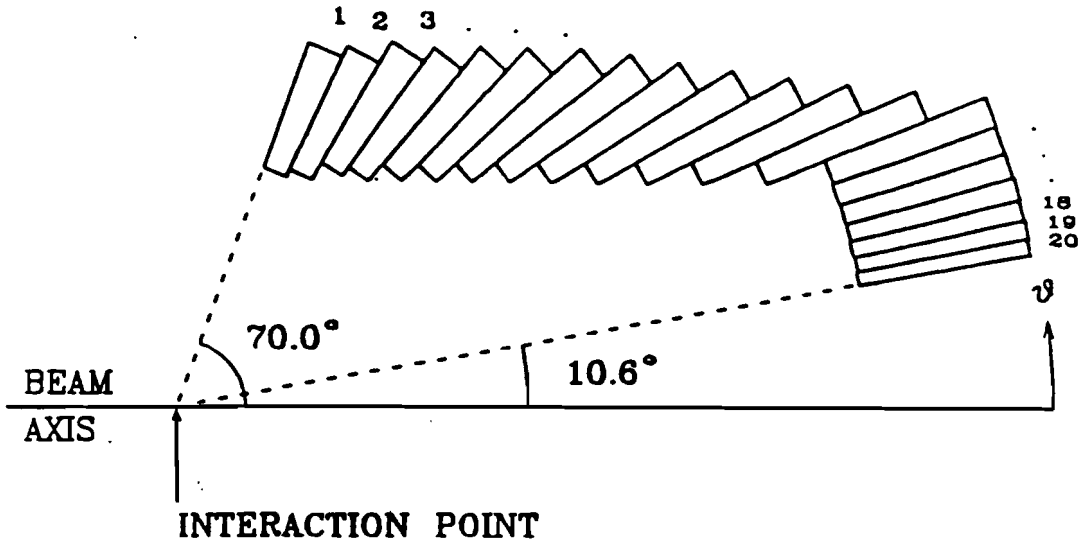

Figure 5.1: Layout of lead glass blocks in one "wedge" of the calorimeter

different depending on which half of the block the incident particle hit, $C_x = C_{low}$ for the "lower" half of the block (lower ring number, larger θ) and $C_x = C_{high}$ for the "higher" half of the block (higher ring number, smaller θ). Table 5.1 contains

the values of these parameters, also found empirically from data taken during the initial calorimeter tests at BNL [24] and from $J/\psi \rightarrow e^+e^-$ data taken *in situ*.

Parameter	Value
A_x (ring)	0.2601
x_A (ring)	0.0321
B_x (ring)	0.2574
x_B (ring)	0.1860
A_y (wedge)	0.3138
y_A (wedge)	0.0397
B_y (wedge)	0.1969
y_B (wedge)	0.1715
C_{low} (ring)	0.0614
$x_{C_{low}}$ (ring)	0.1357
C_{high} (ring)	0.0857
$x_{C_{high}}$ (ring)	0.0508
C_y (wedge)	0.1474
y_C (wedge)	0.0204
D_y (wedge)	0.1594
y_D (wedge)	0.0784

Table 5.1: Values of clustering parameters.

5.2.3 Cluster Sharing Routine

When two energy depositions overlap, the measured energy in some of the blocks is due to contributions from each shower. This energy must be "shared" between the two showers in order to calculate their energies and positions accurately. An iterative procedure is used in which each block, i, in the region defined by the union of the two 3 by 3 clusters is given a weight w_{ij} for cluster j. These weights are normalized such that $w_{i1} + w_{i2} = 1$ for all i. Using these weight, the positions and energies of the two clusters are determined just as for the isolated

shower case:

$$x_1 = \frac{\sum_i w_{i1} E_i x_i}{\sum_i w_{i1} E_i} \tag{5.5}$$

$$x_2 = \frac{\sum_i w_{i2} E_i x_i}{\sum_i w_{i2} E_i} \tag{5.6}$$

and similarly for y_1 and y_2. The weights, which depend on the positions and energies of the two clusters, are re-evaluated at each iteration, and new positions and energies for the clusters are calculated. The shower profile parameters used to obtain the actual laboratory energy and angles are the same as those used in the isolated shower case. This procedure is iterated until the cluster positions and energies stabilize. The criteria used for convergence are: $\Delta\theta \leq 5\ mrad$, $\Delta\phi \leq 5\ mrad$, and $\Delta E \leq 30\ MeV$. In most instances this takes 2-4 iterations. The process is stopped after 10 iterations if it fails to converge.

The starting values for the positions and energies are found by assuming that the clusters are isolated, i.e. the overlapping blocks are double-counted. Since the central blocks of the two clusters are local maxima in the detector, they are never in the overlap region, and hence they will never get counted twice. This is one of the primary difference between this case and the cluster splitting algorithm discussed below.

The weights, w_{ij}, are determined using the following rules. They are listed in order of descending priority, i.e. rule 1 overrides all subsequent rules.

1. The central block of each cluster is not shared with the other cluster:

   if i is the central block of cluster j then

$$w_{ij} = 1$$

$$w_{ik} = 0$$

2. If $D_{ij} < 3.5\ (blocks)^2$ and $D_{ik} < 3.5\ (blocks)^2$, then

$$w_{ij} = \frac{E_j e^{-(|\delta\theta_{ij}|+|\delta\phi_{ij}|)/0.17}}{E_j e^{-(|\delta\theta_{ij}|+|\delta\phi_{ij}|)/0.17} + E_k e^{-(|\delta\theta_{ik}|+|\delta\phi_{ik}|)/0.17}}$$

$$w_{ik} = \frac{E_k e^{-(|\delta\theta_{ik}|+|\delta\phi_{ik}|)/0.17}}{E_j e^{-(|\delta\theta_{ij}|+|\delta\phi_{ij}|)/0.17} + E_k e^{-(|\delta\theta_{ik}|+|\delta\phi_{ik}|)/0.17}}$$

The distances $\delta\theta_{ij}$ and $\delta\phi_{ij}$ are measured from the the middle of block i to the position of cluster j determined in the previous iteration, and $D_{ij} \equiv (\delta\theta_{ij})^2 + (\delta\phi_{ij})^2$. The energy in a given block due to one of the showers should be proportional to the energy of that shower, decaying exponentially according to the shower profile with increasing distance from the shower center. Since the shower cores are contained in the central blocks of the clusters, the characteristic length scale is that of the shower tails, ≈ 0.17 *blocks*, (see table 5.1, parameters x_B and y_B).

3. If $D_{ij} < D_{ik}$ and $D_{ij} < 4.5\ (blocks)^2$, then

$$w_{ij} = 1$$

$$w_{ik} = 0$$

4. If $D_{ij} > 4.5\ (blocks)^2$ and $D_{ik} > 4.5\ (blocks)^2$, then

$$w_{ij} = 0$$

$$w_{ik} = 0$$

5.2.4 Cluster Splitting Routine

For highly symmetric decays of $\pi^0 s$ from $\bar{p}p \rightarrow \pi^0\pi^0$ events, the minimum opening angle for the two photons is approximately 1.5 "blocks". Figure 5.2 shows

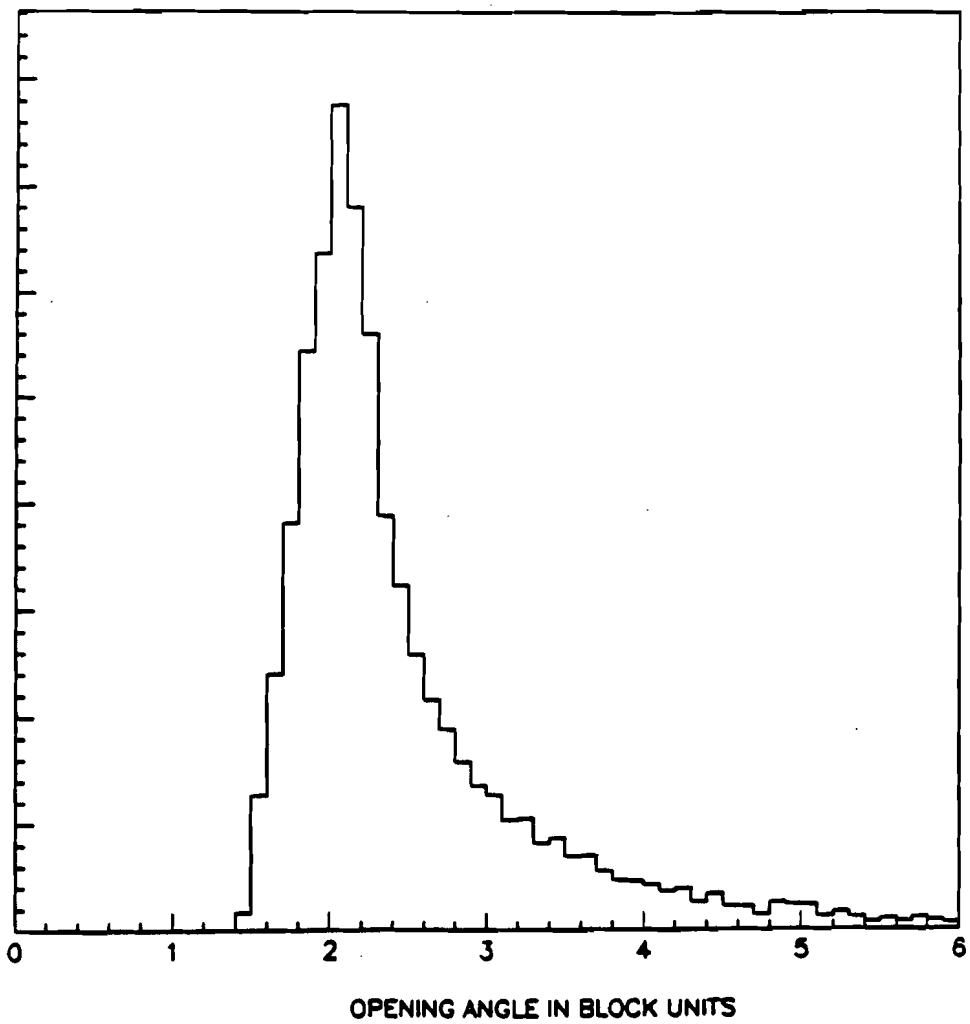

Figure 5.2: Opening angle of photons from π^0 decay, in the laboratory frame. in block units. The data shown are from $\bar{p}p \rightarrow \pi^0\pi^0$ events collected at $\sqrt{s} = 3685\ MeV$

the distribution of opening angles, in block units, for $\pi^0\pi^0$ events collected at the highest energy E760 typically operates at, $\sqrt{s} = 3685\ MeV$. Although it is very unlikely that the two photons hit adjacent blocks (ones with a common side), it

is rather common for the two photons to hit blocks that meet on their corners ($\Delta_{ring} = 1$ and $\Delta_{wedge} = 1$). When this occurs, there is typically only one local maximum for the energy deposition and the main clustering algorithm will treat it as a single electromagnetic shower. Fortunately such energy depositions will have a large cluster *mass*, defined by

$$m = \sqrt{\left(\sum_i E_i\right)^2 - \left(\sum_i \vec{p}_i\right)^2} \tag{5.7}$$

where E_i is the energy deposited in the i^{th} block and $\vec{p}_i = E_i \hat{x}_i$, where $\hat{x}_i$ is the unit vector from the interaction point to the center of the i^{th} block. The cluster *mass* for photons from $\overline{p}p \rightarrow \pi^0\pi^0$ events at $\sqrt{s} = 3686\ MeV$ and for electrons from $\overline{p}p \rightarrow J/\psi \rightarrow e^+e^-$ events are shown in figure 5.3. Energy depositions with a *mass* greater than 100 MeV are split into two clusters.

To split such depositions into two distinct clusters, the first order of business is to choose two cluster centers to work from. One will be the block the original isolated shower algorithm used. Since it is expected that the two photons have hit blocks touching in their corners, the four blocks on the corners of the original cluster central block are examined and the one with the largest energy deposition is taken to be the second cluster center. After this second cluster center is determined, this algorithm proceeds in a similar fashion as the cluster sharing routine discussed above.

Due to the high degree of overlap in the two electromagnetic showers in this case, some care must be taken. The first difficulty is finding the initial values of the positions and energies of the two clusters for the iterative procedure. The

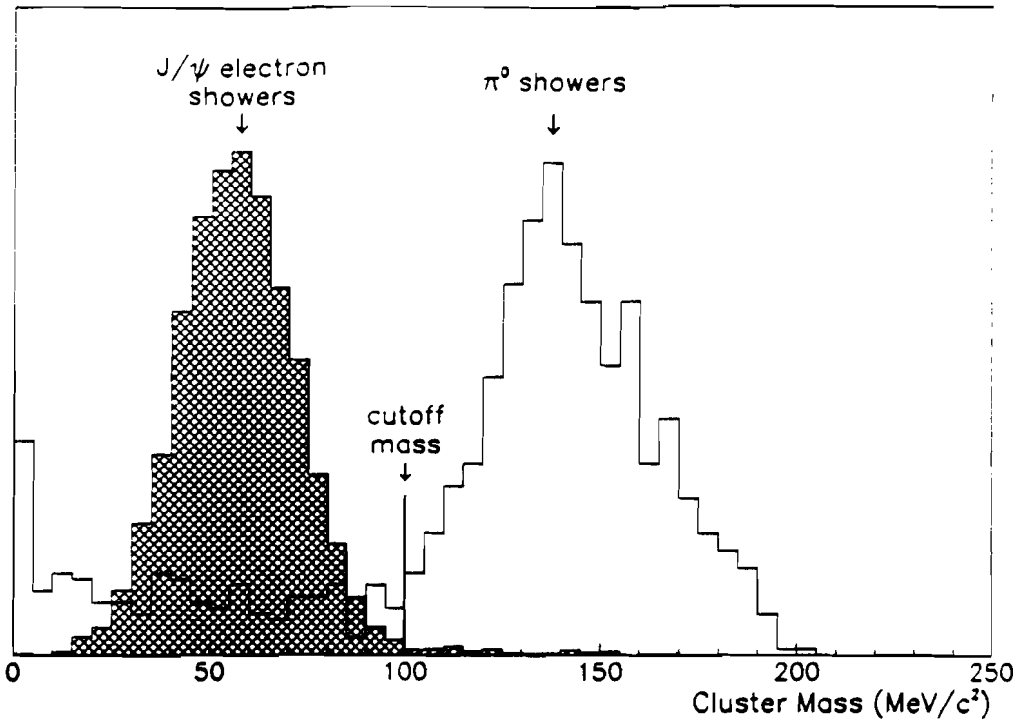

Figure 5.3: Cluster mass distribution

naive approach used in the cluster sharing routine, double-counting the blocks from the overlap region, will tend to return the same positions and energies for both showers. Once this has happened, it is very difficult for the algorithm to separate the two showers in any meaningful way. In order to avoid this tendency, the central block of each shower is not double-counted, as it would have been in the naive approach. This results in an initial overestimate of the separation of the clusters.

The next variation in this routine is that it uses a 5 by 5 grid for each cluster. This is to compensate for the fact that there is little information available from the tails of the showers on the side facing the adjacent shower, i.e. where the tail is sitting beneath the core of the other shower. The added lever arm on the side

away from the adjacent shower is crucial for getting reliable cluster positions. The rules used to determine the weighting functions, w_{ij}, listed in descending priority, are as follows:

1. The central block of each cluster is not shared with the other cluster:

   if i is the central block of cluster j, then

$$w_{ij} = 1$$

$$w_{ik} = 0$$

2. If $D_{ij} < 3.5\ (blocks)^2$ and $D_{ik} < 3.5\ (blocks)^2$, then

$$w_{ij} = \frac{E_j e^{-(|\delta\theta_{ij}|+|\delta\phi_{ij}|)/0.17}}{E_j e^{-(|\delta\theta_{ij}|+|\delta\phi_{ij}|)/0.17} + E_k e^{-(|\delta\theta_{ik}|+|\delta\phi_{ik}|)/0.17}}$$

   The distances $\delta\theta_{ij}$ and $\delta\phi_{ij}$ are measured from the the middle of block i to the position of cluster j determined in the previous iteration, and $D_{ij} \equiv (\delta\theta_{ij})^2 + (\delta\phi_{ij})^2$.

$$w_{ik} = \frac{E_k e^{-(|\delta\theta_{ik}|+|\delta\phi_{ik}|)/0.17}}{E_j e^{-(|\delta\theta_{ij}|+|\delta\phi_{ij}|)/0.17} + E_k e^{-(|\delta\theta_{ik}|+|\delta\phi_{ik}|)/0.17}}$$

   for determining the cluster energies and

$$w_{ij} = 0$$

$$w_{ik} = 0$$

   for determining the cluster positions. The energy in a given block due to one of the showers should be proportional to the energy of that shower, decaying

exponentially according to the shower profile with increasing distance from the shower center. Since the shower cores are contained in the central blocks of the clusters, the characteristic length scale is that of the shower tails, ≈ 0.17 *blocks*, (see table 5.1, parameters x_B and y_B).

3. If $D_{ij} < D_{ik}$ and $D_{ij} < 8.5\ (blocks)^2$, then

$$w_{ij} = 1$$

$$w_{ik} = 0$$

4. If $D_{ij} > 8.5\ (blocks)^2$ and $D_{ik} > 8.5\ (blocks)^2$, then

$$w_{ij} = 0$$

$$w_{ik} = 0$$

Note that in this case the blocks in the overlapping region are not used to calculate the cluster positions and that due to the increased grid size, 5 by 5 rather than 3 by 3, the limits in rules 3 and 4 have been increased from 4.5 $(blocks)^2$ to 8.5 $(blocks)^2$. As mentioned above, the cluster positions are determined by the tails of the showers which are obscured in the central region of the energy deposition by the cores of the two showers. These modifications are intended to compensate for this difficulty.

5.2.5 Clustering Algorithm Performance

There are two aspects to the performance of the clustering algorithm: the resolutions obtained for isolated electromagnetic showers, and the algorithm's ability to resolve photons from symmetric π^0 decays, returning accurate values of the shower energies and positions.

Isolated Showers

The energy and position resolution for isolated electromagnetic showers can be determined using the abundant supply of electrons from the reaction $\overline{p}p \rightarrow J/\psi \rightarrow e^+e^-$. The energy spectrum for these electrons is limited to the range 1.5 to 4.5 GeV so that other methods must be employed for the study of lower energy showers. However, they are an excellent tool for the study of the calorimeter performance since the charged tracking elements of the detector can be utilized to determine the true positions of the incident particles to ± 3.5 $mrad$ (full width in both θ and ϕ for "good" tracks), and the kinematics can be used to determine their energies very accurately.

The differences between the angles determined with the calorimeter and those determined by the charged tracking are plotted in figures 5.4 and 5.5. Only events with "good" charged tracks were included in this selection. After deconvolution of the average charged tracking error (2.5 $mrad$ rms in both θ and ϕ), the average resolutions for the central calorimeter are found to be $\overline{\sigma_\theta} = 5.7$ $mrad$ and $\overline{\sigma_\phi} = 12.3$ $mrad$. Figure 5.6 is a plot of $(\delta E/E)$, the difference between the pre-

dicted energy and the measured energy, divided by the predicted energy. The average electron energy for these events is 2.5 GeV. The distribution has a width $\sigma(\delta E/E) = 4.3\%$.

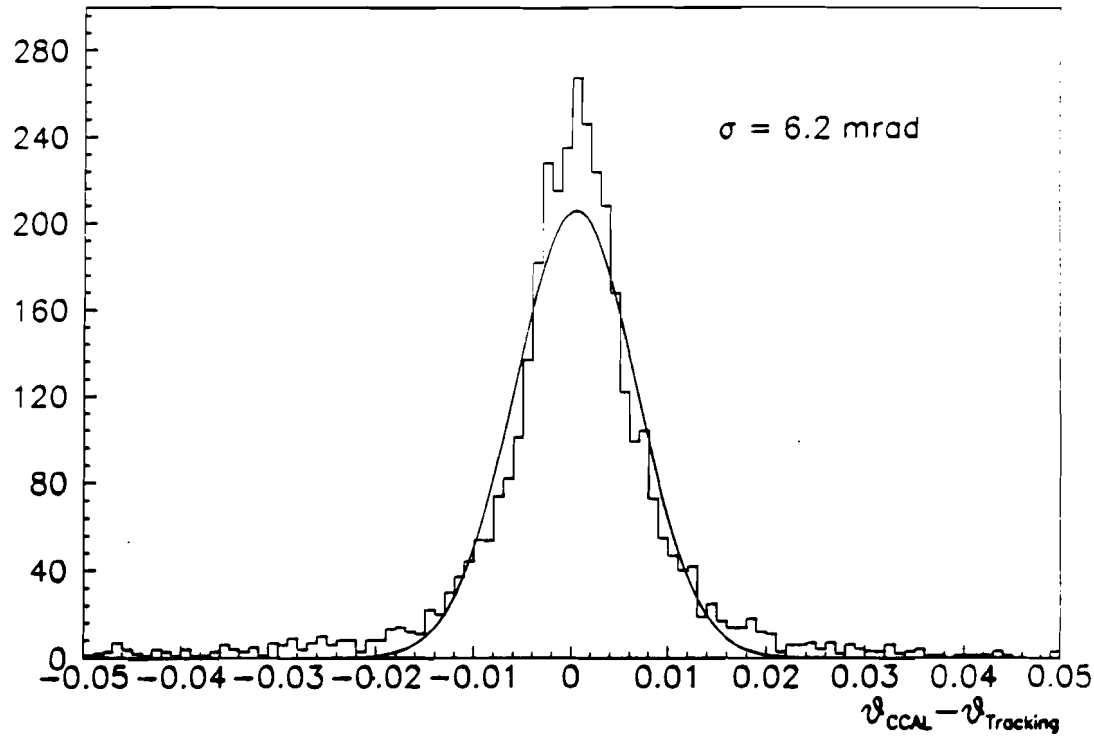

Figure 5.4: Average calorimeter angular resolution (θ)

The angular resolutions can be expressed in term of the intrinsic position resolution of the detector through the expressions

$$\sigma_\theta = \frac{\sigma_x}{r} \tag{5.8}$$

$$\sigma_\phi = \frac{\sigma_y}{r sin\theta} \tag{5.9}$$

where σ_x and σ_y are the position resolution in centimeters and r is the distance from the interaction region to the shower centroid, about 17 cm into the block. The implications of these expressions can be seen by examination of the calorimeter

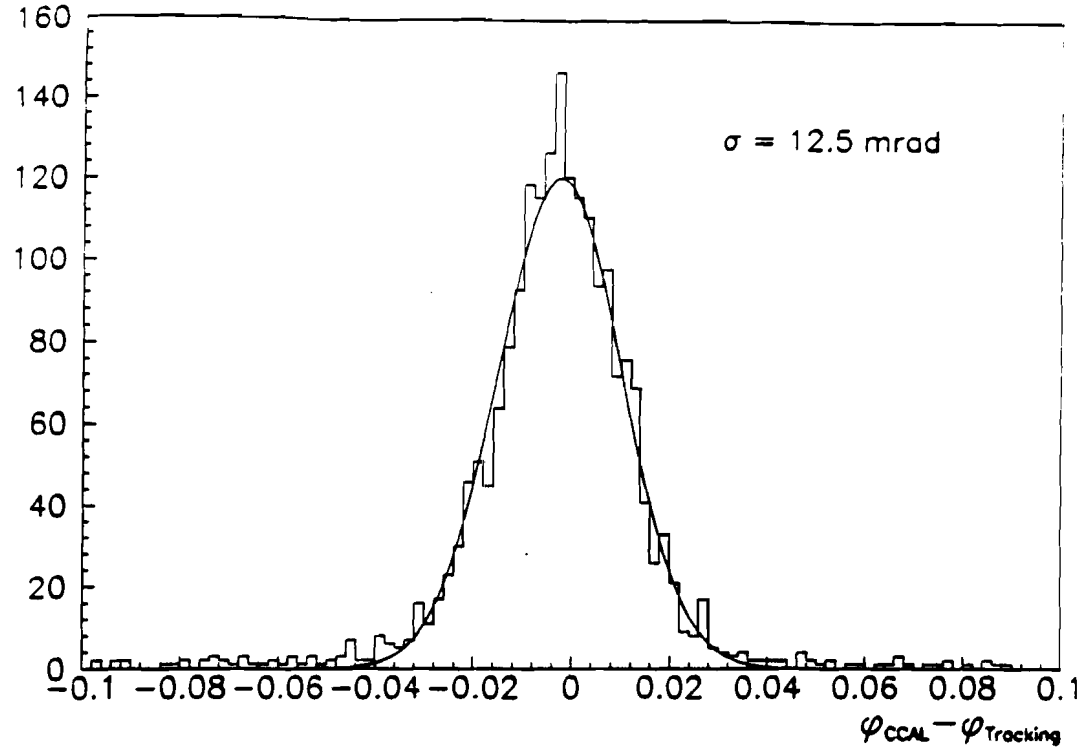

Figure 5.5: Average calorimeter angular resolution (ϕ)

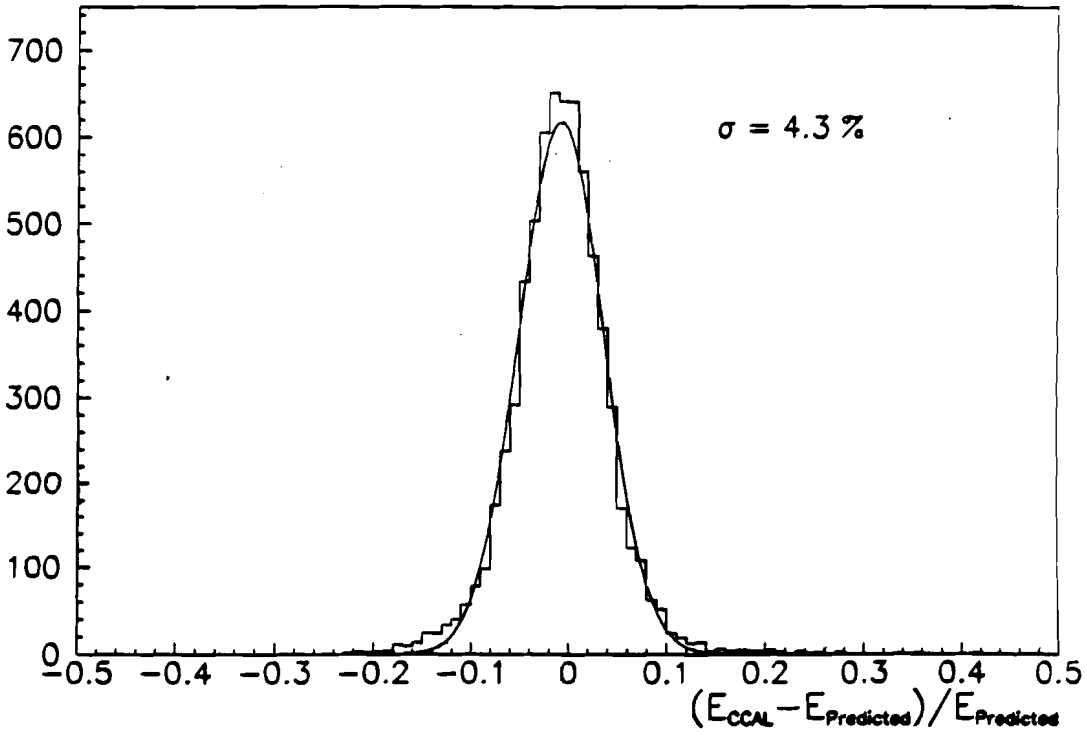

Figure 5.6: Average calorimeter energy resolution

geometry (see figure 5.1). For rings 1 to 14, the only region populated by electrons from charmonium decays, we see that $rsin\theta$ is essentially constant, so σ_ϕ is a constant over most of the detector. On the other hand, σ_θ is a continuously varying function of θ. The blocks are nearly square and the quantity of inactive material between blocks is similar in both directions, so σ_x and σ_y should be equal. Thus, there is a precise relation between the θ and ϕ errors.

The fine structures of the errors are parameterized with respect to the physical distances, δx and δy, of the incident particle from the nearest block edges in θ and ϕ, respectively. The parameterization is based on the data shown in figures 5.7 and 5.8. The position resolution functions obtained from the analysis of the these data are given by the following expressions.

$$\sigma_\theta = [3.40 + 1.51\ \delta x]\left[\frac{136.42}{r}\right] \tag{5.10}$$

$$\sigma_\phi = [5.90 + 2.62\ \delta y]\left[\frac{78.74}{rsin\theta}\right] \tag{5.11}$$

The lengths δx, δy, and r are in centimeters and the resolutions σ_θ and σ_ϕ are in milliradians. The values in the square brackets, 136.42 cm and 78.74 cm, represent the average values for r and $rsin\theta$ over rings 1 to 14. Note that the hypothesis that the position resolutions σ_x and σ_y (see equations 5.8 and 5.9) are equal is clearly valid, with $\sigma_x = (4.64 + .021\ \delta l)mm$ (where δl is the distance from the block edge in mm).

The energy resolution is strongly affected by energy lost in the inactive material between the blocks, so the energy resolution function has been parameterized in

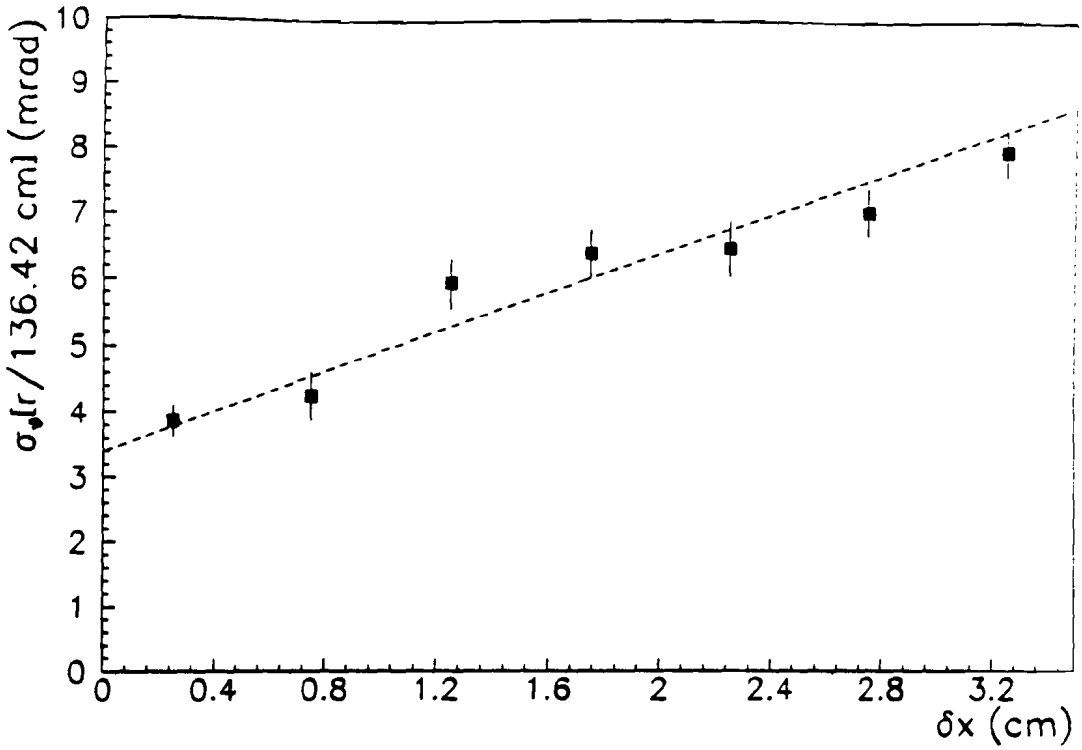

Figure 5.7: Fine structure of calorimeter angular resolution (θ)

terms of the energy correction used to compensate for that loss,

$$C \equiv \frac{E_{corrected} - E_{uncorrected}}{E_{uncorrected}}. \tag{5.12}$$

Figure 5.9 shows the energy resolution as a function of the crack correction, C. The average energy of the electrons in the plot is 2.5 GeV. The energy resolution is found empirically to be

$$\frac{\sigma_E}{E} = \frac{5.5\%}{\sqrt{E}} + 0.14\,C + \frac{0.005}{E}. \tag{5.13}$$

The first two terms come from a fit to the data shown in figure 5.9, while the last term, equivalent to 1 to 2 ADC counts, is included to account for pedestal fluctuations.

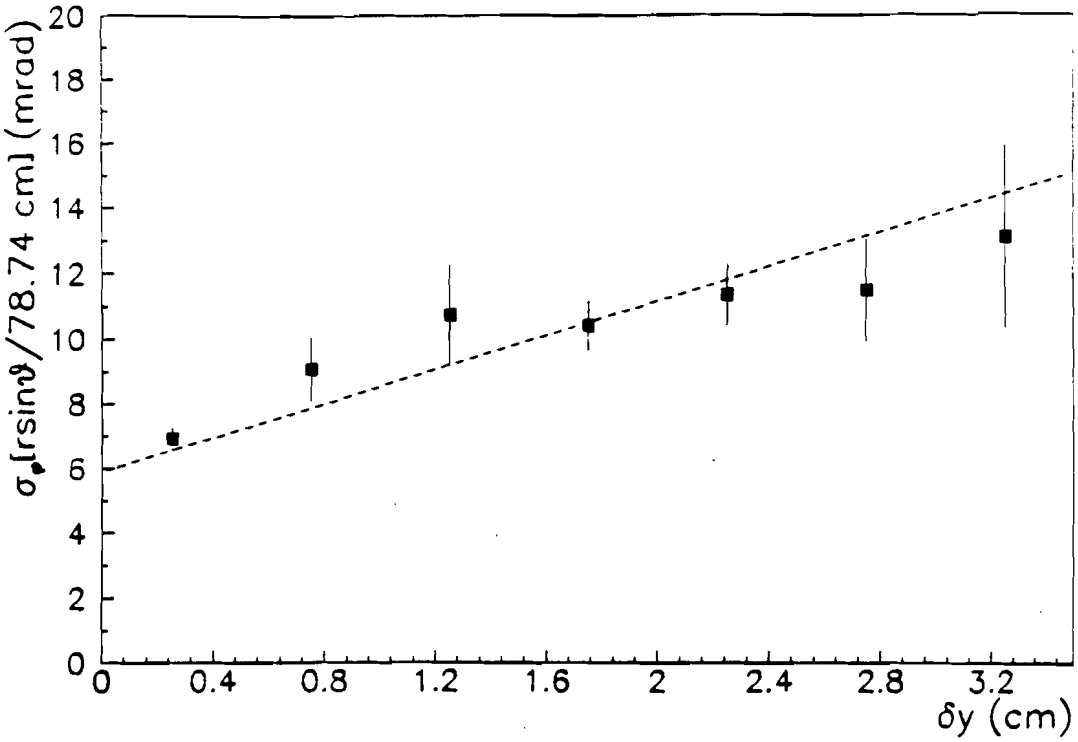

Figure 5.8: Fine structure of calorimeter angular resolution (ϕ)

Symmetric π^0 Decays

The cluster sharing and cluster splitting routines are designed expressly for the purpose of resolving photons from symmetric π^0 decays. The most challenging cases are the very energetic $\pi^0 s$ which come from the reaction $\bar{p}p \rightarrow \pi^0\pi^0$. A Monte Carlo was used to compare the distributions of several kinematical variables from this reaction with the expected distributions. The data are in good agreement with the Monte Carlo distributions. The distribution of the π^0 decay angle in the π^0 rest frame, given by the expression

$$|cos\theta^*| = \frac{|E_1 - E_2|}{\beta_{\pi^0}(E_1 + E_2)} \tag{5.14}$$

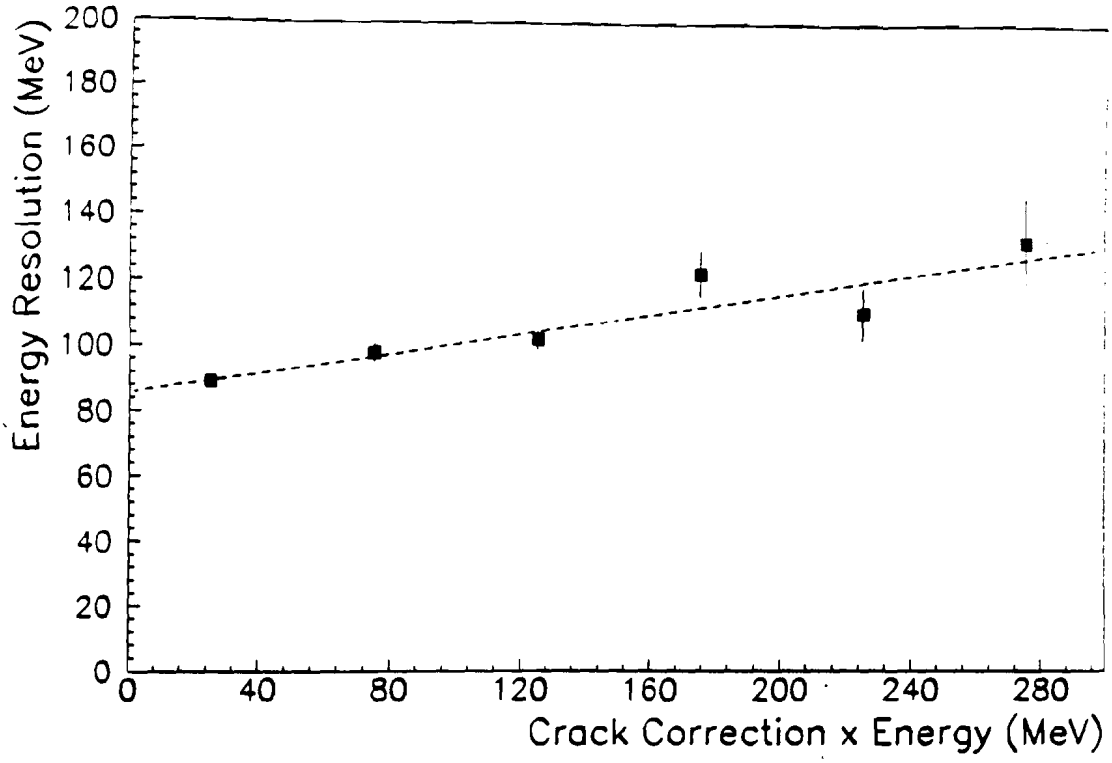

Figure 5.9: Energy resolution as a function of the crack correction

appears in figure 5.10. The distribution of this variable is expected to be flat over the range $0 \leq |cos\theta^*| \leq 1$. Deviations from this expected distribution near $|cos\theta^*| = 0$ would indicate that there is a problem with the reconstruction of symmetrically decaying $\pi^0 s$, while deviations near $|cos\theta^*| = 1$ would indicate a problem with the reconstruction of asymmetrically decaying $\pi^0 s$. Since the measured distribution is extremely flat, with no deficit near $|cos\theta^*| = 0$, the conclusion is that the cluster splitting routine is able to efficiently identify symmetric decays and that the cluster energies are being calculated accurately. There is a small deficiency near $|cos\theta^*| = 1$, which is due in part to the loss of photons below the detectors threshold, and also in part to the loss of photons outside of the detector

acceptance. I should note that the selection of the data used in figure 5.10 included a requirement that the reconstructed π^0 laboratory angles be in the range $15° \leq \theta_{lab} \leq 50°$. This was done to eliminate the large losses near $|cos\theta^*| = 1$ due to the loss of photons outside of the detector acceptance when a π^0 is near the edge of the calorimeter.

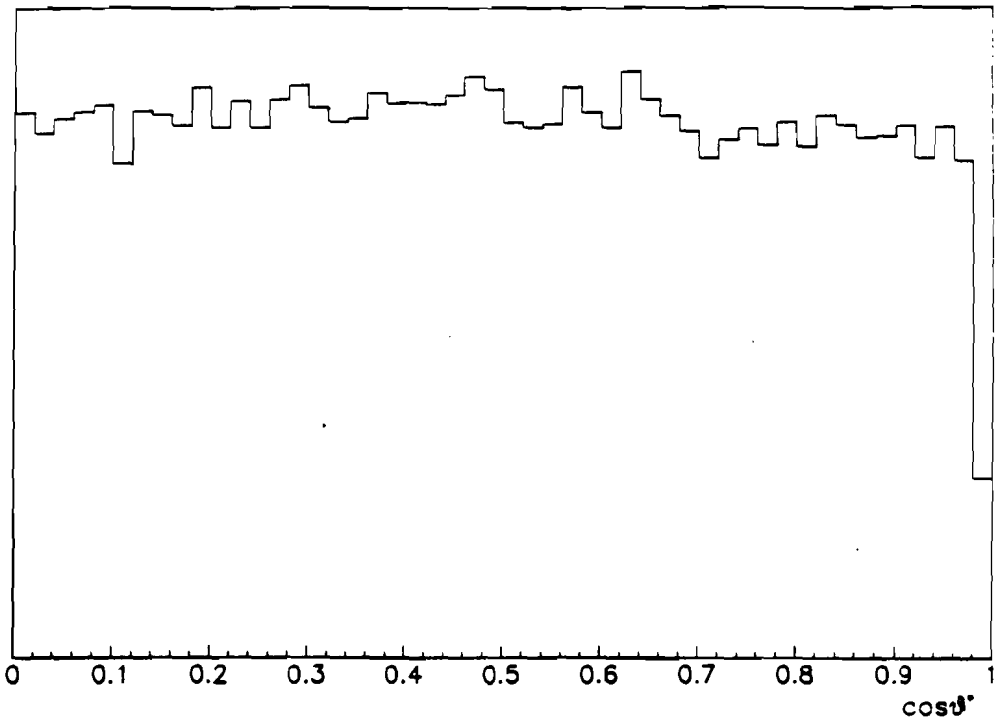

Figure 5.10: π^0 decay angle in the π^0 rest frame

From $\bar{p}p \rightarrow \pi^0\pi^0$ events at $\sqrt{s} = 3.556\ GeV$

5.3 Pile-up

"Pile-up" is defined to be clusters formed from signals not associated with the present physics event. It can pose a serious problem in distinguishing between the $\gamma\gamma$ signal and the hadronic backgrounds which tend to contain a π^0. There are two classes of pile-up which I will consider separately, although they are fundamentally equivalent.

The first class is the case in which a second interaction occurs *after* (within $\approx$ 100 *nsec*) an interaction of interest, i.e. an interaction which satisfies the hardware trigger requirements. This will generally result in events with high multiplicity and too much energy in the calorimeters. It is also likely that the second (unwanted) interaction will contain charged particles in the final state. These events do not pose a problem as background to the $\gamma\gamma$ channel, but do cause small inefficiencies in the trigger and analysis which have been accounted for in the efficiency calculations.

The second class of pile-up comes from situations where the tails of signals from a *previous* interaction are large enough to form calorimeter clusters in the triggered event. These clusters could be easily identified if each calorimeter channel were instrumented with a TDC or latch. Due to financial constraints, such a system was not implemented. However, the triggering system for the experiment provides 160 signals from the calorimeter, each consisting of the summed signal from 9 lead glass modules. These 160 signals are discriminated at a threshold corresponding to a cluster energy of $\approx$ 250 MeV. The discriminated signals are then read-out with

a set of pattern units with a 30 ns gate (for comparison, the central calorimeter's ADC gate length is 150 ns). In addition, 40 second level summed signals, each containing the sum of 5 of the 160 first level sums, are read-out with two sets of ADCs. One set is gated normally, while the other set has the signals delayed 50 ns relative to the gate. The ratio of the "delayed" and "on-time" sums gives some indication of when the signal was produced.

The pattern units provide the primary timing information. The system of delayed and on-time ADC read-out is used as a cross check and, in the event of a hardware problem in the pattern units, can be used to determine the timing information. The ADC read-out system suffers from two problems. First, the system samples rather large regions of the calorimeter (45 modules) so that it is common for more than one cluster to appear in a given region. Second, the method used to extract the timing of a cluster is to look at the ratio of the signals for the delayed and on-time ADCs. For lower energy clusters these signals are rather small; 1 ADC count represents about 20 MeV. Therefore fluctuations of 1 to 2 ADC counts in each measurement can change the ratio substantially.

Since neither system is able to reliably determine the timing for clusters below 200 MeV, I have decided to consider all clusters below 200 MeV to be of indeterminate timing (referred to as "undetermined").

Chapter 6

Event Selection and Analysis Efficiency

6.1 Introduction

The selection of $\gamma\gamma$ candidate events is straight forward. The first criterion is that the candidate photons conform to 2-body kinematics, to within the detector resolution. The remaining backgrounds are well understood. The majority of the background events come from the reactions $\bar{p}p \rightarrow \pi^0\gamma$ and $\bar{p}p \rightarrow \pi^0\pi^0$. In addition, small contributions come from $\bar{p}p \rightarrow \pi^0\eta$ and $\bar{p}p \rightarrow \eta\eta$ events. Thus the remaining selection criteria involve the removal of events that contain a possible π^0 or η.

6.2 Kinematical Cuts

The $\gamma\gamma$ candidate selection begins with events with two central calorimeter clusters with invariant mass $M_{\gamma\gamma} \geq 2.5\ GeV/c^2$. Up to two additional low energy clusters, classified as out-of-time or undetermined, are allowed in the central

calorimeter. No clusters are allowed in the forward calorimeter. The forward calorimeter veto is imposed since the background channels are highly peaked in the forward direction (see chapter 7), while the charmonium decays are not. In the case of the η_c and η_c', the center of mass angular distribution is isotropic. For the χ_2, the center of mass angular distribution is expected to be nearly isotropic, decreasing somewhat in the forward region (see section 6.4.1).

A 4C kinematical fit to the $\gamma\gamma$ hypothesis is done, and events with a fit probability $CL \leq 5 \times 10^{-3}$ are rejected. An invariant mass cut at $\pm 0.1\ \sqrt{s}$ is imposed, corresponding to 3σ of the mass resolution for $J/\psi \rightarrow e^+e^-$ events. The efficiency for this section of the analysis chain is $\approx 85\%$. Events with only 2 clusters that have passed these cuts are considered to be "good" $\gamma\gamma$ candidates. Those events that contain additional clusters are further analyzed as described in the next section.

6.3 π^0 and η Removal

At this point in the analysis a large number of events remain that have more than two clusters. These events will fall into two categories:

1. "good" $\gamma\gamma$ candidates that contain pile-up clusters
2. background events with asymmetric π^0 and/or η decays

In order to distinguish between these categories the masses calculated by pairing each additional low energy cluster with each of the high energy clusters (presumed

to be from the $\gamma\gamma$ decay) are determined. The masses formed in this way are shown in figure 6.1. Events with any mass in the range $80 - 170\ MeV/c^2$ are rejected. The masses from the remaining events, shown in figure 6.2., indicate remaining background from events with ηs. Events with a mass in the range $410 - 690\ MeV/c^2$ are rejected to remove this background.

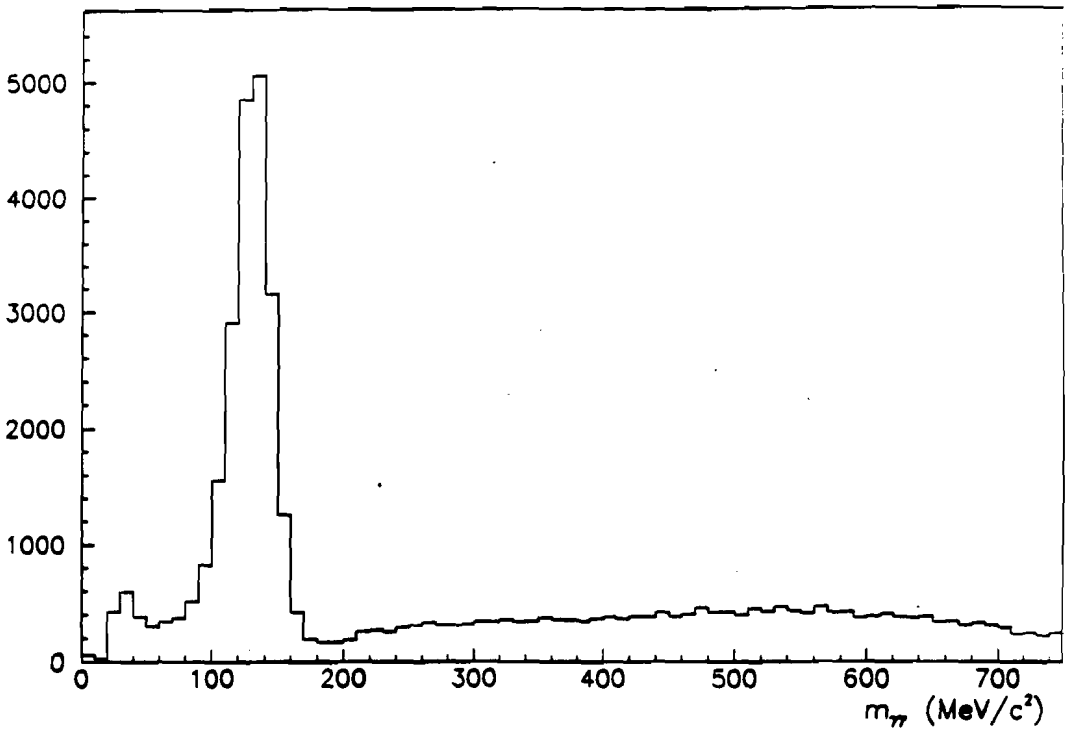

Figure 6.1: Mass spectrum of $\gamma\gamma$ candidate clusters with extra clusters

These windows are quite large. The rationale behind this is that these $\pi^0 s$ and ηs have decayed asymmetrically. In such cases, the mass resolution is dominated by the uncertainty in the energy of the low energy photon. For example, consider **a 3 GeV π^0 consisting of a 2.95 GeV photon and a 50 MeV photon. The mass**

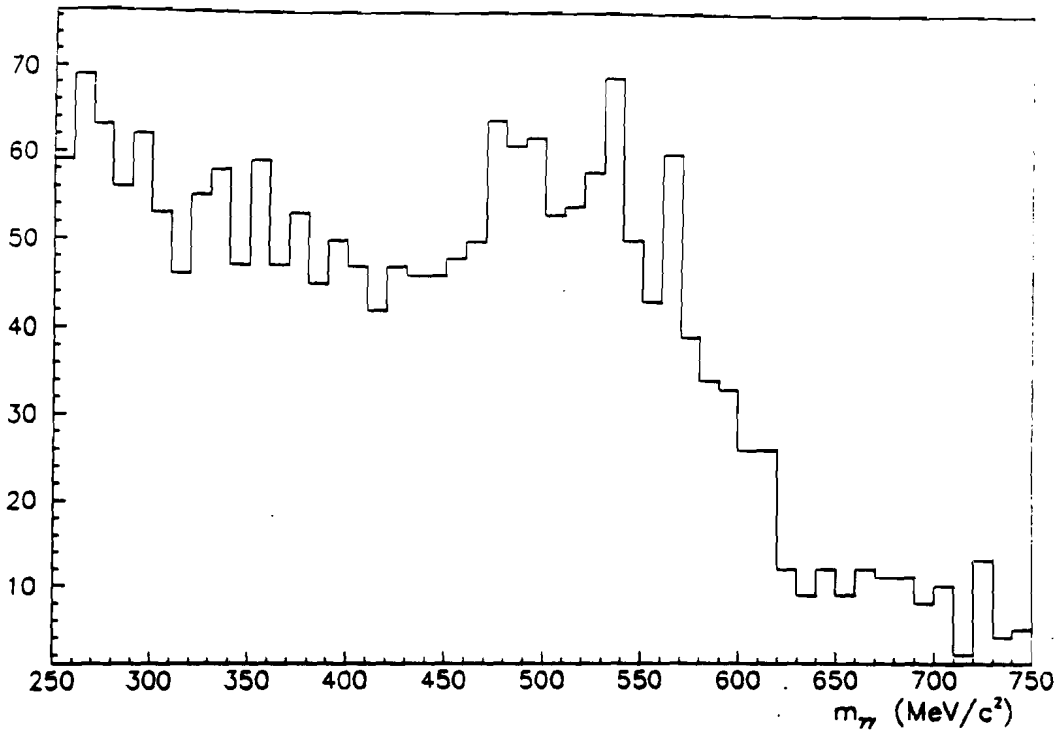

Figure 6.2: Mass spectrum of $\gamma\gamma$ candidate clusters with extra clusters after the removal of $\pi^0 s$

error is given by

$$\left(\frac{\sigma_m}{m}\right)^2 = \left(\frac{1}{2}\,\frac{\sigma_{E_1}}{E_1}\right)^2 + \left(\frac{1}{2}\,\frac{\sigma_{E_2}}{E_2}\right)^2 + \left(\frac{1}{2}\,\frac{sin\theta_{12}}{1-cos\theta_{12}}\,\sigma_{\theta_{12}}\right)^2 \qquad (6.1)$$

Due to the large boost, the opening angle θ_{12} is relatively small even for asymmetric decays, hence the last term is $\approx \left(\frac{\sigma_{\theta_{12}}}{\theta_{12}}\right)^2$. Since the low energy photon is likely to deposit energy only in one module of the calorimeter, the uncertainty in the opening angle will be dominated by the uncertainty in the position of that photon. Since the photons should be distributed uniformly over the face of any given block, that error is $\sigma = 1/\sqrt{12}$ *blocks* (the error for a uniform distribution over a unit interval). The minimum opening angle for an asymmetric π^0 decay is typically ≥ 2.5 *blocks*, so $\left(\frac{\sigma_{\theta_{12}}}{\theta_{12}}\right) \leq 0.12$. The cluster energy errors, on average, are given by

$\left(\frac{\sigma_E}{E}\right) = \frac{0.055}{\sqrt{E}} + 0.014 + \frac{0.005}{E}$. For a 2.95 GeV photon $\left(\frac{\sigma_E}{E}\right) = 0.05$ while for a 50 MeV photon $\left(\frac{\sigma_E}{E}\right) = 0.36$. The energy error for the low energy photon dominates and, in this case, 3σ corresponds to 64% of the particle mass. The efficiency of each of these mass cuts is $\approx 90\%$.

6.4 Acceptance Restriction

The final cut is to restrict the acceptance to a limited angular region in which the signal to background ratio is favorable. The background channels are strongly forward-backward peaked, and the point beyond which they increase rapidly is rather different at the η_c and the χ_2 (η_c') (see chapter 7). The cuts used in the final selections are $|cos\theta^*| \leq 0.40$ at the χ_2 and η_c', and $|cos\theta^*| \leq 0.20$ at the η_c. The choice for the χ_2 is described in the next section. The choice for the η_c is discussed in chapter 8.

To extract a peak cross section, or product of branching ratios, the data must be corrected for the restrictions in acceptance. In order to do this, the angular distributions for the reactions are needed. The cases of the η_c and η_c' are trivial; the distributions are isotropic since these are both spin 0 objects. The χ_2 angular distribution must be formally evaluated, with some theoretical input required in order to extract a numerical result.

6.4.1 The χ_2 Angular Distribution

Using the notation of reference [29], the angular distribution for the process $\overline{p}p \rightarrow \chi_2 \rightarrow \gamma\gamma$ is given by:

$$W(\theta) = (5/8)[K_1 + K_2 cos^2\theta + K_3 cos^4\theta]. \tag{6.2}$$

The coefficients K_1, K_2 and K_3 are related to the helicity amplitudes for the initial and final states. The initial state can have helicity=0 or helicity=1, with amplitudes B_0 and B_1 respectively, while the final state can be helicity=0 or helicity=2, with amplitudes A_0 and A_2 respectively. I will use the normalization conventions $A_0^2 + A_2^2 = 1$ and $B_0^2 + 2B_1^2 = 1$. The coefficients above are found to be

$$K_1 = [2A_2^2]R + [2A_0^2 + 3A_2^2](1 - R) \tag{6.3}$$

$$K_2 = [12A_0^2]R - 6[2A_0^2 + A_2^2](1 - R) \tag{6.4}$$

$$K_3 = -[12A_0^2 + 2A_2^2]R + 6[3A_0^2 + A_2^2](1 - R) \tag{6.5}$$

where $R = 2B_1^2/(B_0^2 + 2B_1^2)$. A full derivation of this distribution appears in appendix B.

The production amplitudes have been measured in the reaction $\overline{p}p \rightarrow \chi_2 \rightarrow J/\psi\gamma \rightarrow e^+e^-\gamma$. The best fit value is $R = 1$, with a 95% CL limit $R \geq 0.8$ [30]. The acceptance correction for a cut at $|cos\theta^*| \leq 0.4$ is not very sensitive to the value of R in the range $0.8 - 1.0$, varying by only 1-2%.

The shape of the angular distribution is very sensitive to the decay amplitudes, ranging from a distribution that is flat near the central region with a

decrease in the forward and backward directions ($A_0^2 = 0 \Rightarrow 1 - cos^4\theta$), to a distribution that is very strongly peaked in the forward and backward direction ($A_0^2 = 1 \Rightarrow cos^2\theta sin^2\theta$). The decay amplitudes cannot be measured directly. This in primarily due to the background, which is comparable to the signal in the central region, and completely swamps the signal in the forward and backward directions, i.e. for $|cos\theta^*| \geq 0.4$. Because of the lack of information in this region, it is impossible to distinguish between a large range of possible distributions. Fortunately, theoretical considerations all lead to similar conclusions and stringent limits can be placed on the ratio A_0^2/A_2^2. In the nonrelativistic limit, this ratio must vanish both in field theoretic and vector meson dominance (VMD) calculations. Relativistic corrections to all orders in $(\frac{v}{c})$ have been calculated [14] and it is found that $A_0^2/A_2^2 \leq 0.004$ for charmonium. The prediction of helicity=2 dominance has been tested in the light quark sector [31] where the relativistic corrections are larger. $A_0^2/A_2^2 \leq 0.047$, and the data support this hypothesis.

Summarizing, the production process has been found experimentally to be dominated by helicity=1, while theory predicts the decay to be dominated by helicity=2. Ignoring the helicity=0 components, the angular distribution is

$$W(\theta) = (5/4)[1 - cos^4\theta]. \qquad (6.6$$

The angular distribution for the $\gamma\gamma$ candidates at the χ_2 and for the background data near $\sqrt{s} = 3.525\ GeV$, scaled to the luminosity for the χ_2 data, are shown in figure 6.3. The inset shows the predicted angular distribution. A cut at $|cos\theta^*| \leq 0.40$ is imposed to achieve the most favorable signal to background

ratio, while maintaining as large a sample as possible to minimize statistical errors. The acceptance for this cut is found by integrating equation 6.6 over the

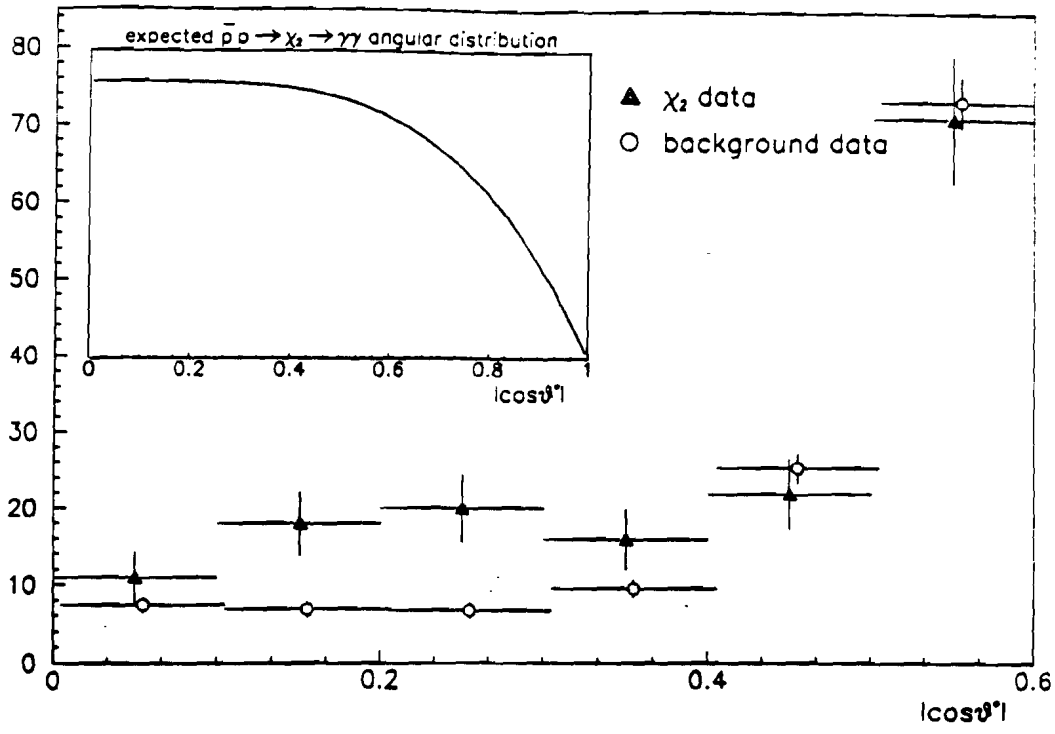

Figure 6.3: Angular distribution for $\gamma\gamma$ candidates at the χ_2

interval $|cos\theta^*| \leq 0.4$, $\alpha = 0.50 \pm 0.02$, where the error reflects the uncertainty in the magnitudes of the helicity=0 components.

6.5 Analysis Efficiency

The analysis efficiency was calculated using clean samples of J/ψ and ψ' events selected using the Čerenkov counter and hodoscopes. Approximately 5800 such events were used in this analysis. These data consisted of three independent samples that were analyzed separately and checked for consistency. The efficiencies

for the three samples are shown in table 6.1. The ψ' sample indicates that there may be some energy and/or luminosity dependence to the analysis efficiency. Unfortunately there are insufficient statistics (230 events at the ψ') to parameterize this in any meaningful way. The overall analysis efficiency, including both the kinematical and the π^0 and η mass cuts, is found to be $79 \pm 2 \pm 4\%$.

Cuts	J/ψ 1	J/ψ 2	ψ'
Kinematical	0.85	0.86	0.81
π^0, η Mass	0.82	0.84	0.77
All Cuts	0.78 ± 0.01	0.80 ± 0.01	0.73 ± 0.04

Table 6.1: Analysis efficiencies

Sixteen data points were taken in the region $\sqrt{s} = 3.522 - 3.572\ GeV$ during a search for the singlet-P state, h_c ($^1P_1$). These data were collected throughout the 1991 data taking period, interspersed between the data taking at the χ_2 and η_c', with the η_c data typically collected with the tail end of a $^1P_1$ or η_c' stack. Thus these data provide a good indication of the stability of the data collection and event selection, i.e. the trigger and analysis efficiencies, over time. The "measured" cross sections (events/luminosity) for these 16 points are plotted in figure 6.4.

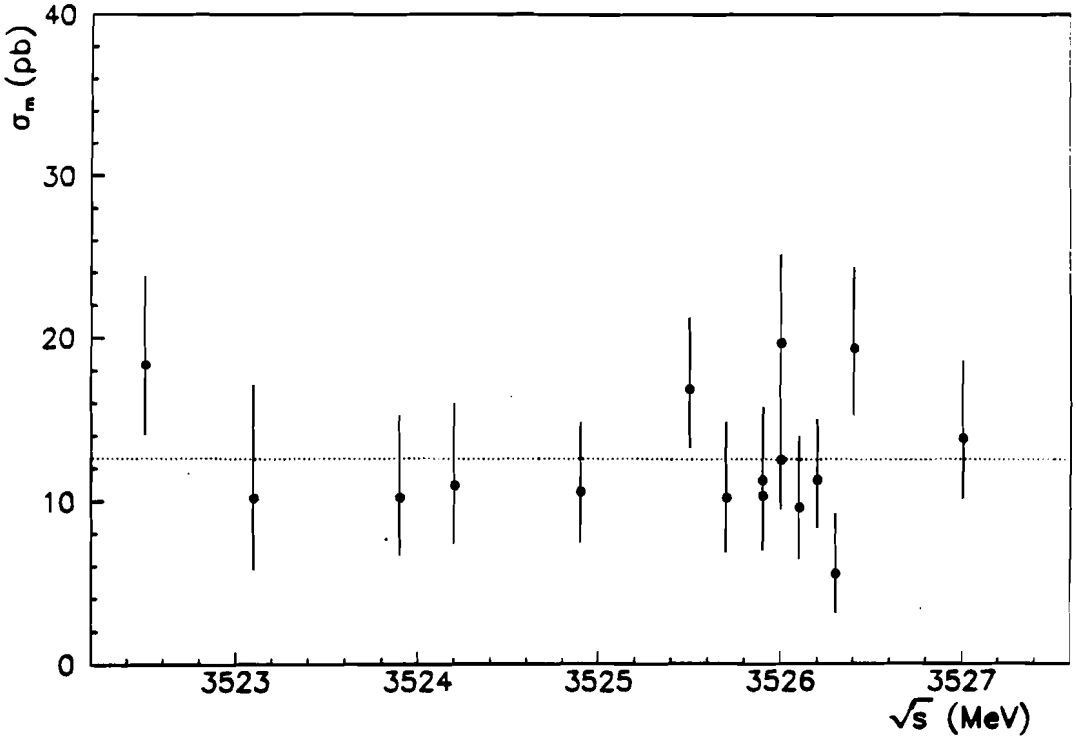

Figure 6.4: Stability of $\gamma\gamma$ triggering and analysis "measured" cross section for 16 stacks taken during the $^1P_1$ search

Chapter 7

Analysis of Background Sources

7.1 Introduction

The primary backgrounds to the $\gamma\gamma$ signal are $\bar{p}p \to \pi^0\pi^0$ and $\bar{p}p \to \pi^0\gamma$, with smaller contributions coming from $\bar{p}p \to \pi^0\eta$, $\bar{p}p \to \eta\eta$, and possibly $\bar{p}p \to \eta\gamma$. All of these processes can be measured directly with the data collected by E760. In this chapter the cross sections and angular distributions for the first two reactions are presented [32]. From these, an estimate of the expected background level for the $\gamma\gamma$ channel has been made. In the case of the χ_2, where the background is measured precisely, this provides only a cross check that the analysis chain and detector performance are well understood. In the case of the η_c, where the statistics of the off-resonance points are small, this analysis provides a constraint on the shape of the background as a function of $\sqrt{s}$. The predicted background levels are compared with the experimentally determined levels in chapter 8.

The latter three reactions, containing one or more η mesons, contribute only a small amount to the $\gamma\gamma$ background for the following three reasons; their cross sections are considerably lower than the channels containing only π^0s, the high

mass of the η makes the photons more easily differentiated kinematically from $\gamma\gamma$ photons, and the branching ratio of the η to $\gamma\gamma$ is only 40%.

7.2 Cross Sections and Angular Distributions for $\bar{p}p \rightarrow \pi^0\pi^0$ and $\bar{p}p \rightarrow \pi^0\gamma$

The excellent performance of the central calorimeter makes identification of fully contained $\pi^0\pi^0$ events almost trivial. Events with four clusters are selected and the photons are paired in the combination which produces the two "particles" which best fit the kinematics for the two-body reaction $\bar{p}p \rightarrow \pi^0\pi^0$. This selection relies solely on the colinearity of the reconstructed particles in the center of mass, and is independent of the invariant masses of the photon pairs. The kinematics for $\pi^0\pi^0$ and for $\eta\pi^0$ are very similar, so the latter reaction has not been entirely removed by the kinematical cuts. Selecting events with $M_{\gamma\gamma} \leq 250\ MeV$ leads to an almost background free sample of $\bar{p}p \rightarrow \pi^0\pi^0$ events. The invariant mass spectrum of the photon pairs thus selected are shown in figure 7.1. The π^0 peak is virtually free of combinatorial background. A mass cut at $M_{\gamma\gamma} = 135 \pm 35\ MeV$ is used to select the final sample. An equivalent analysis is done for three cluster events, in this case looking for kinematics that match the $\pi^0\gamma$ hypothesis. In either case, the photons were restricted to the region $0.20 < \theta < 1.13$ to avoid the poor energy and angular measurements near the edges of the detector's acceptance.

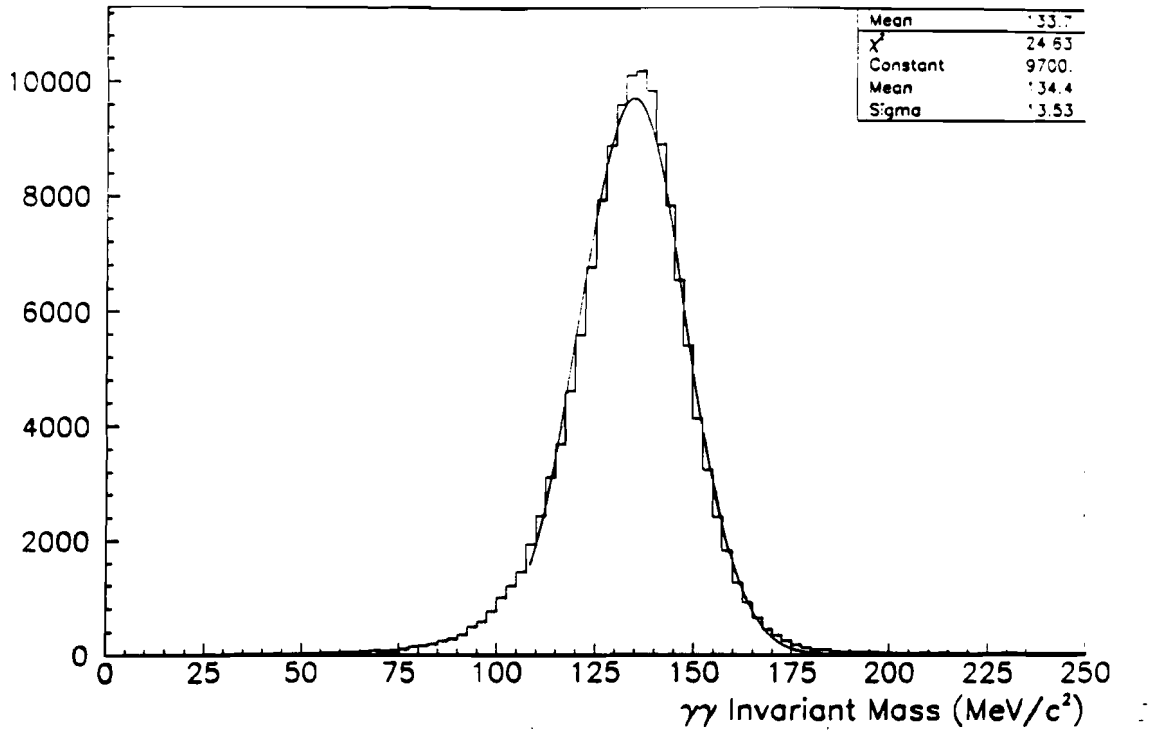

Figure 7.1: $\gamma\gamma$ mass spectrum from four cluster events

7.2.1 $\bar{p}p \rightarrow \pi^0\pi^0$

The measured differential cross section for fully contained (four cluster) $\bar{p}p \rightarrow \pi^0\pi^0$ events must be corrected for trigger efficiency, selection efficiency, and the effects of the geometrical acceptance of the detector and the detector threshold. The trigger efficiencies have been discussed in chapter 3, and are summarized in table 7.1 for the processes of interest to this discussion. The selection effi-

Process	Trigger Efficiency
$\bar{p}p \rightarrow \pi^0\pi^0$	0.87
$\bar{p}p \rightarrow \pi^0\gamma$	0.89

Table 7.1: Trigger efficiencies for $\pi^0\pi^0$ and $\pi^0\gamma$ events

ciency, 84%, is dominated by the first pass selection which uses the information from the on-line processors (ACPs) to create data summary tapes. The effects of the detector acceptance and threshold are determined using Monte Carlo events. These corrections are small, 6% – 9% with a 50 MeV threshold, except near the edges of the detector acceptance. The differential cross sections for $\bar{p}p \rightarrow \pi^0\pi^0$ at $\sqrt{s} = 2975\ MeV$ and $\sqrt{s} = 3525\ MeV$ appear in figures 7.2 and 7.3, respectively.

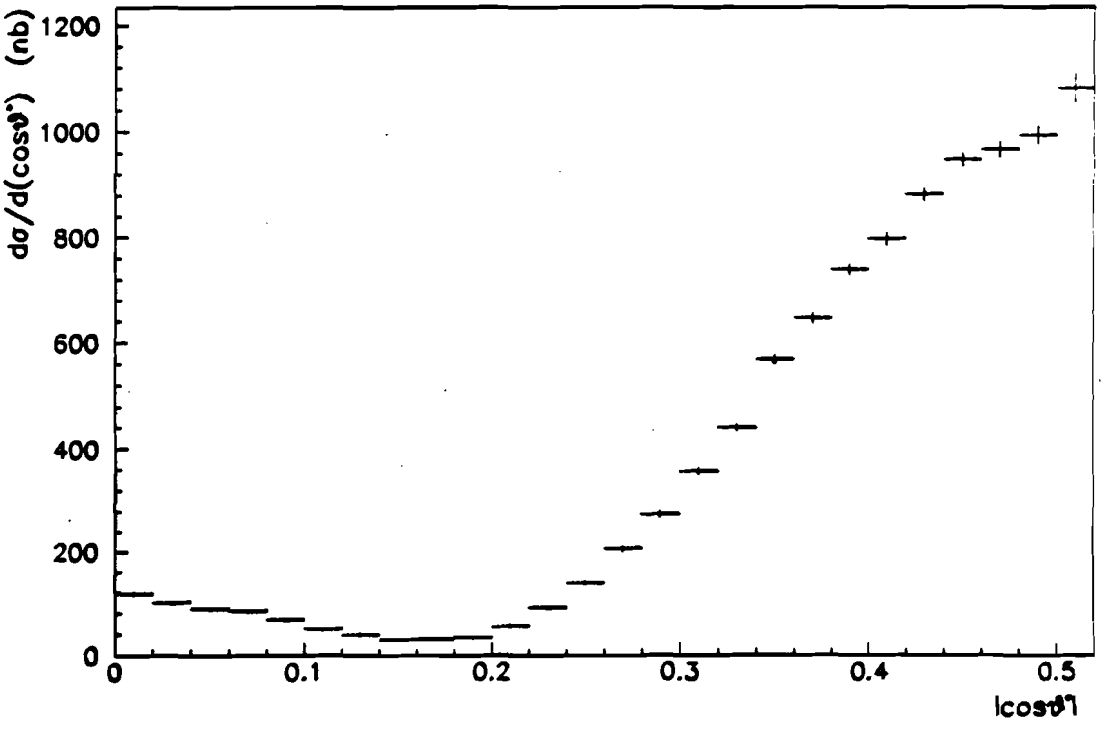

Figure 7.2: Differential cross section for $\bar{p}p \rightarrow \pi^0\pi^0$ at 2975 MeV

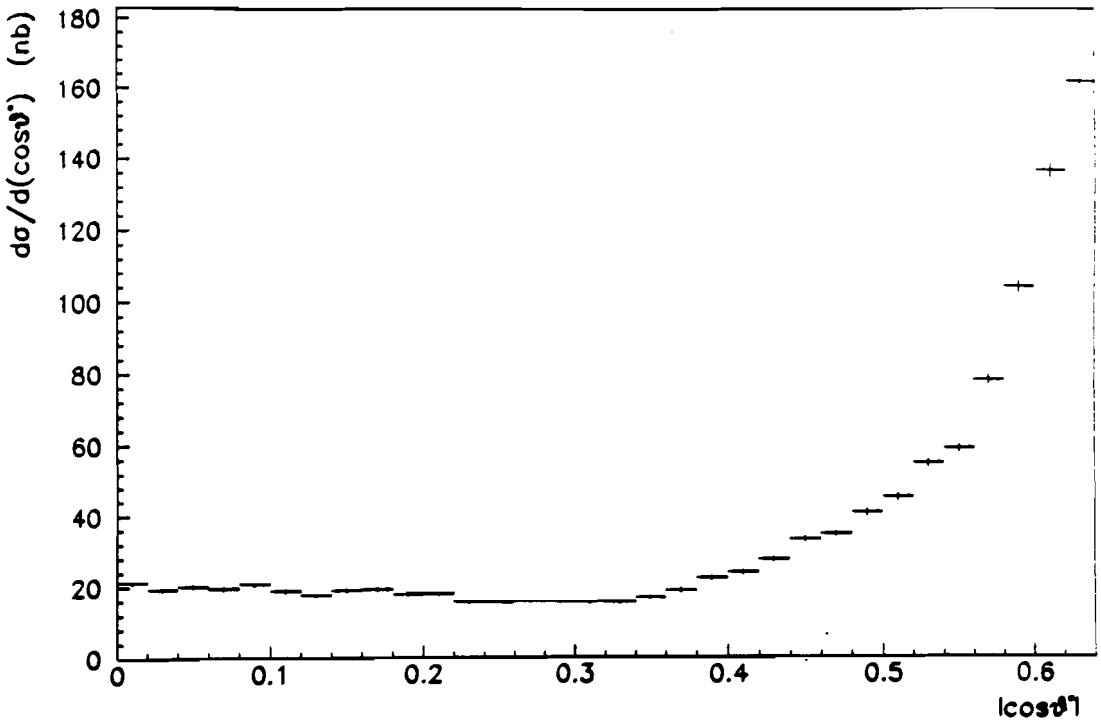

Figure 7.3: Differential cross section for $\bar{p}p \rightarrow \pi^0\pi^0$ at 3525 MeV

7.2.2 $\bar{p}p \rightarrow \pi^0\gamma$

The situation for the reaction $\bar{p}p \rightarrow \pi^0\gamma$ is more complicated since there is a large background coming from $\bar{p}p \rightarrow \pi^0\pi^0$ events with a missing photon (either below threshold or outside the detector acceptance). The background to $\bar{p}p \rightarrow \pi^0\gamma$ is modeled using the measured $\bar{p}p \rightarrow \pi^0\pi^0$. The difficulty is that, while the fraction of $\pi^0\pi^0$ events with only 3 photons detected is small, $\sim 7\%$, the precise value of this fraction is very sensitive to the detector threshold. Of the observed 3γ events, approximately 1/3 of them are background from $\pi^0\pi^0$. For the threshold used in this analysis, 50 MeV, the number of $\pi^0\pi^0$ events for which only 3 photons are observed varies by $\approx 1.5\%$ (out of $\approx 7\%$) for a 10 MeV change in the threshold.

This leads to the possibility of large errors, on the order of 20% to 25%, in the calculation of the background to $\pi^0\gamma$ events. Thus a good understanding of the true detector threshold is needed.

Several methods have been used to investigate nonlinearities in the energy scale at low energies. The recoil photons from the radiative decays of the χ_2 state range in energy from 300 MeV to 1.3 GeV. Since the kinematics uniquely determine the photon energy at a given lab angle, these [illegible]s provide a good test of the linearity of the energy over this intermediate range of energies. Analysis of these data show no evidence of deviations from a linear energy scale, at the 1% level, for this energy range. A single low energy point was examined using test beam data. Data were taken with 84 MeV electrons at the University of Illinois at Urbana-Champaign, and with 1 GeV to 4 GeV electrons at Brookhaven National Laboratory. On the energy scale determined by linearly extrapolating the high energy points to zero, the 84 MeV electron peak was $\approx$ 10% low. The final technique used was to examine the masses of reconstructed $\pi^0 s$ as a function of the minimum photon energy (see figure 7.4). This technique has the advantage that the data cover a wide range of photon energies, from the detector threshold to 800 MeV, with virtually unlimited statistics. These data indicate a small nonlinearity in the energy scale below $\approx$ 200 MeV. Assuming that the mass error comes completely from inaccurate measurement of the energy of the low energy photon, there is about an 8 MeV error in the energy scale at 50 MeV, i.e. a photon which is designated as 50 MeV is really $\approx$ 58 MeV.

The conclusion from these analyses is that there is a nonlinearity near the low end of the energy scale, below $\approx 200\ MeV$. This effect is on the order of 10% to 15% near the threshold used in this analysis, 50 MeV. As indicated above, such an uncertainty in the energy scale near threshold will result in about a 20% error in the (calculated) amount of background to the $\pi^0\gamma$ channel coming from $\pi^0\pi^0$ events. Since this background constitutes about 1/3 of the observed events, this results in about a 10% systematic error in the $\pi^0\gamma$ cross section. For my purposes, namely to constrain the shape of the $\gamma\gamma$ background, I do not need to know the absolute cross sections to better than 10%, so these systematic errors have been neglected. The differential cross sections for $\bar{p}p \rightarrow \pi^0\gamma$ at $\sqrt{s} = 2975\ MeV$ and $\sqrt{s} = 3525\ MeV$ appear in figures 7.5 and 7.6, respectively.

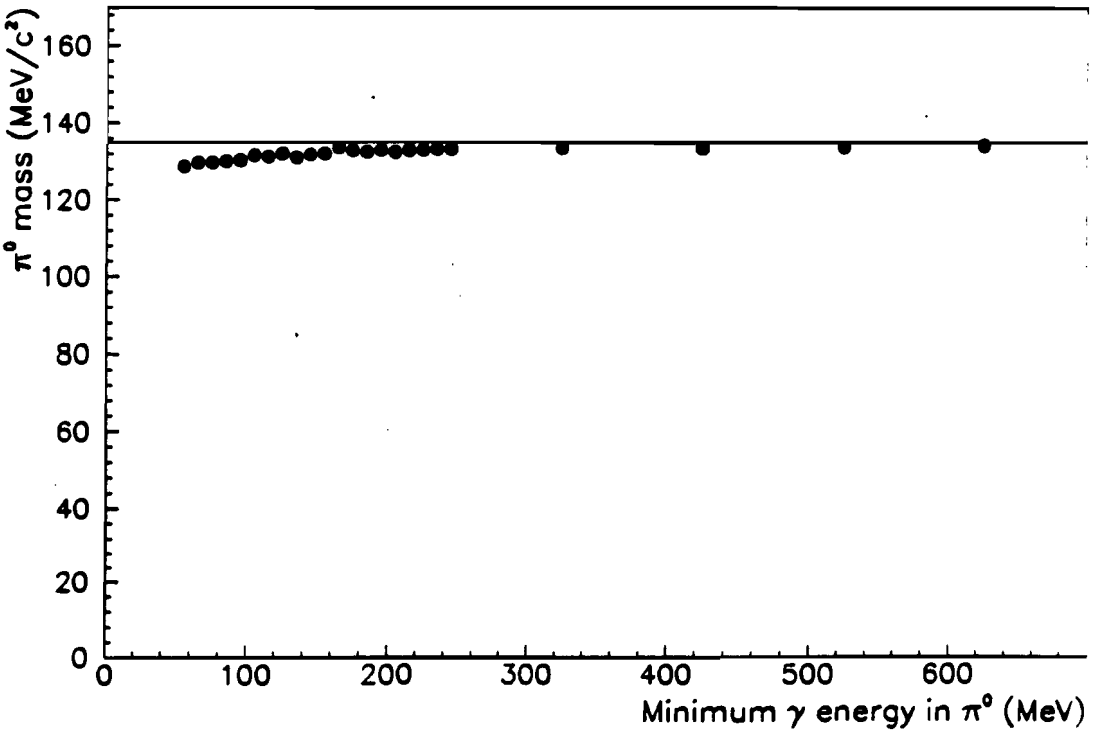

Figure 7.4: Reconstructed π^0 mass as a function of the minimum photon energy

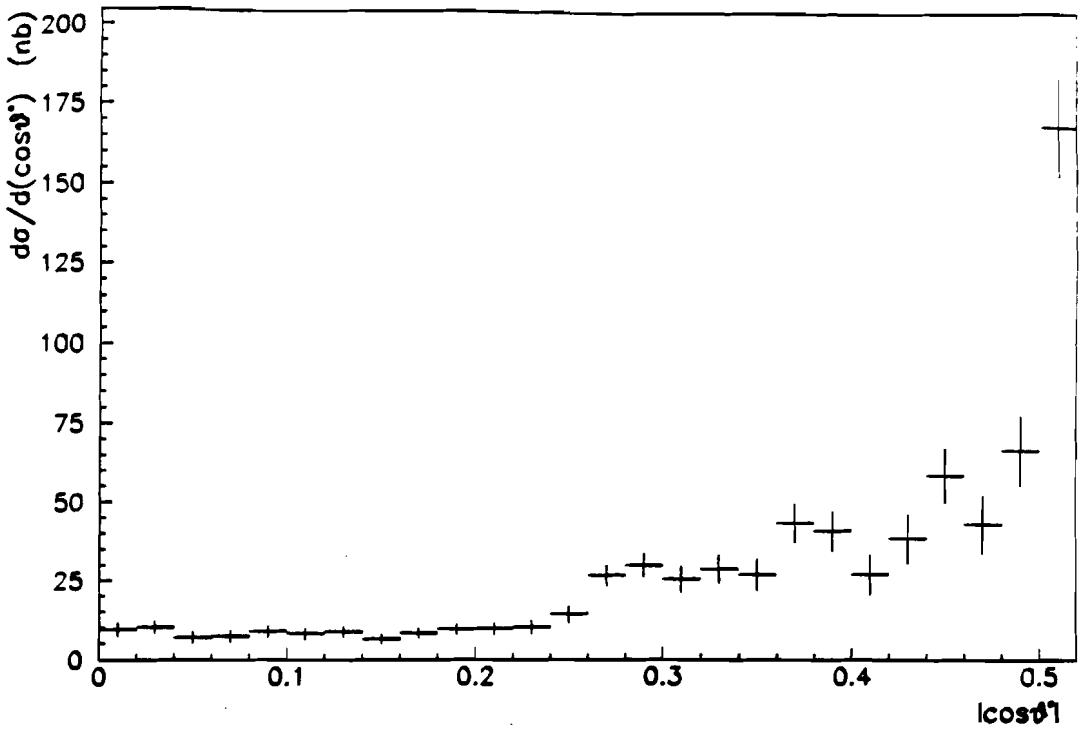

Figure 7.5: Differential cross section for $\bar{p}p \rightarrow \pi^0\gamma$ at 2975 MeV

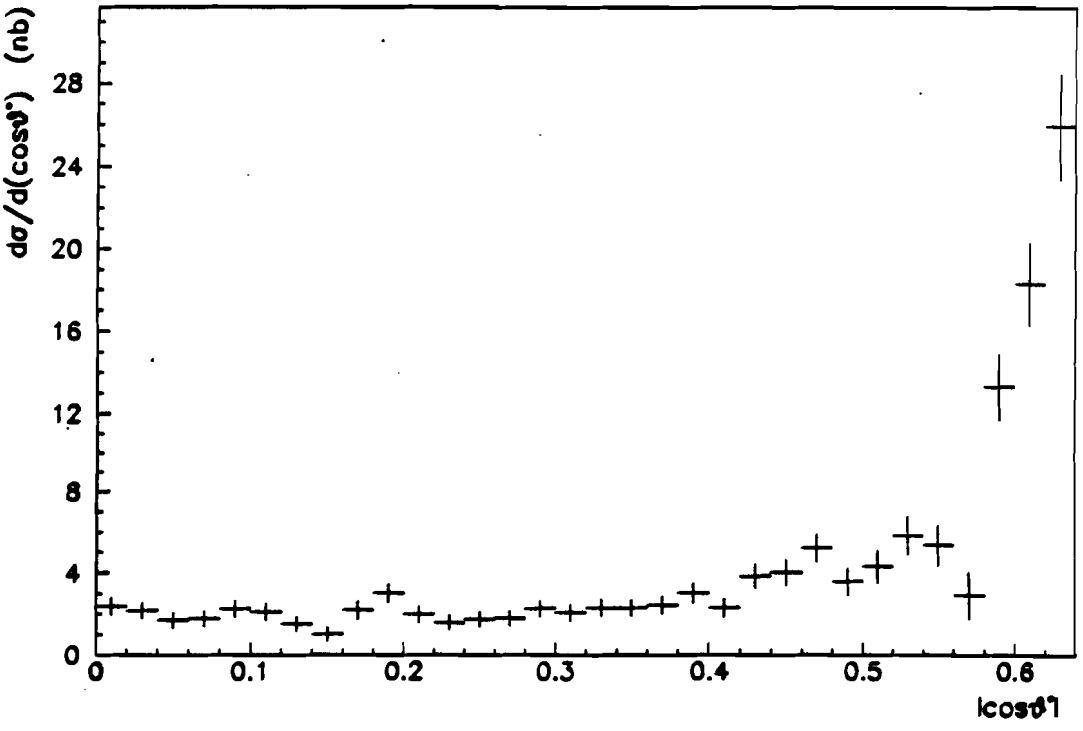

Figure 7.6: Differential cross section for $\bar{p}p \rightarrow \pi^0\gamma$ at 3525 MeV

Chapter 8

Results and Conclusions

8.1 Likelihood Fits to the Data

For each data point taken there is a measured center of mass energy, center of mass energy spread, luminosity, and number of events. These data were fit for a smooth background plus a Breit-Wigner line shape convoluted with the beam energy spread. The resonance parameters used in the fits were the mass, M, total width, Γ, and the parameter

$$\sigma_m \equiv \frac{(2J+1)\pi}{k^2} BR_{IN} BR_{OUT} \times efficiency \times acceptance \qquad (8.1)$$

which represents the measured cross section (events/luminosity) at the peak of the resonance (for $\Gamma_{res} \gg \Gamma_{beam}$).

8.1.1 η_c Results

The data used in the η_c fits appear in table 8.1. Due to the limited statistics of the background data for the η_c resonance, and because the mass and total width are not precisely known, it is impossible to do a global fit to both the resonance

$\sqrt{s}\ (MeV)$	Events	$\int \mathcal{L}\ (nb^{-1})$	Events/$\int \mathcal{L}\ (pb)$
2911	3	49.11	61.1
2950	11	197.45	55.7
2975	26	423.91	61.3
2979	13	165.30	78.6
2981	31	392.64	79.0
2985	13	200.15	65.0
2990	52	513.01	101.4
2995	25	308.89	80.9
3005	24	510.71	47.0
3050	4	110.63	36.2
3097	19	690.27	27.5

Table 8.1: Final $\gamma\gamma$ candidates for the η_c

and background. Therefore, the background was constrained using the measured $\pi^0\pi^0$ and $\pi^0\gamma$ cross sections (discussed in chapter 7) and a simple Monte Carlo to predict the cross section for $\gamma\gamma$ candidates due to these sources. These predicted values were fit using the form:

$$\sigma_{predicted} = A\left(\frac{2988\ MeV}{E_{CM}}\right)^B + C. \tag{8.2}$$

The best fit values are $A = 23.6\ pb$, $B = 44.5$ and $C = 12.3\ pb$ for an acceptance restriction $|cos\theta^*| \leq 0.20$.

Two fits were done to the $\gamma\gamma$ data at the η_c using different background parameterizations. The mass, total width, and the parameter σ_m (equation 8.1) were allowed to vary in both fits. Each fit had one free parameter for the background. The background paramterizations used were:

$$\sigma_{bkg} = \sigma_{predicted} + D \tag{8.3}$$

$$\sigma_{bkg} = \sigma_{predicted} \times E. \tag{8.4}$$

The fit results are:

$$M = 2989.8 \pm 2.3\ MeV \tag{8.5}$$

$$\Gamma = 15.6 \pm 6.7\ MeV \tag{8.6}$$

$$\sigma_m = 54.6 \pm 11.2^{p}b \tag{8.7}$$

$$D = 8.9 \pm 5.7\ pb \tag{8.8}$$

with $\chi^2 = 3.1/6\ dof$, and

$$M = 2990.1 \pm 2.0\ MeV \tag{8.9}$$

$$\Gamma = 15.5 \pm 6.4\ MeV \tag{8.10}$$

$$\sigma_m = 54.7 \pm 13.7\ pb \tag{8.11}$$

$$E = 1.25 \pm 0.22 \tag{8.12}$$

with $\chi^2 = 4.7/6\ dof$. The data and fitted curves are shown in figure 8.1.

The stability of the η_c results was checked using acceptance restrictions of $|cos\theta^*| \leq 0.10$, $|cos\theta^*| \leq 0.15$, $|cos\theta^*| \leq 0.20$, and $|cos\theta^*| \leq 0.25$; performing the likelihood analyses described above on each of these data sets. The resonance parameters from the eight fits appear in table 8.2. The mass and product of branching ratios are quite stable for the eight fits, but the total width varies strongly with the $|cos\theta^*|$ cut. The final results for the η_c resonance parameters are taken from the $|cos\theta^*| \leq 0.20$ sample, while the other results are used to estimate systematic errors due to event selection and fitting.

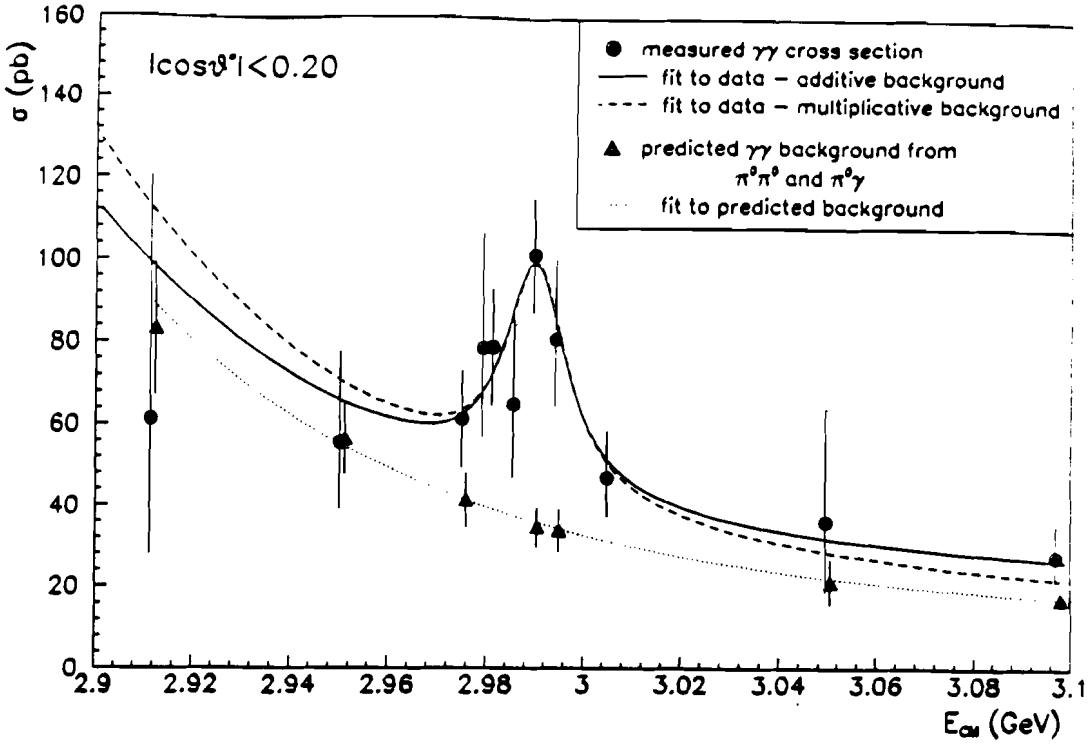

Figure 8.1: Fits to η_c data

The results are:

$$M = 2989.9 \pm 2.2 \pm 0.4\ MeV \tag{8.13}$$

$$\Gamma = 15.6 \pm 6.9 \pm 6.4\ MeV \tag{8.14}$$

$$\sigma_m = 54.6 \pm 14.5 \pm 7.8\ pb. \tag{8.15}$$

Branching ratios and partial widths derived from these results are presented in section 8.2.

Comparisons of these measurements of the mass and total width of the η_c with previous measurements appear in figures 8.2 and 8.3. The $J/\psi - \eta_c$ mass splitting provides a direct measure of the hyperfine splitting in charmonium. However, since this is the only hyperfine splitting for which experimental data has been

$cos\theta^*$ cut	Mass (MeV)	Width (MeV)	$\sigma_m/acceptance$ (pb)	χ^2/dof
Additive Background Parameterization				
0.25	2989.8 ± 3.4	21.0 ± 10.5	179.5 ± 57.4	4.9/6
0.20	2989.8 ± 2.2	15.6 ± 7.1	272.8 ± 76.2	3.1/6
0.15	2990.6 ± 2.4	8.1 ± 7.9	273.6 ± 110.9	5.4/6
0.10	2990.0 ± 2.0	10.3 (*fixed*)	240.2 ± 93.9	8.4/7
Multiplicative Background Parameterization				
0.25	2989.7 ± 3.2	23.8 ± 10.7	193.2 ± 54.5	5.3/6
0.20	2990.1 ± 2.2	15.5 ± 6.4	273.3 ± 68.8	4.7/6
0.15	2990.7 ± 2.1	8.6 ± 7.4	278.1 ± 94.9	7.5/6
0.10	2990.1 ± 1.9	10.3 (*fixed*)	252.5 ± 99.8	9.3/7

Table 8.2: Fit parameters for the η_c

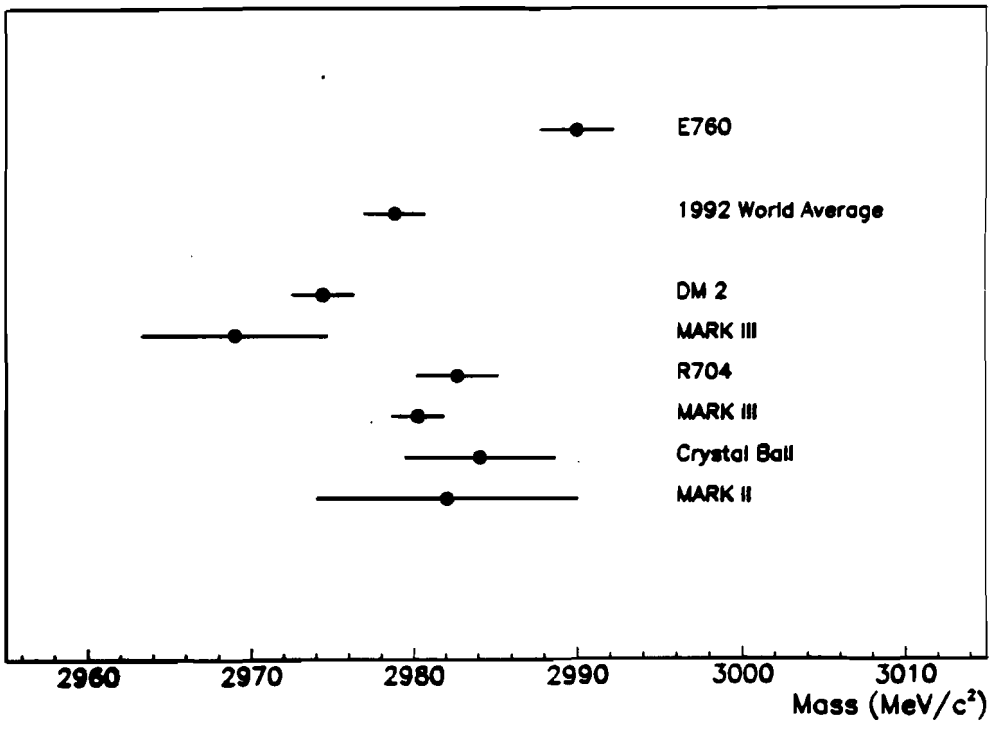

Figure 8.2: Comparison of η_c mass with previous measurements

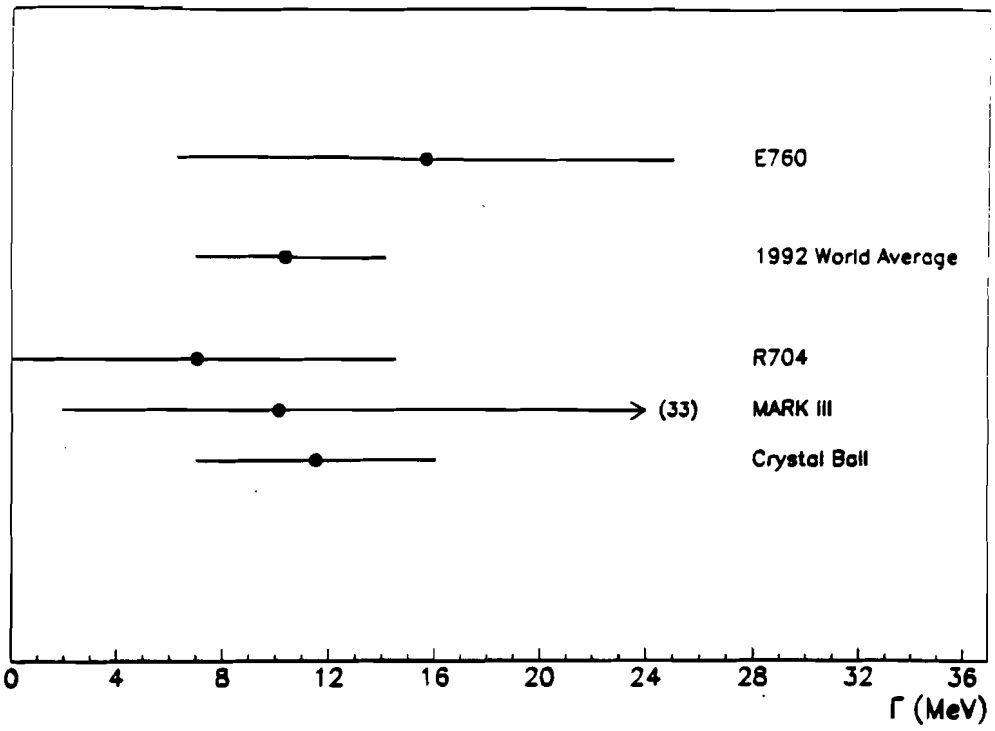

Figure 8.3: Comparison of η_c width with previous measurements

available, all of the theoretical models have used the published values of this splitting to determine the parameters in their potentials and wavefunctions. This measurement of the η_c mass reduces the $J/\psi - \eta_c$ mass splitting which will have the effect of reducing the predicted $\psi' - \eta_c'$ mass splitting. A discussion of these predictions appears below in section 8.2.3.

8.1.2 χ_2 Results

The data used for the χ_2 fit appear in table 8.3. The form of the background used in the χ_2 fit was:

$$\sigma_{bkg} = A\left(\frac{3556.15\ MeV}{E_{CM}}\right)^B \tag{8.16}$$

$\sqrt{s}\ (MeV)$	Events	$\int \mathcal{L}\ (pb^{-1})$	Events/$\int \mathcal{L}\ (pb)$
3522.7-3527.0	204	15.893	12.8
3555.3	7	0.304	23.0
3555.9	55	2.103	26.2
3556.6	2	0.169	11.8
3590.8	9	0.924	9.7
3594.6	5	0.827	6.0
3612.8	5	1.167	4.3
3615.9	13	1.276	10.2
3618.9	7	0.575	12.2
3621.1	16	1.216	13.2
3667.7	2	0.372	5.4
3686.0	14	0.995	14.1

Table 8.3: Final $\gamma\gamma$ candidates for the χ_2 and η_c'

Since the χ_2 mass and total width were independently obtained from analysis of the radiative decay [11], they were fixed[1] at their measured values of $M = 3556.15\ MeV/c^2$ and $\Gamma = 1.98\ MeV$. The fit results are:

$$A = 11.8 \pm 0.7\ pb \tag{8.17}$$

$$B = 7.3 \pm 4.8 \tag{8.18}$$

$$\sigma_m = 14.8 \pm 3.6 \pm 0.5\ pb \tag{8.19}$$

with $\chi^2 = 35.0/24\ dof$. The $\gamma\gamma$ branching ratio and partial width derived from σ_m appear in section 8.2. The data and fitted curve are shown in figures 8.4 and 8.5.

[1]The mass used in the fit was varied by $\pm 120\ KeV/c^2$ to account for the uncertainty in the beam momentum between the data set in which the mass was determined and the data set used in this analysis. The quoted systematic error in the parameter σ_m reflects this uncertainty.

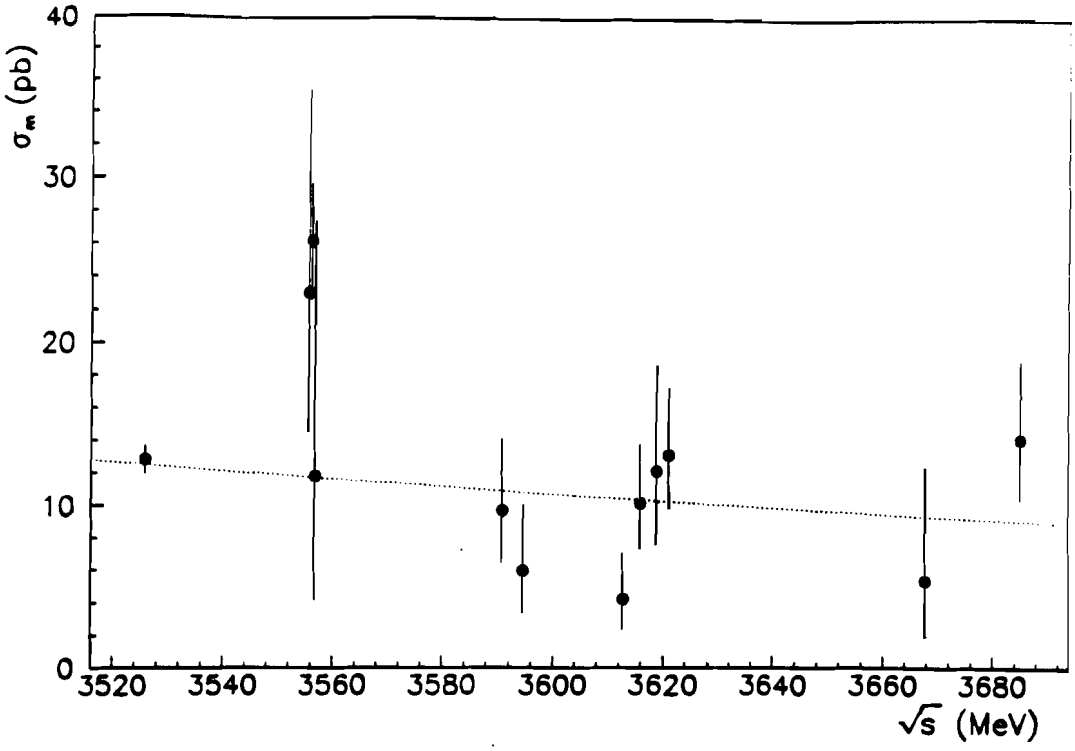

Figure 8.4: Fit to χ_2 data

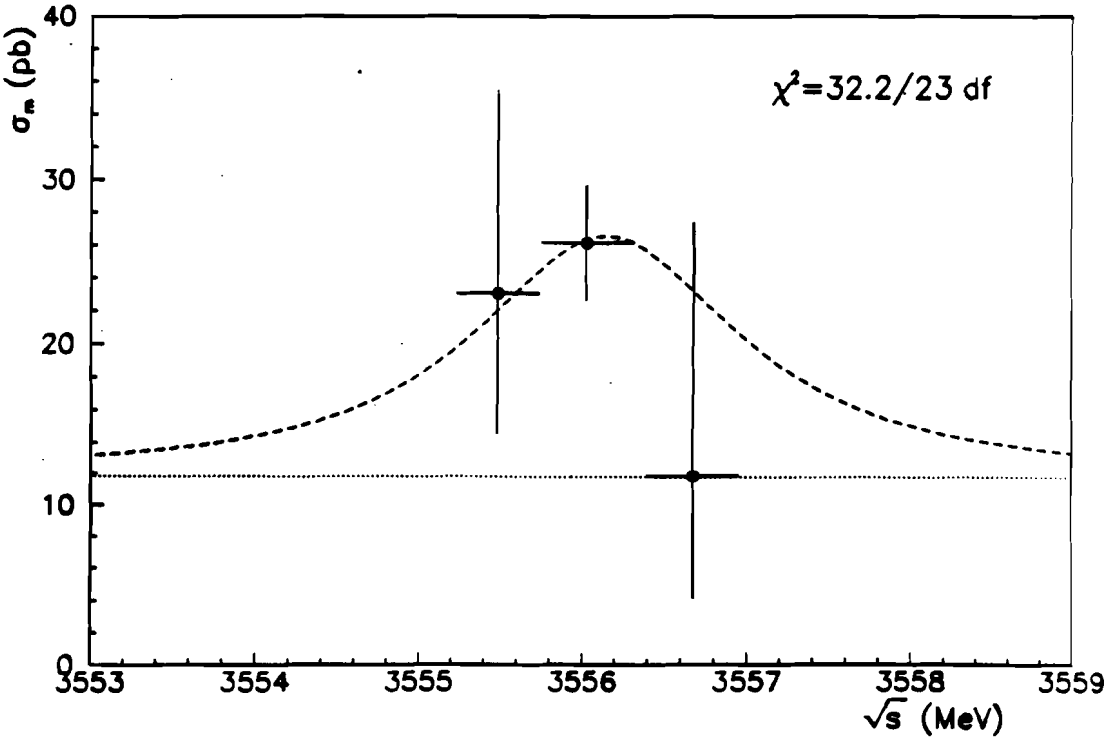

Figure 8.5: Blowup of χ_2 region

8.1.3 η_c' Results

The data from the η_c' search is included as background in the χ_2 analysis. Six points were taken in the region $\sqrt{s} = 3591 - 3621\ MeV$ with no evidence of a signal. An upper limit on the product of branching ratios as a function of $\sqrt{s}$ is presented in section 8.2.3. A discussion of the predicted mass and branching ratios for the η_c' also appears in section 8.2.3.

8.2 Branching Ratios and Partial Widths to $\gamma\gamma$

The product of branching ratios, $BR(R \to \bar{p}p)BR(R \to \gamma\gamma)$, can be extracted from the fitted parameter σ_m of equation 8.1. The trigger and analysis efficiencies were discussed in chapters 3 and 6. Their values are $91 \pm 3 \pm 3\%$ and $79 \pm 2 \pm 4\%$. respectively. The acceptance for each resonance, subject to the $|cos\theta^*|$ cuts used in the analyses, were also covered in chapter 6 and are summarized in table 8.4.

Resonance	$\lvert cos\theta^* \rvert$ cut	Acceptance
η_c	0.20	0.20
χ_2	0.40	0.50 ± 0.02
η_c'	0.40	0.40

Table 8.4: Resonance acceptances

8.2.1 The η_c

Correcting the fitted value of $\sigma_m = 54.6 \pm 14.5 \pm 7.8\ pb$ for efficiency and acceptance, the product of branching ratios is:

$$BR(\eta_c \to \bar{p}p)BR(\eta_c \to \gamma\gamma) = (33.3 \pm 8.9 \pm 5.2) \times 10^{-8}. \tag{8.20}$$

Using the particle data group values $BR(\eta_c \to \bar{p}p) = (12 \pm 4) \times 10^{-4}$ and $\Gamma_{\eta_c} = 10.3^{+3.8}_{-3.4}\ MeV$ [33], the $\gamma\gamma$ branching ratio and partial width are found to be:

$$BR(\eta_c \to \gamma\gamma) = (3.47 \pm 1.48 \pm 0.57) \times 10^{-4} \tag{8.21}$$

$$\Gamma(\eta_c \to \gamma\gamma) = (3.6 \pm 2.0 \pm 0.6)\ KeV. \tag{8.22}$$

Alternatively, using this experiment's measurement of the total width, $\Gamma = 15.6 \pm 6.9 \pm 6.4\ MeV$, the partial width is:

$$\Gamma(\eta_c \to \gamma\gamma) = (5.4 \pm 3.3 \pm 0.9)\ KeV. \tag{8.23}$$

This result is compared to previous measurements and to theoretical predictions in table 8.5. This result is consistent with both the PQCD prediction and that of Barnes and Ackleh. An improved measurement and a realistic estimate of the theoretical uncertainties in the predictions are needed to differentiate between the PQCD result and that of Barnes and Ackleh.

	$\Gamma(\eta_c \to \gamma\gamma)$ (keV)	$BR(\eta_c \to \gamma\gamma)$ (10^{-4})
Experiment		
E760	$5.4 \pm 3.3 \pm 0.9$	$3.5 \pm 1.5 \pm 0.6$
R704 [2]		$6^{+4}_{-3} \pm 4$
CLEO [3]	$5.9^{+2.1}_{-1.8} \pm 1.9$	
TPC [34]	$6.4^{+5.0}_{-3.4}$	
PLUTO [35]	28 ± 15	
Theory		
PQCD [7]	3.7 ± 1.4	
B.A. [14]	4.8	

Table 8.5: Comparison of η_c results with other measurements and theory.

8.2.2 The χ_2

Correcting the fitted value of $\sigma_m = 14.8 \pm 3.6 \pm 0.5\ pb$ for efficiency and acceptance, the product of branching ratios is:

$$BR(\chi_2 \to \bar{p}p)BR(\chi_2 \to \gamma\gamma) = (1.54 \pm 0.38 \pm 0.16) \times 10^{-8}. \tag{8.24}$$

Using the E760 measurements $BR(\chi_2 \to \bar{p}p) = (1.00 \pm 0.09 \pm 0.13) \times 10^{-4}$ and $\Gamma_{\chi_2} = 1.98 \pm 0.17 \pm 0.07\ MeV$ [11,33], the $\gamma\gamma$ branching ratio and partial width are found to be:

$$BR(\chi_2 \to \gamma\gamma) = (1.54 \pm 0.40 \pm 0.26) \times 10^{-4} \tag{8.25}$$

$$\Gamma(\chi_2 \to \gamma\gamma) = 304 \pm 84 \pm 51\ eV. \tag{8.26}$$

A comparison of this result with previous measurements and with theoretical estimates appears in table 8.6. This result is lower than theoretical expectations, with the prediction of Barnes and Ackleh being in best agreement. All of the predictions are sensitive to the value of the strong coupling constant $\alpha_s(m_c)$ and to the mass of

	$\Gamma(\chi_2 \to \gamma\gamma)$ (KeV)	$BR(\chi_2 \to \gamma\gamma)$ (10^{-4})
Experiment		
E760	$0.30 \pm 0.08 \pm 0.05$	$1.5 \pm 0.4 \pm 0.2$
R-704 [2]	$2.9^{+1.3}_{-1.0} \pm 1.7$ [2]	$11^{+5}_{-4} \pm 4$ [2]
CLEO [3]	< 1.0 (95% CL)	
TPC [34]	< 4.2 (95% CL)	
DASP [33]	< 1.6 (90% CL)	
Theory		
PQCD [36]	0.70 ± 0.13 [3]	
B.A. [14]	0.56	
B.B.L. [15]		4.1 ± 1.1 ($\pm$36%)

Table 8.6: Comparison of χ_2 results with other measurements and theory.

[2] This result uses an isotropic angular distribution and $\Gamma(\chi_2) = 2.6^{+1.4}_{-1.0}\ MeV$.
[3] Using $\Gamma(\chi_2 \to gg) = 1.71 \pm 0.21\ MeV$.

the charm quark m_c. For example, using a charm quark mass of $m_c = 1.7\ GeV/c^2$ rather than the typical value of 1.5 GeV/c^2, Barnes and Ackleh predict a rate as low as that observed. The PQCD prediction can also be made to agree with the experimental result using $\alpha_s(m_c) = 0.37$, a value somewhat larger than that obtained from global fits to the charmonium and bottomonium spectra and leptonic widths, $\alpha_s(m_c) = 0.276$ [7], or that obtained by running the value obtained at the mass of the Z^0 down to the mass of the charm quark, $\alpha_s(m_c) = 0.30$ [33]. This result is inconsistent with the prediction of Bodwin, Braaten, and Lepage, but they have not included the substantial leading order QCD correction to this rate. In their formalism the correction for the color octet term is needed, which has not been calculated. Assuming that the leading order correction to the color octet term is comparable to that for the color singlet term, with $\alpha_s(m_c) = 0.3$ their results are in good agreement with the experimental result after corrections.

8.2.3 The η_c'

The only previous measurement of the η_c' resonance comes from the Crystal Ball collaboration [4] which observed an excess of events in the inclusive photon spectrum from ψ' decays at an energy of $91 \pm 5\ MeV$, corresponding to an η_c' mass of $3594.0 \pm 5.0\ MeV$. The Crystal Ball collaboration also placed an upper limit of $8\ MeV$ (95%) on the η_c' width.

The theoretical expectations for the $\psi' - \eta_c'$ mass splitting generally predict a larger η_c' mass than that observed by the Crystal Ball. Since the measured $J/\psi - \eta_c$ mass splitting is used in global fits to the spectrum in order to determine free parameters in the potential and the wavefunctions, the theoretical predictions for the $\psi' - \eta_c'$ depend on the value of the $J/\psi - \eta_c$ splitting available at the time of the calculations. Since the η_c was originally reported to have a mass considerably lower than its present value, early calculations are not reliable. Predictions of the hyperfine splittings are also dependent on the form of the potential, in particular whether the confinement term is taken to be a purely scalar term, or if it is given both scalar and vector contributions. For instance, Gupta, Repko, and Suchyta [13] have calculated the hyperfine splittings using both a purely scalar confinement term and a confinement term with both scalar and vector terms. They find that the data are best fit using both scalar and vector terms in the confinement potential, with the vector term reducing the S-wave hyperfine splittings by about $4\ MeV$. They predict an η_c' mass of $3615\ MeV/c^2$. Note that their parameterization of the potential uses an η_c mass of $2981\ MeV/c^2$ as input. Using the η_c mass

obtained by this experiment will raise their predicted η_c' mass[2]by $\approx 6\ MeV/c^2$. Leading order radiative corrections to the hyperfine splittings have been calculated by Barbieri, Gatto, and Remiddi [37]. They find that these corrections increase the $J/\psi - \eta_c$ hyperfine splitting by 45% from that expected in lowest order. They have not performed these calculations for the $\psi' - \eta_c'$ splitting, but it is likely that these corrections will be comparable to those for the $J/\psi - \eta_c$ splitting. A systematic study, including leading order QCD radiative corrections and coupled-channel effects would greatly improve the theoretical understanding of the hyperfine splittings. In addition, since the leading order corrections are quite large, calculation of the next-to-leading order corrections should also be considered.

An estimate of the expected branching ratios can be made as follows. The decays of the η_c and η_c' into two photons and two gluons (the dominant process for hadronic decays) are identical in form. Each decay mode depends on the value of $|\Psi(0)|^2$, the square of the wave function at the origin. By taking the ratio of the rates, equivalent to the branching ratio to two photons, the wave functions drop out,

$$BR(n^1S_0 \to \gamma\gamma) \approx \left[\frac{\Gamma(n^1S_0 \to \gamma\gamma)}{\Gamma(n^1S_0 \to gg)}\right] = \frac{8}{9}\left(\frac{\alpha}{\alpha_s}\right)^2 [1 + f(\alpha_s)]\,. \qquad (8.27)$$

The first order correction, $f(\alpha_s)$, is independent of the radial quantum number [7], so the $\gamma\gamma$ branching ratio of the η_c' should be equal to that of the η_c, $BR(\eta_c \to$

[2]The $\psi' - \eta_c'$ and $J/\psi - \eta_c$ splittings are expected to scale as $\frac{|\Psi_{\eta_c'}(0)|^2}{|\Psi_{\eta_c}(0)|^2}\,\frac{1-(3\alpha_s/4\pi)\ln\left(R_{\eta_c'}\,m_c\right)}{1-(3\alpha_s/4\pi)\ln\left(R_{\eta_c}\,m_c\right)}$ [37]. The ratio of the wavefunctions (≈ 0.6) at the origin can be estimated from the leptonic widths of the ψ' and J/ψ [7]. The ratio of the logarithmic corrections, ≈ 0.95, is only a minor modification to the leading behaviour.

$\gamma\gamma) = (3.5 \pm 1.6) \times 10^{-4}$. The $\bar{p}p$ coupling is more difficult to estimate. A rough estimate can be made based on the gluonic widths of the J/ψ, ψ', and η_c and the relative probabilities of hadronization to $\bar{p}p$ at the J/ψ and ψ'. Assuming that

$$\frac{\Gamma(\eta_c' \to \bar{p}p)/\Gamma(\eta_c' \to \text{glue})}{\Gamma(\eta_c \to \bar{p}p)/\Gamma(\eta_c \to \text{glue})} \approx \frac{\Gamma(\psi' \to \bar{p}p)/\Gamma(\psi' \to \text{glue})}{\Gamma(J/\psi \to \bar{p}p)/\Gamma(J/\psi \to \text{glue})} \tag{8.28}$$

the result is $BR(\eta_c' \to \bar{p}p) \approx (6 \pm 3) \times 10^{-4}$. Note that the total widths of the η_c and η_c' are dominated by their gluonic widths while the total widths of the J/ψ and ψ' have large contributions from radiative decays, decays to virtual photons (which have small probabilities for hadronization to $\bar{p}p$ [38]), and for the ψ' a large width for hadronic decays to the J/ψ. This results in a crude estimate of $BR(\eta_c' \to \bar{p}p)BR(\eta_c' \to \gamma\gamma) \approx (2.1 \pm 1.4) \times 10^{-7}$.

There is no indication of a signal in the data taken during the E760 search for the η_c' resonance in the region $\sqrt{s} = 3591 - 3621\ MeV$. Upper limits on the product of branching ratios $BR(\eta_c' \to \bar{p}p)BR(\eta_c' \to \gamma\gamma)$ can be placed as a function of $\sqrt{s}$, or equivalently as a function of the η_c' mass, and as a function of the total width of the η_c'. The analysis of the 95% upper limits on the product of branching ratios utilized the same likelihood analysis that was performed on the χ_2 data. The background level was fixed (see equations 8.16-8.19), as were the mass and width of the resonance. The only free parameter in the fit was σ_m, defined in equation 8.1. The 95% upper limit was defined by the value of σ_m for which the log of the likelihood function was 2 units less than the maximum value. The product of branching ratios is obtained using equation 8.1. The efficiency is $72 \pm 4 \pm 6\%$ (trigger and analysis) and the acceptance is 0.40 (assuming an isotropic

decay). The 95% upper limits as a function of the η_c' mass, for widths of 5 MeV and 10 MeV, are shown in figure 8.6. Based on the estimate for the product of

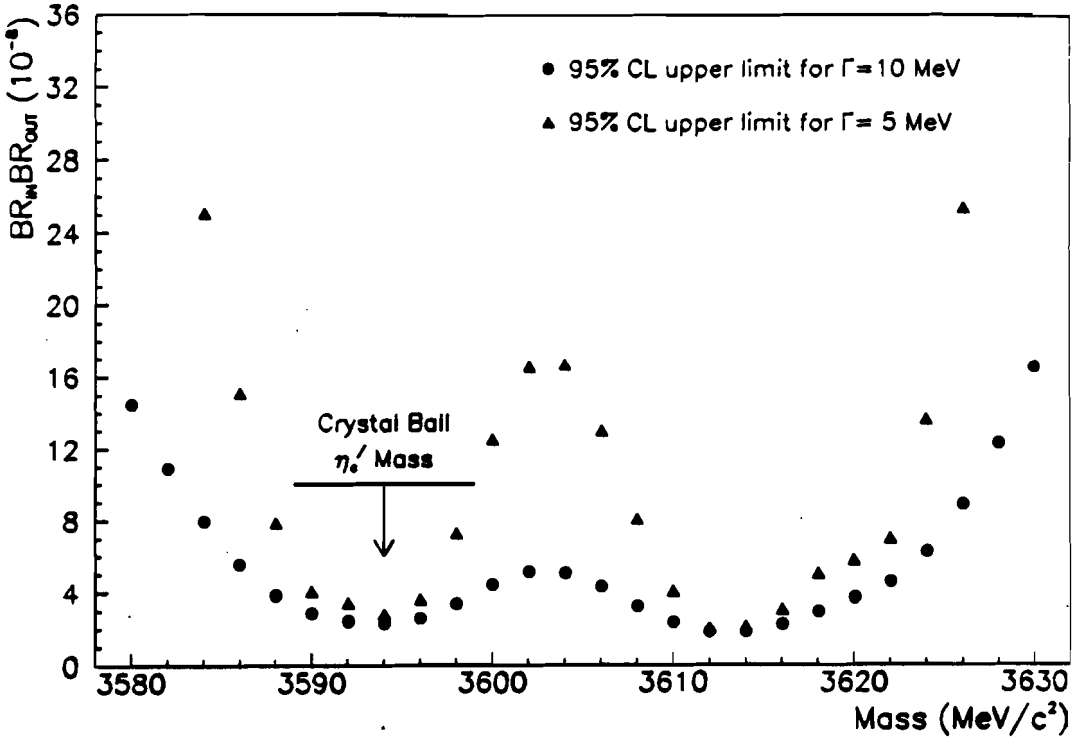

Figure 8.6: 95% upper limit for $BR(\eta_c' \to \bar{p}p)BR(\eta_c' \to \gamma\gamma)$

branching ratios presented above, the η_c' can be excluded in the mass region of the Crystal Ball measurement at better than 95% confidence.

8.2.4 Derivation of $\alpha_s(m_c)$ From The $\gamma\gamma$ Branching Ratios

An interesting result from these measurements is to derive the value of $\alpha_s(m_c)$ and compare it with the value obtained from deep inelastic scattering and LEP results [33]. From the ratio of equations 1.7 and 1.6, the measured branching ratio

$BR(\eta_c \rightarrow \gamma\gamma) = (3.47 \pm 1.58) \times 10^{-4}$ can be used to obtain a value of

$$\alpha_s(m_c) = 0.26^{+0.06}_{-0.04}. \tag{8.29}$$

The ratio of equations 1.9 and 1.8 for the χ_2 decays can be used to obtain an independent determination of $\alpha_s(m_c)$. In this case the gluonic width cannot be approximated by the total width because of the large radiative decay branching ratio, $13.5 \pm 1.1\%$. This gives a gluonic width of $1.71 \pm 0.21\ MeV$ [11]. From this measurement of $BR(\chi_2 \rightarrow \gamma\gamma) = (1.54 \pm 0.48) \times 10^{-4}$, the coupling constant is found to be

$$\alpha_s(m_c) = 0.37^{+0.04}_{-0.03}. \tag{8.30}$$

These values can be compared with the world average, $\alpha_s(m_Z) = 0.1134 \pm 0.0035$, by "running" this value down to the charm quark mass, m_c[3]. The value is

$$\alpha_s(m_c) = 0.32^{+0.01}_{-0.03} \tag{8.31}$$

which is in good agreement with the values obtained from these measurements of the two photon branching ratios.

8.3 Conclusion

Fermilab experiment E760 has measured the mass and width of the η_c resonance. The mass obtained from this analysis is consistent with, but somewhat higher than previous measurements. The width obtained is consistent with pre-

[3]The procedure for doing this, including higher order corrections, appears in [33].

vious values. Branching ratios and partial widths to two photons have been measured for the η_c and χ_2 resonances. The η_c results are consistent with previous measurements, while the χ_2 values constitute the first significant measurements of nonzero values. The null results of the η_c' search constitute reasonably stringent upper limits on the product of branching ratios $BR(\eta_c' \to \bar{p}p)BR(\eta_c' \to \gamma\gamma)$ in the mass region scanned.

Bibliography

[1] The Particle Data Group. *Phys. Lett. B*, 239:VII.140–VII.156, 1990.

[2] C. Baglin et al. *Phys. Lett.*, B187:191–197, 1987.

[3] W.-Y. Chen et al. *Phys. Lett.*, B243:169–174, 1990.

[4] C. Edwards et al. *Phys. Rev. Lett.*, 48:70–73, 1982.

[5] T. Appelquist et al. *Ann. Rev. Nucl. Part. Sci.*, 28:387–499, 1978.

[6] W. Kwong et al. *Ann Rev. Nucl. Part. Sci.*, 37:325–382, 1987.

[7] W. Kwong et al. *Phys. Rev. D*, 37:3210–3215, 1988.

[8] A. Martin and J. M. Richard. *Phys. Lett.*, B115:323–328, 1982.

[9] The Particle Data Group. *Phys. Rev. D*, 48:III.54–58, 1992.

[10] T.A. Armstrong et al. *Phys. Rev. Lett.*, 69:2337, 1992.

[11] T.A. Armstrong et al. *Nucl. Phys. B*, 373:35, 1992.

[12] V. Gupta et al. *Phys. Rev. D*, 37:740, 1988.

[13] S. Gupta et al. *Phys. Rev. D*, 39:974, 1989.

[14] T. Barnes and E. Ackleh. ORNL-CCIP-92-05, UTK-92-3.

[15] G. Bodwin et al. *Phys. Rev. D*, 46:1914, 1992.

[16] P. Bryant and S. Newman. *CERN Accelerator School 1983*, CERN 84-15, 1984.

[17] M. Macri. *CERN Accelerator School 1983*, CERN 84-15, 1984.

[18] A.C. Melissinos and S.L. Olsen. *Phys. Rep.*, 3:77, 1975.

[19] C. Biino et al. *Nucl. Inst. and Meth.*, A271:417, 1988.

[20] R. Calabrese et al. *IEEE Trans. Nucl. Sci.*, 36:54, 1989.

[21] R. Calabrese et al. *IEEE Trans. Nucl. Sci.*, 36:54, 1989.

[22] C. Biino et al. *Nucl. Inst. and Meth.*, A317, 1992. to be published.

[23] G. Barisone et al. Report A.E./89-6, I.N.F.N., 1989.

[24] L. Bartoszek et al. *Nucl. Instr. and Meth.*, A301:47, 1991.

[25] M.A. Hasan et al. *Nucl. Instr. and Meth.*, A295:73, 1990.

[26] R. Ray et al. *Nucl. Instr. and Meth.*, A307:254, 1991.

[27] I. Gaines et al. *Computer Physics Communications*, 45:323, 1987.

[28] C. Gay et al. *IEEE Trans. on Nucl. Sci.*, 34:870, 1987.

[29] M.G. Olsson et al. *Phys. Rev. D*, 34:2043–2046, 1986.

[30] E-760 collaboration. Measurement of the angular distributions from the radiative decays of the χ_1 and χ_2 states of charmonium formed in $\overline{p}p$ annihilations. To be published.

[31] H. Aihara et al. *Phys. Rev. Lett.*, 57:404–407, 1986.

[32] E-760 collaboration. Measurement of the differential cross sections for $\bar{p}p \rightarrow \pi^0\pi^0$ and $\bar{p}p \rightarrow \pi^0\gamma$ at $\sqrt{s} = 2.9$ to 3.7 gev. To be published.

[33] The Particle Data Group. *Phys. Rev. D*, 48:VII.166–182, 1992.

[34] H. Aihara et al. *Phys. Rev. Lett.*, 60:2355–2358, 1988.

[35] C. Berger et al. *Phys. Lett.*, 167B:120–126, 1986.

[36] W. Kwong et al. *Phys. Rev. D*, 37:3210, 1988. And references therein.

[37] R. Barbieri et al. *Phys. Lett.*, B106:497–500, 1981.

[38] E-760 collaboration. Measurement of the proton electromagnetic form factors in the time-like region at 8.9 and 13.0 gev^2. to be published.

[39] B. Rossi. ***High-Energy Particles.*** Prentice-Hall, Inc., 1952.

[40] J. Richman. ***DOE Research and Development Reort***, CALT-68-1148, 1984.

Appendix A

Estimate of δ−ray Production from Beam-Target Interactions

Production of δ−rays from interactions of the circulating antiprotons with electrons in the molecular hydrogen target play a major role in the inefficiency of the neutral trigger. The $H1$ OR rate, about 3 MHz at peak luminosity, consists of the $\bar{p}p$ interaction rate, about 1 MHz, plus the δ−ray rate. The distribution of δ−rays is given by [33]

$$\frac{d^2N}{dTdx} = \frac{1}{2}\left[4\pi N_A r_e^2 m_e c^2\right] z^2 \frac{Z}{A}\,\frac{1}{\beta^2}\,\frac{F(T)}{T^2} \qquad \text{(A.1)}$$

where T is the kinetic energy of the knock-on electron, β is the antiproton velocity, and $F(T)$ is a spin dependent factor dependent on the particles involved. The numerical value for the constants in the square brackets[1] is 0.307 $MeVcm^2g^{-}1$. The atomic number z for the incident particle, and the atomic number Z and atomic mass A of the target particle are all 1. For antiproton-hydrogen collisions,

[1] N_A is Avagadro's number, r_e is the classical radius of the electron, m_e is the mass of the electron, and c is the speed of light.

the spin dependent factor is given by [39]

$$F(T) = 1 - \beta^2 \left(\frac{T}{T_{max}}\right) + \frac{1}{2}\left(\frac{T}{E_{\overline{p}}}\right)^2 \tag{A.2}$$

where the maximum kinetic energy that can be imparted to the electron is $T_{max} \approx 2m_e c^2 \beta^2 \gamma^2$.

The angular coverage of the $H1$ counters is $15°-60°$. The FCV array covers the region $5° - 15°$. The momentum of a knock-on electron is related to its scattering angle through the relation

$$P \approx \frac{2m_e \beta cos\theta}{1 - \beta^2 cos^2\theta} \tag{A.3}$$

where it is assumed that the initial and final antiproton energies are equal. Table A.1 contains, for several beam momenta, the values for the electron kinetic energy at the edges of the counters. Table A.2 contains the integral of equation A.1 over each of the counters, using equation A.2 for $F(T)$.

$P_{\overline{p}}\ (GeV/c)$	$T_{max}\ (MeV)$	$T_{5°}\ (MeV)$	$T_{15°}\ (MeV)$	$T_{60°}\ (MeV)$
3.5	14.2	12.8	6.86	0.311
4.5	23.5	19.9	8.63	0.322
5.5	35.1	27.7	9.91	0.328
6.5	49.1	35.7	10.85	0.332

Table A.1: Kinetic energies of δ-rays incident on $H1$ and FCV

The rates in the counters are obtained by integration with respect to x over the target thickness and multiplication by the flux of antiprotons. For a luminosity of $3.5 \times 10^{30} cm^{-2} s^{-1}$, the values for dN/dx which appear in table A.2 can be multiplied by 5.83 $MHz cm^{-2} g$ to get the rates in the counters. The result is that

$P_{\bar{p}}$ (GeV/c)	$\frac{dN}{dx}$ for $H1$ (cm^2g^{-1})	$\frac{dN}{dx}$ for FCV (cm^2g^{-1})
3.5	0.472	0.004
4.5	0.457	0.005
5.5	0.451	0.006
6.5	0.447	0.006

Table A.2: $\frac{dN}{dx}$ of δ-rays incident on $H1$ and FCV

the rate in $H1$ is about 2.6 MHz and the rate in the FCV array is about 30 KHz at this luminosity. In the trigger, the gate length for the scintillator counters is 30 $nsec$. Thus the expected inefficiency due to $\delta-$rays in $H1$ or the FCV array is 7.8%, to be compared with the measured value of 6.5% (see section 6.5).

Appendix B

Derivation of the Angular Distribution for $\bar{p}p \rightarrow \chi_2 \rightarrow \gamma\gamma$

This derivation is based on, and uses the notation of, reference [40]. Figure B.1 is a schematic of the process. The particle helicities are indicated by the Greek symbols.

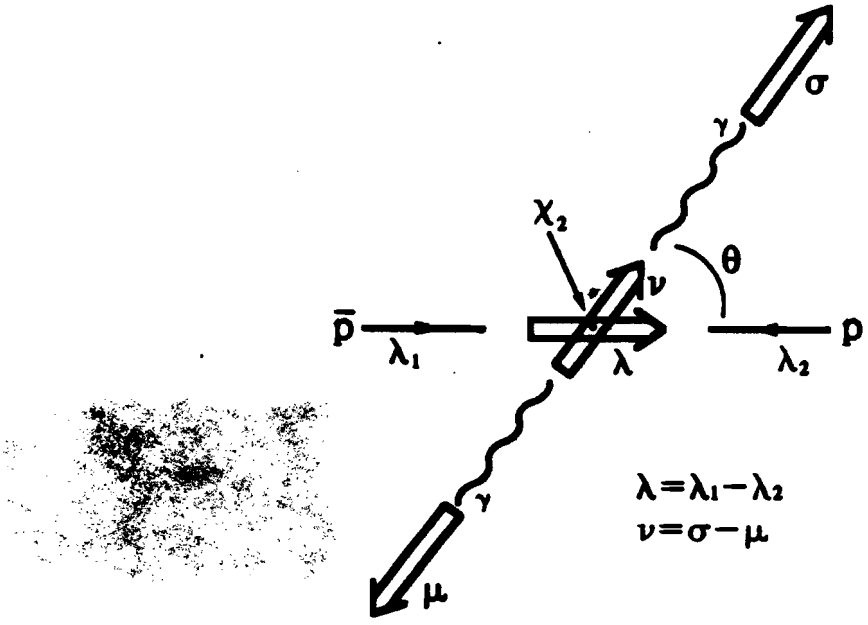

Figure B.1: Diagram of the process $\bar{p}p \rightarrow \chi_2 \rightarrow \gamma\gamma$ in the helicity formalism

B.1 Production Amplitude

The amplitude for production of a χ_2 ($J = 2$) from the annihilation of an antiproton of helicity λ_1 and a proton with helicity λ_2 is

$$A(\bar{p}p \to \chi_2) = \langle J, m_j | U | \theta, \phi, \lambda_1, \lambda_2 \rangle. \tag{B.1}$$

The angles θ and ϕ define the direction of the χ_2 quantization axis relative to the quantization axis along which the incident particle (proton and antiproton) helicities are defined. Insertion of a complete set of states gives

$$A(\bar{p}p \to \chi_2) = \sum_{J'} \sum_{m_j'} \sum_{\lambda_1'} \sum_{\lambda_2'} \langle J, m_j | U | J', m_j', \lambda_1', \lambda_2' \rangle \langle J', m_j', \lambda_1', \lambda_2' | \theta, \phi, \lambda_1, \lambda_2 \rangle. \tag{B.2}$$

Since the strong interaction conserves angular momentum

$$\langle J, m_j | U | J', m_j', \lambda_1', \lambda_2' \rangle = \delta_{JJ'} \delta_{m_j m_j'} \langle J, m_j | U | J', m_j', \lambda_1', \lambda_2' \rangle. \tag{B.3}$$

Inserting equation B.3 into equation B.2 and summing over J' and m_j',

$$A(\bar{p}p \to \chi_2) = \sum_{\lambda_1'} \sum_{\lambda_2'} \langle J, m_j | U | J, m_j, \lambda_1', \lambda_2' \rangle \langle J, m_j, \lambda_1', \lambda_2' | \theta, \phi, \lambda_1, \lambda_2 \rangle. \tag{B.4}$$

The first matrix element in equation B.4 is independent of m_j and is defined to be

$$B_{\lambda_1', \lambda_2'} \equiv \langle J, m_j | U | J, m_j, \lambda_1', \lambda_2' \rangle. \tag{B.5}$$

The second is given by

$$\langle J, m_j, \lambda_1', \lambda_2' | \theta, \phi, \lambda_1, \lambda_2 \rangle = \delta_{\lambda_1 \lambda_1'} \delta_{\lambda_2 \lambda_2'} \sqrt{\frac{2J+1}{4\pi}} D^J_{m_j, \lambda}(\phi, \theta, -\phi) \tag{B.6}$$

where $\lambda = \lambda_1 - \lambda_2$. The production amplitude is symmetric in ϕ, so the coordinate systems may be chosen such that $\phi = 0$. With this choice, the production

amplitude may be written as

$$A(\bar{p}p \to \chi_2) = \sqrt{\frac{5}{4\pi}} B_{\lambda_1,\lambda_2} d^2_{m_j,\lambda}(\theta) \tag{B.7}$$

where the functions $d^2_{m_j,\lambda}(\theta)$ can be found in [33].

B.2 Decay Amplitude

The amplitude for the decay of a χ_2 ($J = 2$) into two photons can be written in a similar manner as the production amplitude discussed above. For photons of helicities σ and μ

$$A(\chi_2 \to \gamma\gamma) = \langle \theta, \phi, \sigma, \mu | V | J, m_j \rangle. \tag{B.8}$$

Insertion of a complete set of states and summation over the dummy variables, again utilizing the fact that the interaction conserves angular momentum, gives

$$A(\chi_2 \to \gamma\gamma) = \sqrt{\frac{5}{4\pi}} A^*_{\sigma,\mu} D^{2\,*}_{m_j,m_j}(\phi, \theta, -\phi) \tag{B.9}$$

where

$$A^*_{\sigma,\mu} \equiv \langle J, m_j, \sigma, \mu | V | J, m_j \rangle. \tag{B.10}$$

Since the χ_2 quantization axis has been chosen to coincide with the photon axis, $\theta = 0$. Using the relation $D^J_{m_j,\mu}(\phi, 0, -\phi) = \delta_{m_j\mu}$, the decay amplitude is

$$A(\chi_2 \to \gamma\gamma) = \sqrt{\frac{5}{4\pi}} A^*_{\sigma,\mu}. \tag{B.11}$$

B.3 Differential Cross Section for $\bar{p}p \rightarrow \chi_2 \rightarrow \gamma\gamma$

The differential cross section for $\bar{p}p \rightarrow \chi_2 \rightarrow \gamma\gamma$ is given by

$$\frac{d\sigma}{d\Omega} \propto \frac{1}{4} \sum_{\sigma,\mu} \sum_{\lambda_1,\lambda_2} |A(\bar{p}p \rightarrow \chi_2 \rightarrow \gamma\gamma)|^2 \tag{B.12}$$

where the initial states have been averaged over and the final states summed over. Inserting equations B.7 and B.11,

$$\frac{d\sigma}{d\Omega} \propto \frac{1}{4} \left(\frac{5}{4\pi}\right)^2 \sum_{\sigma,\mu} \sum_{\lambda_1,\lambda_2} |A^*_{\sigma,\mu}|^2 |B_{\lambda_1,\lambda_2}|^2 |d^2_{m_j,\lambda}|^2 \tag{B.13}$$

B.3.1 Relations Between Amplitudes

From time reversal symmetry and the Hermiticity of the electromagnetic decay amplitude, the $A_{\sigma,\mu}$ are real. Due to parity conservation in both the strong interaction and the electromagnetic interaction, the amplitudes satisfy $A_{\sigma,\mu} = A_{-\sigma,-\mu}$ and $B_{\lambda_1,\lambda_2} = B_{-\lambda_1,-\lambda_2}$.

Due to these symmetries, the amplitudes can be characterized by the total helicity of the initial or final state. In the following definitions the subscripts in the expressions on the left side of the equations refer to the total helicity of the initial or final state.

$$\frac{1}{2}B_0^2 \equiv |B_{1/2,1/2}|^2 = |B_{-1/2,-1/2}|^2 \tag{B.14}$$

$$B_1^2 \equiv |B_{1/2,-1/2}|^2 = |B_{-1/2,1/2}|^2 \tag{B.15}$$

$$R \equiv \frac{2B_1^2}{B_0^2 + 2B_1^2} \tag{B.16}$$

$$\frac{1}{2}A_0^2 \equiv |A_{1,1}|^2 = |A_{-1,-1}|^2 \tag{B.17}$$

$$\frac{1}{2}A_2^2 \equiv |A_{1,-1}|^2 = |A_{-1,1}|^2 \tag{B.18}$$

The normalizations are $B_0^2 + 2B_1^2 = 1$ and $A_0^2 + A_2^2 = 1$.

B.4 The Angular Distribution

The angular distribution for the process $\bar{p}p \to \chi_2 \to \gamma\gamma$ is obtained by explicitly calculating the sums in equation B.13 subject to the conditions outlined in the section B.3.1. The result is:

$$\begin{aligned}\frac{d\sigma}{d\Omega} \propto\ & B_0^2\left[A_0^2\left(d^2_{0,0}(\theta)\right)^2 + A_2^2\left(d^2_{2,0}(\theta)\right)^2\right] \\ & +2B_1^2\left[A_0^2\left(d^2_{1,0}(\theta)\right)^2 + A_2^2\left\{\frac{1}{2}\left(d^2_{2,1}(\theta)\right)^2 + \frac{1}{2}\left(d^2_{2,-1}(\theta)\right)^2\right\}\right].\end{aligned} \tag{B.19}$$

Inserting the explicit forms for the d-functions from [33], and extracting only the angular dependence,

$$W(cos\theta) = \frac{5}{8}\left[k_1 + k_2 cos^2\theta + k_3 cos^4\theta\right] \tag{B.20}$$

where the constants k_1, k_2, and k_3 are

$$k_1 = [2A_2^2]R + [2A_0^2 + 3A_2^2](1 - R) \tag{B.21}$$

$$k_2 = [12A_0^2]R + [-12A_0^2 - 6A_2^2](1 - R) \tag{B.22}$$

$$k_3 = [-12A_0^2 - 2A_2^2]R + [18A_0^2 + 3A_2^2](1 - R) \tag{B.23}$$

with the normalization being

$$\int_0^1 W(cos\theta)d(cos\theta) = 1. \tag{B.24}$$